# HIGH INDEX GLASS THIN FILM PROCESSING FOR PHOTONICS AND PHOTOVOLTAIC (PV) APPLICATIONS

by

Okechukwu Anthony Ogbuu

A dissertation submitted to the Faculty of the University of Delaware in partial fulfillment of the requirements for the degree of Doctor of Philosophy in Materials Science and Engineering

Spring, 2016

**HIGH INDEX GLASS THIN FILM PROCESSING FOR**

**PHOTONICS AND PHOTOVOLTAIC (PV) APPLICATIONS**

by

Okechukwu Anthony Ogbuu

Approved: _____
Darrin Pochan, Ph.D.
Chair of the Department of Materials Science and Engineering

Approved: _____
Babatunde Ogunnaike, Ph.D.
Dean of the College of Engineering

Approved: _____
Ann L. Ardis, Ph.D.
Senior Vice Provost for Graduate and Professional Education

I certify that I have read this dissertation and that in my opinion it meets the academic and professional standard required by the University as a dissertation for the degree of Doctor of Philosophy.

Signed: _____

Juejun Hu, Ph.D.
Professor in charge of dissertation

I certify that I have read this dissertation and that in my opinion it meets the academic and professional standard required by the University as a dissertation for the degree of Doctor of Philosophy.

Signed: _____

Robert Birkmire, Ph.D.
Member of dissertation committee

I certify that I have read this dissertation and that in my opinion it meets the academic and professional standard required by the University as a dissertation for the degree of Doctor of Philosophy.

Signed: _____

Robert Opila, Ph.D.
Member of dissertation committee

I certify that I have read this dissertation and that in my opinion it meets the academic and professional standard required by the University as a dissertation for the degree of Doctor of Philosophy.

Signed: _____

Kathleen Richardson, Ph.D.
Member of dissertation committee

## ACKNOWLEDGMENTS

It was truly an interesting journey filled with rich experiences that will guide me through my life. It could not have happened without the positive contributions of several smart and talented people. I am here to appreciate them.

First I want extend my unalloyed appreciation to University of Delaware and more importantly to Departmental of Materials Science and Engineering for offering an opportunity to commence and the necessary support they provided throughout the program. I must say that I am very privileged to interactive and network with the smart and diverse faculty and students in MSEG UD. The Faculty and students contributed in many ways to the completion of my program.

I would like to express my sincere gratitude to my advisor Prof. JJ Hu whose mentorship and encouragement was super instrumental and handy through the difficult moments in the program. His smart ideas provided the required additional problem solving edge to navigate through the challenging problems encountered through this project. Besides, he doubled as a supervisor and a career mentor who creates time out of his very busy schedule to listen and make positive contributions.

I would like to thank my group members; Hongtao Lin, Lan Li, Sarah Geiger, Qingyang Du, June Li and others who contributed immensely to the successful completion of the project through experimental and research discussions. I want to specially thank Hongtao Lin and Lan Li for their insightful research ideas during numerous discussions, June Li for assisting in thermal evaporation of thin films used in this project, Sarah Geiger for the intellectual research and social discussions and

Qinyang Du for all those Massachusetts-Delaware trips. It was and will always be a memorable experience spending the past years with you guys. Hu-group rocks!

This piece will not be complete without the mention people who were great friends and brothers that made graduate school memorable; Mohamed Bah and Ugochukwu Nsofor. Thank you Mohamed for the endless motivations, thought provoking discussions during lunch & coffee breaks and being the best running buddy. He is always there for me both in good and bad days through graduate school. Thank you Ugochukwu, for those valuable advices and wonderful counsels. I trust I will get to hear your good stories of graduate school. I would also use this opportunity to express my immense gratitude to Uchechukwu Obialasor who was the listening ear and good company at the other end of the line through many lonely days of graduate school. I will not forget to mention Dr. Mfon Umoren who, without know it, motivated and supported me in numerous ways and silently pushed me to quickly finish up this thesis. Thanks Mfon for your great support and encouragements. Similar appreciation goes to numerous individuals and groups who helped squeeze out the best in me through graduate school days. In more than a million ways, everyone was amazing!

I want to thank our collaborators (Richardson group at UCF and Birkmire group at IEC) who were provided extreme support to ensure smooth completion of the project. Your reliable support and positive contributions was instrumental to the progress made in this study. I want to thank Prof. Richardson and her group members (Dr. Sylvain Danto, Erick Koontz, Rebecca Whitsitt, Spencer Novak, Jacklyn Novak, Jason Lonergan, Dr. David Musgraves) for providing bulk materials (chalcogenide and tellurites) used for thin film deposition. Her detailed and insightful discussions

provided a strong guide through the project. I am really grateful. Thanks to Prof. Birkmire and his group members (Gowri Sriramagiri, Evan Kimberly, Dr. Kevin Dobson and Hamed Simchi) for providing the solar cells and devices characterization. In addition, I am grateful to IEC staff and students; Peipei Xin, Uwadiae Obahiagbon, James Matitu who assisted in terms of the training and usage of IEC's instruments, including UV-Vis, Raman, ellipsometry, during my Ph.D. program.

I would also want to thank MTL staff members at Massachusetts Institute of Technology; Kurt Broderick and Gary Riggott; for their assistance with instruments in EML.

To all my committee members I say a big thank you for your time and valuable advices. I will ever remain grateful.

Finally I want to express utmost gratitude to my parents and siblings for their support, love and patience through these years. Without your amazing support and care, I would not make it this far. I love you all.

Above all, I say all glory to almighty God for making this journey and dream a reality. **God, you always win**.

## TABLE OF CONTENTS

## LIST OF TABLES

## LIST OF FIGURES

## ABSTRACT

To favorably compete with fossil-fuel technology, the greatest challenge for thin film solar-cells is to improve efficiency and reduce material cost. Thickness scaling to thin film reduces material cost but affects the light absorption in the cells; therefore a concept that traps incident photons and increases its optical path length is needed to boost absorption in thin film solar cells. One approach is the integration of low symmetric gratings (LSG), using high index material, on either the front-side or backside of 30 um thin c-Si cells.

In this study, Multicomponent $TeO_2$–$Bi_2O_3$–ZnO (TBZ) glass thin films were prepared using RF magnetron sputtering under different oxygen flow rates. The influences of oxygen flow rate on the structural and optical properties of the resulting thin films were investigated. The structural origin of the optical property variation was studied using X-ray diffraction, X-ray photoelectron spectroscopy, Raman Spectroscopy, and transmission electron microscopy. The results indicate that TBZ glass thin film is a suitable material for front side LSG material photovoltaic and photonics applications due to their amorphous nature, high refractive index ($n > 2$), broad band optical transparency window, low processing temperature.

We developed a simple maskless method to pattern sputtered tellurite based glass thin films using unconventional agarose hydrogel mediated wet etching. Conventional wet etching process, while claiming low cost and high throughput, suffers from reproducibility and pattern fidelity issues due to the isotropic nature of wet chemical etching when applied to glasses and polymers. This method overcomes

these challenges by using an agarose hydrogel stamp to mediate a conformal etching process. In our maskless method, agarose hydrogel stamps are patterned following a standard soft lithography and replica molding process from micropatterned masters and soaked in a chemical etchant. The micro-scale features on the stamp are subsequently transferred into glass and polymer thin films via conformal wet etching.

High refractive index chalcogenide glass (n = 2.6) thin films with composition $As_{20}Se_{80}$ was selected for backside LSG material due to their attractive properties. We developed an optimized integration protocol for LSG integration and successfully integrated these LSG structures at the back side of both 30 µm c-Si solar cells and standalone 30 µm c-Si wafers. Optical and electrical characterization of LSG on thin c-Si cells shows that LSG structures create higher absorption enhancement and external quantum efficiency at long wavelengths.

# Chapter 1

# INTRODUCTION

## 1.1 Background and Motivation

Photovoltaics (PV); the conversion of sunlight to electricity, is a promising technology that may allow generation of electrical power on a very large scale. Over the past two years, solar cell technology has progressed more rapidly than even the most optimist forecasts [1]. In May 2011 hundreds of thousands of mainly small, private photovoltaic systems combined to supply over 20% of Germany's monthly peak electricity demand as well as 8% of its monthly usage [2]. Presently, most of the solar-cell market is based on crystalline silicon(c-Si) wafers with thickness between 180 -500 um, and the bulk of the price lies on the costs of silicon materials and processing. In order to reposition power generated from photovoltaic technology to effectively compete with fossil-fuel technologies; the cost needs to be reduced by a factor of 2-5. As a result, there is a profound interest in reducing the thickness of bulk Photovoltaic cells to thin film solar cells.

Thin c-Si and thin film polycrystalline solar cells are the primary technologies that are expected to meet the DOE goal of 1$/W photovoltaics. Reducing the c-Si wafer thickness to less than 50 microns or thin films to less than an absorption length significantly reduces material cost, and may result in improvements in efficiency by minimizing bulk recombination and decreasing dark current. For c-Si modules, the cost of the silicon absorber material currently comprises approximately 1/6 of the

system cost which must be drastically reduced by moving to thin wafers, < 50 μm or less, most likely produced by kerfless wafering techniques to eliminate current kerf losses of over 50%. In the case of polycrystalline thin film cells, CdTe technology is the first to demonstrate the "promise of thin film PV", where high throughput processing and large-scale facilities significantly reduce its cost.

Market leader First Solar has a manufacturing capacity of 1.5 GW/year and has achieved the lowest manufacturing cost in the PV industry of $0.75/watt with a module conversion efficiency of 11.7%. $CuInSe_2$ based module manufacturing is following the pathway of CdTe and is expected to meet or exceed the cost achieved by CdTe as large scale manufacturing facilities come on line [3]. A promising approach to further reduce cost is to make the absorber thinner which minimizes material cost and increases manufacturing throughput. This approach appears to be very compatible with $CuInSe_2$ based technologies and less so for CdTe. The fundamental penalty incurred by reducing wafer thickness is poorer optical absorption. This limitation is predominant in all thin-film solar-cell technologies because absorption near their band-gap is small, particularly for indirect band-gap semiconductors (e.g silicon). This limitation can be addressed using an advanced light trapping [1]. Light trapping scheme is a technique that allows solar cells to absorb sunlight using an active material layer designed such that the distance light travels in them is much larger than their thickness. This technique does not only improve the cell efficiency but also enables thickness scaling and cost reduction of solar cells. This technology-transforming attribute forms the core focus of this proposal.

Light trapping in solar cells has been conventionally implemented using geometric structuring [4, 5] random surface/ Transparent Conducting Oxide (**TCO**)

texturing [6, 7] or periodic gratings/photonic crystals (**PhCs**) [8, 9, 10]. Geometric structuring is not applicable for thin film cells whose thickness becomes comparable to wavelength. While very encouraging PV efficiency boost has been demonstrated using the latter two methods, two major challenges present barriers to their practical applications: (1) limited light trapping enhancement; and (2) high fabrication cost and solar cell material degradation. The maximum absorption enhancement factor in a thin film solar cell has been derived by Yablonovitch et al. to be $4n^2$ in the geometric optics regime where n is the refractive index of the cell material [11, 12]. The $4n^2$ Lambertian limit corresponds to 40-60x absorption enhancement for semiconductor solar cells, although in practice the enhancement factor is typically < 10, limited by low diffraction efficiency [13] and parasitic loss mechanisms such as increased surface recombination and surface plasmon absorption[14]. Recently significant efforts have been devoted to closing this large gap between the $4n^2$ limit and practically achieved enhancement, and it has been theoretically shown that enhancement factor close to or even exceeding the Lambertian limit is possible in the wave optics regime [15,16]. Nevertheless, few experimental demonstrations have been made to validate these theoretical predictions, and enhancement close to the Lambertian limit has only been achieved at few selected wave bands [17, 18].

On the fabrication end, light trapping requires high-index, wavelength-scale surface corrugation structures on solar cells which are produced either by conventional lithography and etching, or by cell material deposition on roughened substrates such as textured TCO. In the former approach, the fine-line lithography steps involved for wavelength-scale grating or PhC patterning incurs high cost and defeats the cost reduction purpose of thickness scaling. Variants of the approach such as random

surface sculpting via reactive ion etching eliminate the lithography steps, although with the penalties of increased surface area and deteriorated surface recombination result [19]. In comparison, the latter approach of depositing on textured substrates circumvents high processing cost via simple wet etching [20] or by controlling TCO deposition conditions [22]. However, thin films grown on textured rather than planar substrates can suffer from excessive material defects which disrupt solar cell performance. As an example, micro c-Si and nano c-Si films deposited on textured high haze TCO are plagued with open circuit voltage ($V_{oc}$) degradation due to low-density regions nucleated from valleys on the rough substrates [22, 23]. Finally, all of these low-cost alternatives to lithography essentially rely on self-assembly for structure formation and thus lack deterministic control on the structural parameters, which is critical to effective light management in the wave optics regime. Besides these two main drawbacks, most of the lights trapping methods demonstrated to date are only applicable to one or few solar cell systems. Material-specific issues do exist. For instance, surface roughness on polycrystalline thin film solar cells (e.g. CIGS) complicates or even prohibits integration of wavelength-scale light trapping gratings/PhCs [24]. Chemical compatibility and processing thermal budget are also critical integration challenges that have not been extensively explored.

**Table 1.1** summarizes the key challenges faced by current light trapping schemes. Our proposal of a platform low symmetry grating (LSG) technology applicable to different solar cell systems at low cost and with light trapping efficiency exceeding the Lambertian limit is thus highly desirable for achieving the $1/W strategic goal.

Table 1.1: Comparison between Low Symmetry Gratings (LSG) and Convectional gratings/PhC light trapping Structures

| ***Performance Attribute*** | ***Conventional Random texture and gratings/PhC light trapping designs*** | ***High-index glass Low-Symmetry Gratings(LSG)*** |
|---|---|---|
| **Optical Enhancement** | Average due to insufficient excitation of guided modes and unoptimized optical leakage; bound by the $4n^2$ Lambertian limit | Low symmetry and high refractive indices of glass (> 3) lead to strong enhancement exceeding the $4n^2$ limit |
| **Solar cell material degradation** | Surface deterioration due to increased surface area and etch-induced defects; growth defects can result in thin film cells on textured substrates | The semiconductor surface remains intact and planar during processing |
| **Processing complexity & cost** | High due to the fine-line lithography steps; complicated gray-scale lithography needed for asymmetric structure fabrication | Low; amenable to large-area single stepimprint/molding for fabrication of LSG even with complex geometries |

## 1.2 Proposed Methodology

### 1.2.1 Low-Symmetry Grating (LSG) Fabrication

In this project we propose to develop novel wavelength-scale low-symmetry gratings (LSG) fabricated in high refractive-index glass using low-cost nanoimprint/molding and/or Reaction-diffusion wet etching stamping (RD-WETS) techniques as the light trapping solution. This approach promises light trapping enhancement exceeding the conventional Lambertian limit by coupling the out-of-plane incident solar radiation into guided wave modes in the solar cell slab, which dramatically increases the effective optical path length. A generic 2-D LSG configuration consisting of a periodic array of asymmetric structural units (a skewed

pyramid is shown in **Figure 1.1** as an example) on a 2-D oblique Bravais lattice is schematically illustrated in Fig.1. A novel characteristic of LSG distinguishes our approach from previous gratings/PhC designs and constitutes the key to light trapping beyond the Lambertian limit: the inherent low symmetry of both the skewed structural unit and the 2-D oblique Bravais lattice ensures that all guided modes, irrespective of their symmetry, are excited and contribute to light trapping enhancement. According to recent theoretical analysis by Yu et al. [15] and Han et al.[16], effective excitation of guided modes with different symmetric properties is critical to maximizing light trapping efficacy beyond the Lambertian limit, which motivates the LSG design. In practice, the versatile LSG structures can be integrated either on frontside of substrate solar cells or on backside of superstrate solar cells (**Figure 1.2**) to offer light trapping enhancement.

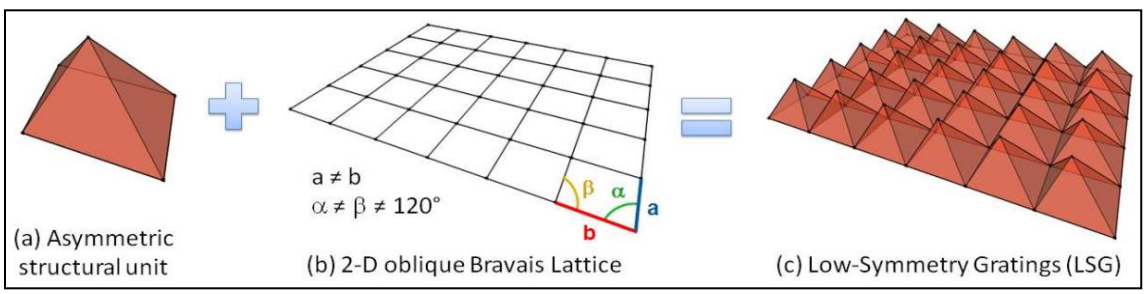


Figure 1.1: Construction of 2-D LSG; the low structural symmetry distinguishes the proposed design from prior work and is the key to ultimate light trapping enhancement exceeding the $4n^2$ Lambertian limit. Note that the skewed pyramidal shape of the structural unit is only an example to illustrate low structural symmetry; the optimized LSG structural unit may be of completely different geometry

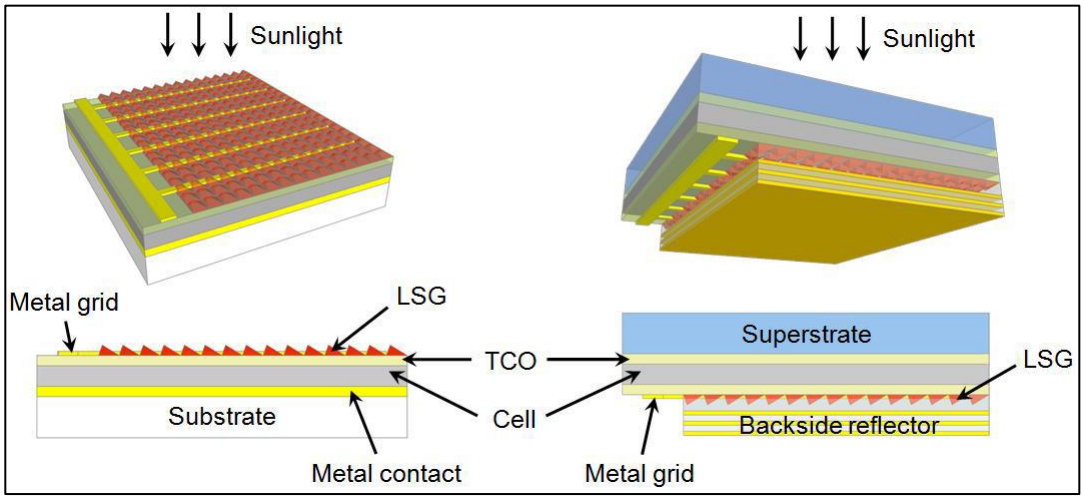


Figure 1.2: Schematic tilted view (top) and cross-sectional (bottom) illustrations of LSG integrated solar cells with a substrate configuration (left) and a superstrate configuration (right). Figures are not drawn to scale.

Besides low structural symmetry, several other features are incorporated in the LSG design to maximize light trapping enhancement. A pyramidal unit shape generates a gradual grading of effective refractive index when light enters the grating, which minimizes Fresnel reflection when LSG is used as frontside light trapping structures. The lattice parameters are chosen to be smaller than the band edge wavelength in order to suppress phase matched optical back-coupling (i.e. leakage) from guided modes back to free space. These features combined point to a > 3xoptical path length increase compared to the Lambertian limit in optimized 2-D LSG [15], corresponding to a dramatic 160x absorption enhancement in ultra-thin solar cells.

# Chapter 2

# THIN FILM GLASS MATERIALS

## 2.1 Material Selection

The proposed effort deals with fabrication of the LSG structures in a layer of high-index-glass deposited on solar cell surface. The choice of fabrication technique that maintains the active material surface integrity and possesses low defects to eliminate recombination center is desired.

The gratings will be comprised of high-index glasses such as chalcogenide glasses (suitable for backside gratings) and multi-component oxide glasses or their amorphous alloys (suitable for front side grating). These glass materials possess the following suitable properties, making them potential candidates for LSG: **(1)** high refractive index [25]; **(2)** Optical transparency in entire visible and near IR spectrum; **(3)** they can be deposited uniformly using low-cost techniques compatible with roll-to-roll processing such as thermal evaporation [26], sputtering [27], sol gel processing [28, 29]; **(4)** their amorphous nature enables monolithic integration on virtually any solar cell substrate/superstrate; **(5)** gratings with complex asymmetric shapes can be fabricated in them using low cost techniques such as single step nanoimprint [30,31] and/or alternatively reaction-diffusion wet stamping techniques [32,33].

There are possible material and processing challenges encountered in selecting novel glass films for thin c-Si PV application. Table 2.1 present a list of challenges and proposed solutions. These solutions and other attractive materials properties

explained in this chapter provided the navigation map for materials selecting and suitable low cost processing techniques.

Table 2.1: Challenges of novel glass for light trapping applications

| Challenges | Proposed Solution |
|---|---|
| **Diffraction efficiency** | High index (n > 2) grating materials |
| **Gray-scale patterning** | Thermal Nanoimprint |
| **Surface recombination increase** | Use deposited gratings to maintain semiconductor surface integrity |
| **Processing cost** | Monolithic imprint patterning |

### 2.1.1 Glass Thin Film Materials for Front Side Thin c-Si Solar Cells

Multicomponent metal oxide glasses such as amorphous $TeO_2$-$Bi_2O_3$-ZnO alloy glass system (tellurites) with large optical band gap energies ($E_g$ > 3 eV) [34] is a suitable candidate for front side low symmetry grating structure on thin film solar cell. Tellurite glasses (containing $TeO_2$ or tellurium dioxide as the main component) have attracted much attention due to their amorphous nature, high refractive index (n > 2), peculiar non-linear optical properties, excellent infrared transmittance, low phonon energies, good chemical durability and low melting temperatures [35, 36]. These glasses are highly transparent from around 400 nm to ~ 6 µm in the mid-infrared, have high acoustic-optic figures of merit (three times that of quartz) [37], large Raman shifts (up to 1200 $cm^{-1}$ in some compositions) [38] and large Raman coefficients (~ 60 times silica) [27]. Besides, tellurite glasses are relatively thermally and mechanically

stable, glass transition temperature ranging 240-430 $^{o}$C shown in various compositions with high tellurite content [37, 39].

It has been shown that tellurite glasses combined with heavy metal oxide display interesting physical and optical properties [36]. Tellurite glasses are capable of incorporating large concentration of rare-earth ions such as $Er^{3+}$, $Tm^{3+}$, $Ho^{3+}$, $Pr^{3+}$, etc., displaying additional transitions not seen in silica for example at 1300nm and beyond 2000nm which are crucial for future active integrated optics components into the matrix [40, 41, 42]. Pao et al demonstrated broadband and anisotropic light emission capability of rare-earth doped tellurite thin films using $Er^{3+}$- $TeO_2$ photonic crystals [42].

As a result of this profound applicability of $TeO_2$-based glasses, it is pertinent to understand the structure of the parent compound that constitutes these glass systems to clarify the nature of the relevant glass properties. The structure of tellurite glasses has been extensively studied starting from the crystalline $TeO_2$ [37]. Conventionally, crystalline $TeO_2$ exist in two polymorphs in ambient temperature: tetragonal $\alpha$-$TeO_2$ (paratellurite) [43] and orthorhombic $\beta$-$TeO_2$ (tellurite) although in the last years new crystalline phases have been reported. In both structures, tellurium atoms have four neighboring oxygen atoms and the basic structural unit is a $TeO_4$ disphenoid, or taking into account the $5s^2$ lone pair of tellurium atoms, a distorted $TeO_4$ bipyramid [44] shown in **Figure 2.1**. This unit has the shape of a trigonal-bipyramid (tbp), formed by two inequivalent pairs of oxygen atoms: two equatorial oxygens ($O_{eq}$) at a distance of 1.9 Å from the Te atom and two axial oxygens ($O_{ax}$) at 2.1 Å. The tbp is distorted due to the Te electron lone pair, placed in the equatorial plane. The angle $O_{eq}$-Te- $O_{eq}$ is 102.0$^{o}$ while the angle $O_{ax}$-Te-$O_{ax}$ is 168.5 $^{o}$ [45]. The crystalline network is built up

by [$TeO_4$] tbp units with each oxygen atom shared by two units and bonded in the equatorial position to one Te atom and in the axial position to another (Te-$_{eq}O_{ax}$-Te linkages).

Tellurium dioxide ($TeO_2$) is a conditional glass former because it does not have glass forming ability under normal quenching conditions without the addition of a secondary component such as alkali oxide, an alkaline-earth oxide, a transition-metal oxide, or another glass former[ 46, 47]. Addition of a network modifier or an intermediate oxide, to tellurite glasses modifies its structure and provides several advantageous properties, such as doping with rare earth elements in a wide range, modifying the composition by a third, fourth, and even fifth component, enhancing the chemical stability and devitrification resistance. Studies [48] and numerous spectroscopic techniques such as infrared [49], Raman [48], and X-ray spectroscopy [50, 51] have shown that $TeO_2$-based glasses consist of low symmetric structural units such as $TeO_4$ trigonal bipyramid and $TeO_3$ trigonal pyramid. It is also well known that addition of $Bi_2O_3$ and ZnO enhances the glass polymerization by creating chain-like structures of Te-O-Te increasing the tendency of glass formation [52].

Fabrications of high-quality planar devices such as waveguide from these glass materials require two approaches. The first involves fabrication on waveguides by processing a bulk glass substrate modifying the refractive index locally to form the core or bottom cladding. This has been demonstrated in tellurite using UV direct write [53], femtosecond laser direct write [54, 55], ion exchange [56, 57] and ion plant [58, 59]. The second approach involves patterning thin films on another substrate either directly by lift off or by post processing with wet etching [60], sputter etching [61], reactive ion etching (RIE) [27] or thermal nanoimprint [30,62].

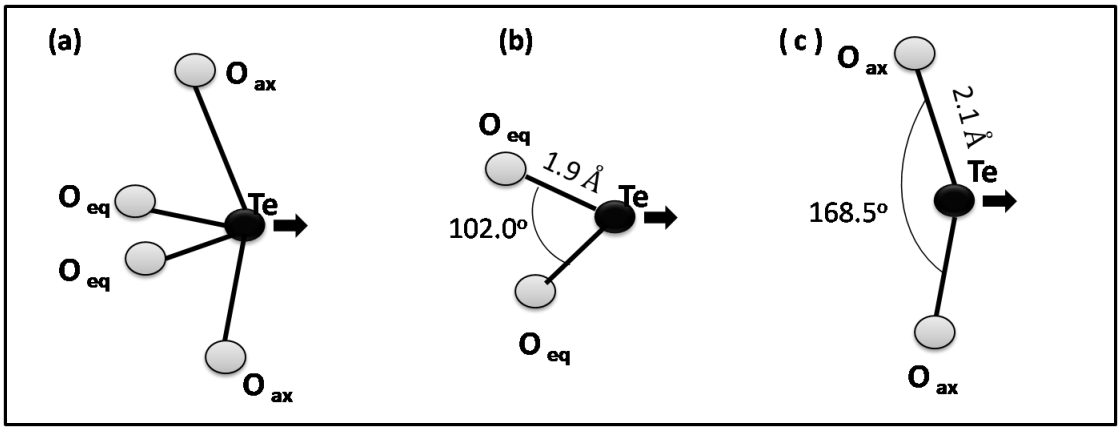


Figure 2.1: Structural model for (a) $TeO_4$ trigonal bipyramid structural unit which is formed by two dissimilar pair of oxygen atoms; (b) two equivalent oxygen ($O_{eq}$) and (c) two axial oxygen ($O_{ax}$). The arrow indicates the position of the electron lone pair of $Te^{4+}$ [50].

Film formation is clearly a critical part of the process and reactive sputtering is currently the most mature method for controlling film stoichiometry microstructure and composition for attaining low-loss high-quality films [27,63].The optical and structural characteristics of sputtered $TeO_2$ based thin films of tellurium dioxide strongly depend on its chemical composition and parameters of growth (such as fabrication method, deposition rate, deposition temperature, annealing conditions and film thickness) [64,65].

### 2.1.2 Glass Thin Film Materials for Back Side Thin c-Si Solar Cells

Chalcogenide thin films have attracted a great deal of attention because they can be used in solar cell, microelectronics, optics, magnetic, laser devices and gas sensor application. Chalcogenides are comprised of covalently bonded heavy elements with weaker inter-atomic bonds compared to those in oxides and this gives them some

unique properties for infrared optics applications. The bonds have low vibrational energies making them transparent in the near and mid-infrared region [66]. Their high glass densities compared to oxide glasses coupled with strong polarization effect lead to high refractive index of n = 2-3.

Conventional techniques of chalcogenide glass film deposition, such as spin-coating of glassy films from solution, thermal evaporation and sputtering demonstrates deposition of thick film over a large area. Thermal evaporation is a simple, low-cost method and produces glass thin films with large-area uniformity. Previous report has shown that high-quality chalcogenide glass films can be evaporation deposited at rates ranging from 200 nm/min to 500 nm/min [67], which points to a total deposition time of < 1 min suitable for high-throughput processing.

For back side material for light trapping material in thin c-Si solar cell, thermal evaporated chalcogenide glass film with composition of $As_{20}Se_{80}$ is chosen because it exhibits required properties such as (i) uniform thickness with low surface roughness, (ii) Relatively similar composition and chemical structure compared with the bulk glass and (iii) excellent optical properties with high refractive index (iv) Low $T_g$ and viscosity compared to other compositions such as $As_{20}Se_{60}$ (v) Low imprinting temperature compatible with PDMS stamps and solar cells processing. These attractive properties meet the requirements for ideal back-side LSG materials for light trapping. In this study, low symmetric gratings will be imprinted on thin film $As_{20}Se_{80}$ at backside of thin c-Si solar cell.

# Chapter 3

# LIGHT TRAPPING THEORY AND DESIGN

## 3.1 Optics and Device Physics of Low Symmetric Diffraction Grating for Thin Film c-Si Cells

Diffraction gratings are optical components with a periodic structure which separate light into its component wavelengths. They consist of a series of closely packed grooves that have been engraved or etched into the grating's surface. Diffraction gratings can be either transmissive or reflective. As light transmits through or reflects off a grating, the grooves cause the light to diffract, dispersing the light into its component wavelengths. Diffraction directions of the beams depend on the period of the gratings and the wavelength of the light. The diffraction angles are given by the grating equation: $\theta s = \sin^{-1}(m\,\frac{\lambda}{\Lambda} + \sin\theta i)$, where $\theta s\ and\ \theta i$ are diffraction angle and incident angle, respectively, $m$ is the diffraction order, $\lambda$ is the wavelength of laser beam, and $\Lambda$ is the period of the gratings.

In thin film solar cells when the thickness becomes comparable to wavelength, the conventional ray optics argument fails. Also, when the light trapping grating period approaches wavelength-scale, the basic assumption of ergodicity no longer holds [68]. Finally, the density of photon states may also deviate from the bulk value in thin film guided wave structures [15]. Consequently, wave optics takes over in the new nanophotonics light trapping regime. In this study, we apply the temporal coupled mode theoretical formalism in wave optics pioneered by Yu et al. [69] to the LSG configuration. In the framework of the coupled mode theory, light trapping works by

coupling incident light into guided modes to increase optical path length (coupling light "in"), however any back-coupling (i.e. optical leakage "out") from these modes to free space can reduce optical enhancement. The theory specifies that the optical path length enhancement factor *E* is determined by the number of accessible guided modes in the solar cell as well as back-coupling from guided modes to free space, and can be written as:

$$\mathrm{E} = \frac{2\,\pi\,c\,M}{n\,d\,N} \tag{2.1}$$

where *c* is the light velocity, *n* is the cell material refractive index, *d* is the solar cell thickness, *M* denotes the number of accessible modes per unit optical frequency interval, and *N* represents the number of phase-matched optical leakage pathways. Eq. (2.1) suggests that optimal light trapping is attained by maximizing the number of optical modes *M* contributing to light trapping, and minimizing optical leakage channel number *N* to maintain guided mode enhancement. In conventional grating/PhC light trapping designs, structural symmetry limits the accessible modes to those sharing the same symmetric properties with the light trapping structure. For example, mirror symmetry prohibits coupling into anti-symmetric modes and cuts the mode number *M* by half. The low symmetry inherent to the LSG design thus maximizes *M* by ensuring all modes, irrespective of their symmetry, are excited and contribute to light trapping.

On the other hand, the number of optical back-coupling pathways can be calculated by considering the phase-matching condition in a periodic medium (i.e. the Laue equation of diffraction):

$$\overline{k_{//,\mathrm{d}}} = \overline{k_{//,\mathrm{i}}} + \overline{\mathrm{G}} \tag{2.2}$$

where $k_{//,i}$ and $k_{//,d}$ denote in-plane (parallel to solar cell surface) wave vectors of incident light and light diffracted back to free-space, respectively, and G is a reciprocal lattice vector of the gratings. Due to the grating periodicity, the in-plane wave vector of light diffracted back to free space can only take discrete values specified by Eq. (2.2). Since each possible $k_{//,d}$ value correspond to an optical leakage pathway satisfying the phase-matching condition, N is exactly the number of possible $k_{//,d}$ values. Following the argument, N can be most conveniently solved graphically. **Figure 3.1** shows an example of graphic solution for normal incidence light (i.e. $k_{//,i}$ = 0). In free space, $|k_{//,d}| < |k_0|$. Therefore the number of reciprocal lattice points inside the circle gives the value of N. Here, N is a function of LSG lattice type, basis parameters, wavelength, and incidence angle. Another important conclusion from the discussion is that structural periodicity is essential to minimal guided mode leakage, as the phase-matching condition does not need to be strictly obeyed for light to escape from guided modes in random structures; and optical enhancement in random structure thus always is inferior to the Lambertian limit.

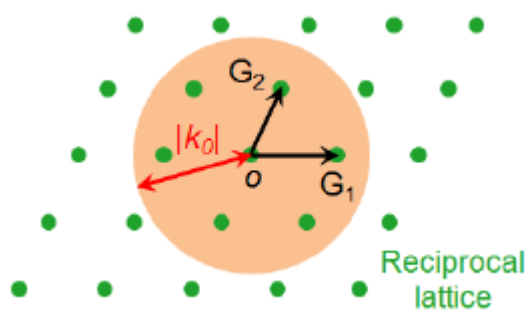


Figure 3.1: Graphic solution of the number of optical leakage pathways N. $k_0$ is the free space wave vector, and G1 and G2 are bases of the LSG reciprocal lattice. The lattice points inside the shaded circle gives the possible values of $k_{//,d}$. In this specific example, N = 7.

Based on this insight, the theoretical investigations analytically evaluate the impact of key LSG parameters on accessible optical mode density and optical leakage pathways. These parameters include grating lattice type, period, symmetric properties, and light incident angle. Expected outcome from the analysis clarifies the fundamental mode coupling mechanisms contributing to light trapping, and establish an optimized set in the parameter space which leads to complete excitation of modes in the over coupling regime (maximum $M$) and a minimum $N = 1$ for subsequent numerical design and modeling. The condition $N = 1$ suggests that the only out coupling channel is through zero order diffraction, i.e. direct back reflection from grating surface, which can be further minimized by appropriately tapered structural unit design to provide anti-reflection functionalities.

Numerical simulations, on the other hand, solve for the optimized LSG structural unit design which the analytical theory cannot provide. The Rigorous Coupled Wave Analysis (RCWA) approach is the primary numerical method given its superior computation efficiency in modeling periodic structures, which was also complemented by the Finite-Difference Time-Domain (FDTD) method for cross-checking results and numerical convergence. We note that each LSG structural unit design involves a large set of parameters characterizing the unit's geometric shape and refractive index distribution. Therefore multi-parameter optimization algorithms can be implemented. Genetic evolutionary algorithm and particle swarm optimization are two promising approaches we explored, as both techniques have been demonstrated to be mature photonic design optimization algorithms.[70, 71, 72]

Besides design optimization, we also evaluated the impact of LSG fabrication imperfections (e.g. pattern distortion, edge roughness, etc.) on light trapping by FDTD

simulations to ascertain the structural fabrication tolerance. It is expected, however, that given the level of pattern fidelity achieved by imprint and the broadband nature of solar radiation, the remaining defects in LSG gratings probably do not have a significant impact on the light trapping performance, as is also confirmed by other groups[73].

The combined analytical and numerical studies yielded fundamental understandings into the optics and device physics of LSG light trapping enhancement, and derive LSG design principles and optimized device parameters to guide high-index glass material and processing studies.

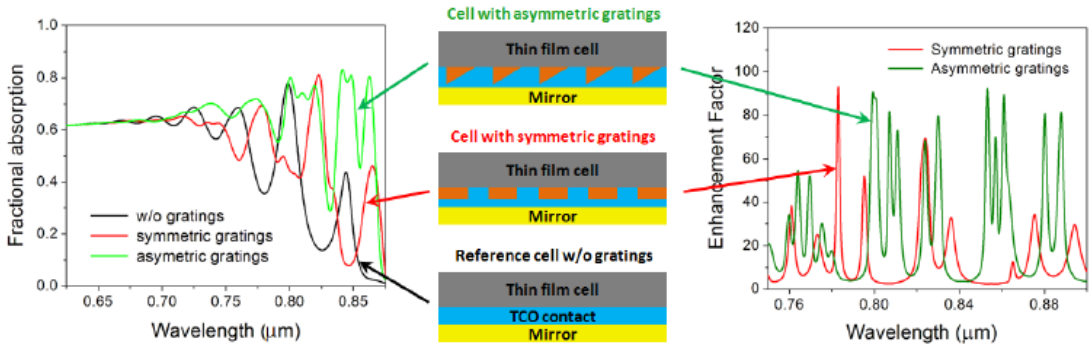


Figure 3.2: (Left) Absorption of a-Si thin film cells with and w/o backside structures; note that only the band edge regime is shown for clarity; (center) schematics of cell structures with a backside grating configuration; 1-D gratings with respect to single-pass absorption.

As a proof-of-concept of LSG designs, we performed preliminary simulations of light trapping using 1-D gratings. Note that the Lambertian limit in the 1-D case is given by the enhancement factor $\pi n$, and is lower than the 2-D factor $4n^2$ as only 1-D guided modes are considered. The simulations were conducted in a 1.5 μm thick c-Si

solar cell using 1-D asymmetric sawtooth gratings, as well as using a traditional symmetric rectangular grating for comparison. The period, grating height, and duty cycle were optimized in both asymmetric and symmetric cases, and for both front and backside configurations. For cells with backside gratings and normal incidence solar radiation, the optimized asymmetric gratings generate a 25% increase of short circuit current relative to cells without gratings and an average light trapping enhancement of 25x in the weak absorption regime (750 - 900 nm for c-Si); these levels are far superior compared to the 12x enhancement of optimized symmetric gratings as well as the Lambertian limit of 11x. Such performance is realized because ~ 2x more guided modes are excited with asymmetric gratings as is evident in **Figure 3.2** (right), where each excited guided mode shows up as a resonant peak. Substrate-configuration cells with frontside asymmetric gratings of the same refractive index claims an optical trapping enhancement factor of 18x, again boasting ~ 2x improvement compared to enhancement in cells of an identical configuration but with symmetric gratings (10x). We have also validated our design in c-Si cells and demonstrated similar enhancement factors between the 800 - 1100 nm c-Si band edge ranges in our experimental results presented in discussed in details in chapter 7 of this thesis.

## 3.2 Investigation on Impact of Refractive Index in Optical Enhancement

The impact of grating material refractive index on light trapping is investigated as well. **Figure 3.3** plots the optical path length enhancement factor spectrum-averaged over the a-Si band edge regime as functions of grating refractive index in both symmetric and asymmetric 1-D grating cases. Clearly, high index gratings lead to stronger diffraction effects and hence improved light trapping. From a coupled mode theory perspective, high-index gratings increases coupling into guided modes in solar

cells and thus generally favor guided wave resonance in the over coupling regime, which maximizes the modal spectral absorption cross-section[69]. The figure also suggests that optimized light trapping using LSG can be achieved by using high-index chalcogenide glasses such as As-Se-Te (n ~ 3.5). Such glasses, however, are only suitable for backside structures as their absorption edge locates at ~ 1100 nm wavelength. For frontside structures, the maximum index offered by transparent bismuthate oxide glasses is ~ 2.5, which is still capable of offering light trapping enhancement exceeding the Lambertian limit according to **Figure 3.3**.

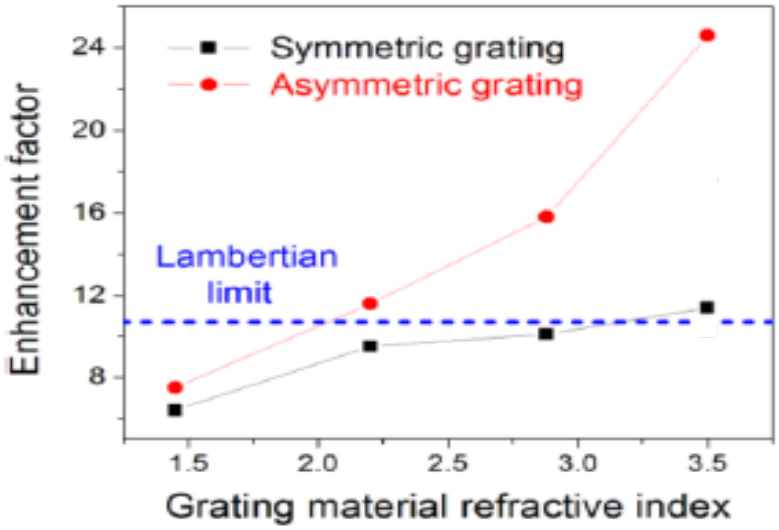


Figure 3.3: Normal incidence optical path length enhancement factors of 1-D gratings as functions of grating material refractive indices; the open and filled dots correspond to front and backside structures, respectively; the blue line represents the 1-D Lambertian limit

# Chapter 4

# SPUTTERED TELLURITE GLASS THIN FILMS

## 4.1 Introduction to Sputtering of Tellurite Glass Thin Film

Tellurite glasses (containing $TeO_2$ as the main component) have attracted much attention for photonic applications due to their high refractive index (n > 2), large acousto-optic effect (three times that of quartz), singular non-linear optical properties (e.g., their Raman coefficients are ~ 60 times higher than that of silica [38]), and can be tailored by knowledge of structural make-up [74], excellent near and mid-infrared transmittance (from around 400 nm to ~ 6 um), large rare earth solubility [40-42], good chemical durability, and compatibility with fiber drawing processes [36, 75]. Despite their hygroscopic nature which leads to loss when drawn into fibers [76], they can be made into property-tailored transparent glass ceramics [77] with specialized melting and heat treatment protocols [78]. This set of unique properties make them strong candidates for applications in optical communications [27], amplifiers, acousto-optic modulators [79], light emitters [40-42], and optical storage devices [81,82]. Since $TeO_2$ under normal conditions does not have the ability to form glass structure easily, multi-component tellurites, $TeO_2$-based glasses containing one or more chemical modifiers like alkali oxides, alkaline-earth oxides, or transition-metal oxides, are of great interest to the aforementioned applications given their much improved glass forming ability [78,82,83] and enhanced optical properties[84]. The superior glass stability of multi-component tellurites allows them to be prepared as

bulk glass by melt quenching [77,85,86] , drawn into optical fibers [82], and even re-melted to form micro-spheres[88]. Planar tellurite thin films, on the other hand, constitute the basic building block for on-chip photonic devices such as waveguide amplifiers and optical modulators. Multi-component tellurite films have been prepared using sol-gel processing [27, 92] and laser ablation [93, 94]. Alternatively, radio frequency (RF) magnetron reactive sputtering has been extensively used for oxide thin film deposition given its great versatility in controlling film stoichiometry, microstructure, and phase composition via tuning deposition parameters, in particular, oxygen partial pressure [95-97]. Thus far the method has only been used to grow $TeO_2$ thin films [27, 95, 98], Er-doped single-component $TeO_2$ films and tungsten tellurite materials [41, 42].

Here we explore RF reactive sputtering for multi-component tellurite film preparation capitalizing on its unique ability to fine tune resulting film stoichiometry and hence optical properties. Specifically, we choose $TeO_2$-$Bi_2O_3$-ZnO (TBZ) glass system as the addition of $Bi_2O_3$ and ZnO enhances glass polymerization by creating chain-like structures of Te-O-Te, and thereby increases the tendency of glass formation [77, 98]. Consequently, the system exhibits superior glass stability and has been successfully used in low-loss optical fiber fabrication [78, 99]. Unlike bulk glass processing or fiber drawing where composition variation during processing is usually minimal, vacuum deposition of thin films is highly susceptible to oxygen loss, and the resulting stoichiometry change has a major impact on film structure and properties While the structure of bulk tellurite glasses has been investigated by several groups [50, 51,100- 103], the structural properties of tellurite thin films, in particular the impact of glass stoichiometry, have been much less studied.

In the following sections, we enumerate the experimental steps used to explore the film composition space by varying the deposition parameters, and discuss chemical, structural, and optical characterization results that elucidate the structure-optical property relation in the TBZ thin film system.

## 4.2 Tellurite Bulk Glass Synthesis and Thin Film Deposition

The bulk glass target used in this study was prepared by melt-quenching from commercial regents. The flow process for bulk glass synthesis is shown in **Figure 4.1**. We carefully selected glass of composition $0.70TeO_2$-$0.10Bi_2O_3$-0.20ZnO (in atomic %) in the tellurite-based $TeO_2$–$Bi_2O_3$–ZnO (TBZ) glass family. High-purity regents ($TeO_2$ Alfa Aesar 99%; $Bi_2O_3$ Alfa Aesar, 99%; ZnO Alfa Aesar, Ward Hill, MA, 99%) are batched and melted in an $O_2$-rich (UHP 305 CF) atmosphere in a platinum crucible at 850 °C for 5–10 min. The melt is then poured on a cold metallic plate to be quenched in a disk-like shape. The glass is annealed for 16 hours at 300 °C, that is to say 40 °C below its glass transition temperature to relax quench-induced mechanical stress. The resulting as-quenched material is depicted in **Figure 4.2(a)**. The glass has a slight yellowish coloration. In order to fit perfectly on the sputter holder, the edges and the top and bottom faces of the glass are precisely polished **(Figure 4. 2(b))**. Melt process optimization was carried out to ensure that robust, large diameter targets could be fabricated to enable deposition of desirable films with target thicknesses. The glass target is subsequently bond on to a copper plate using Silver-epoxy paste (part A & B in 1:1 ratio) and allowed to cure at room temperature for 15-17 hours.

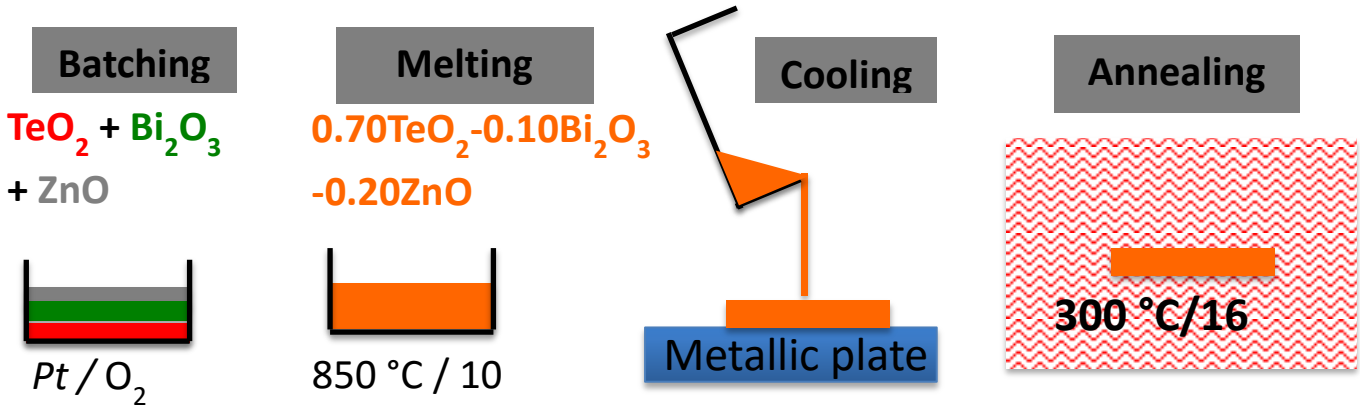


Figure 4.1: Process flow for synthesizing bulk tellurite target for thin film Sputtering

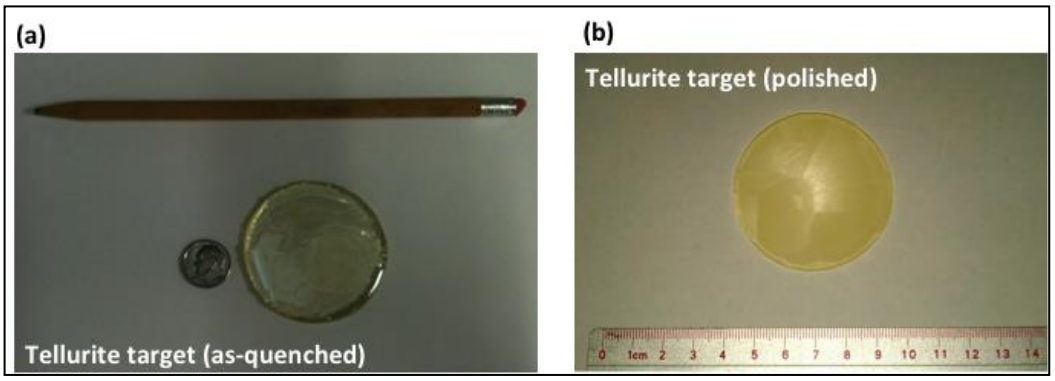


Figure 4.2: Tellurite target for sputtering (a) as-quenched (b) polished in order to fit on the sputter target holder.

Sputtering glass target of composition $(TeO_2)_7$-$Bi_2O_3$-$(ZnO)_2$ [2 inches, 0.25 inches thickness] prepared by melt-quenching method was used for thin film deposition. Thin films were deposited from the target onto substrates (sodalime silicate glass slides from Fisher Scientific Inc. or 3-inches (100) silicon wafers from

University Wafer Inc.) by RF reactive sputtering. The substrate choice has little impact on resulting film properties given the amorphous nature of the films. No changes were observed from characterization results performed on thin films deposited on both substrates. Prior to deposition, the glass substrates were cleaned with $H_2SO_4$-Nochromix® solution while silicon substrates were dipped into buffered oxide etch (BOE) solution for 3 minutes to remove the native oxide layer. The sputter deposition chamber was first evacuated to a base pressure below $10^{-6}$ Torr. The target-substrate spacing is fixed at 13 cm for all deposition. Pre-sputtering was conducted for 10 minutes prior to film deposition, with covered substrates, to clean the surface of the target of any possible contamination. Sputtering was performed, using a custom-designed system (PVD products), in oxygen ($O_2$) and argon (Ar) atmosphere with varying gas flow rates while keeping all other parameters constant to investigate the impact of oxygen stoichiometry change on film properties. The film deposition process parameters are summarized in **Table 4.1**. The low sputtering power of 25 W is specific to tellurite targets in order to avoid target melting and cracking due to large thermal coefficient gradient between copper and $TeO_2$. The deposition rates shown in Table 4.1 were calibrated using a Dektak profilometer. The deposition rate decreases as the oxygen flow rate increases, which was similar to the report on $Bi_2O_3$ [97]. The observed decrease in deposition rates with increasing oxygen content may be derived from the reduced level of energetic Ar+ ions in the plasma. During deposition, the substrates were rotated at 5 rpm to ensure uniform thin film deposition. For each deposition, the films are deposited on both soda-lime and Si substrates simultaneously. The substrates were not intentionally heated and were kept near room temperature

throughout the deposition process. Depending on ratio of Ar:$O_2$ atmospheres, the sputtered films were labeled TBZ1 to TBZ4 as shown in **Table 4.1**.

Table 4.1 : Deposition parameters for reactive sputtering of tellurite films

| Sample name | **TBZ1** | **TBZ2** | **TBZ3** | **TBZ4** |
|---|---|---|---|---|
| RF Power (W) | 25 | 25 | 25 | 25 |
| Sputtering pressure (mTorr) | 2.5 | 2.5 | 2.5 | 2.5 |
| Ar :$O_2$ flow rate(sccm) | 17:0 | 15.3 : 1.7 | 13.6:3.4 | 11.9:5.1 |
| Target-Substrate distance (cm) | 13 | 13 | 13 | 13 |
| Deposition rate (nm/min) | 1.7 | 1.5 | 1.4 | 1.2 |

## 4.3 Optical Characterization

Optical transmittance of the thin films deposited on glass substrates were measured over a wavelength range of 300-1800 nm using an ultra violet-visible (UV-Vis) spectrophotometer (Perkin-Elmer 1050). Refractive index and extinction coefficient of the films were characterized using an M-44 rotating analyzer variable angle spectroscopic ellipsometer [VASE] (J.A. Woollam Co., Inc.) equipped with an autoretarder. Ellipsometry data were collected at three incidence angles: 62°, 67°, and 72° for TBZ1; 66°, 71°, 76° for TBZ2; 69°, 74°, 79° for TBZ3; 66°, 71°, and 76° for TBZ4 which covers the (pseudo) Brewster angle for the tellurite thin films. Variable angle spectroscopic ellipsometry (VASE) data were modeled using the Complete EASE®software. B-spline function [104] was implemented to describe the dispersion

of thin films sputtered in oxygen-rich atmosphere while Tauc-Lorentz model [105] was adapted to modeling the VASE data for thin film sputtered in oxygen-rich atmosphere.

TBZ thin films deposited in mixed $Ar/O_2$ atmosphere show drastically different appearance from those deposited in pure Ar plasma (**Figure 4.3a**). The former samples are optically transparent while the latter are opaque. Similar trends have been made on single-component $TeO_2$ films deposited by reactive sputtering [27, 106]. This observation indicates the important role film stoichiometry plays in dictating the film morphology and physical properties. Here we evaluated the impact of oxygen deficiency on the structural, chemical and optical properties of TBZ films to understand the structural origin of such drastic film appearance difference.

**Figure 4.3b**. shows the UV-Vis optical transmission spectra for TBZ thin films along with that of the glass substrate. All films sputtered in an $Ar/O_2$ environment (TBZ2-TBZ4) exhibit similar spectra, transparent to light above 350 nm wavelength (interference fringe maximums overlap with the glass substrate transmission spectrum), whereas the film prepared in oxygen-deficient atmosphere(TBZ1) show broadband optical absorption in the entire wavelength range measured, consistent with our visual inspection. This broad absorption in the entire visible spectrum indicates that oxygen-deficiency defects may play a role in the opaqueness. This result is similar to the trend observed in RF magnetron sputtering of thin film $TiO_2$ [107-108] where increase in oxygen flow rate improves optical transmittance in $TiO_2$ films and shifts the optical absorption edge of the films to lower wavelengths. Varying interference fringe peaks in the spectrum indicates changes in

growth rate as the oxygen flow rate increases. **Figure 4.3c.**depicts the dispersion diagram measured using VASE.

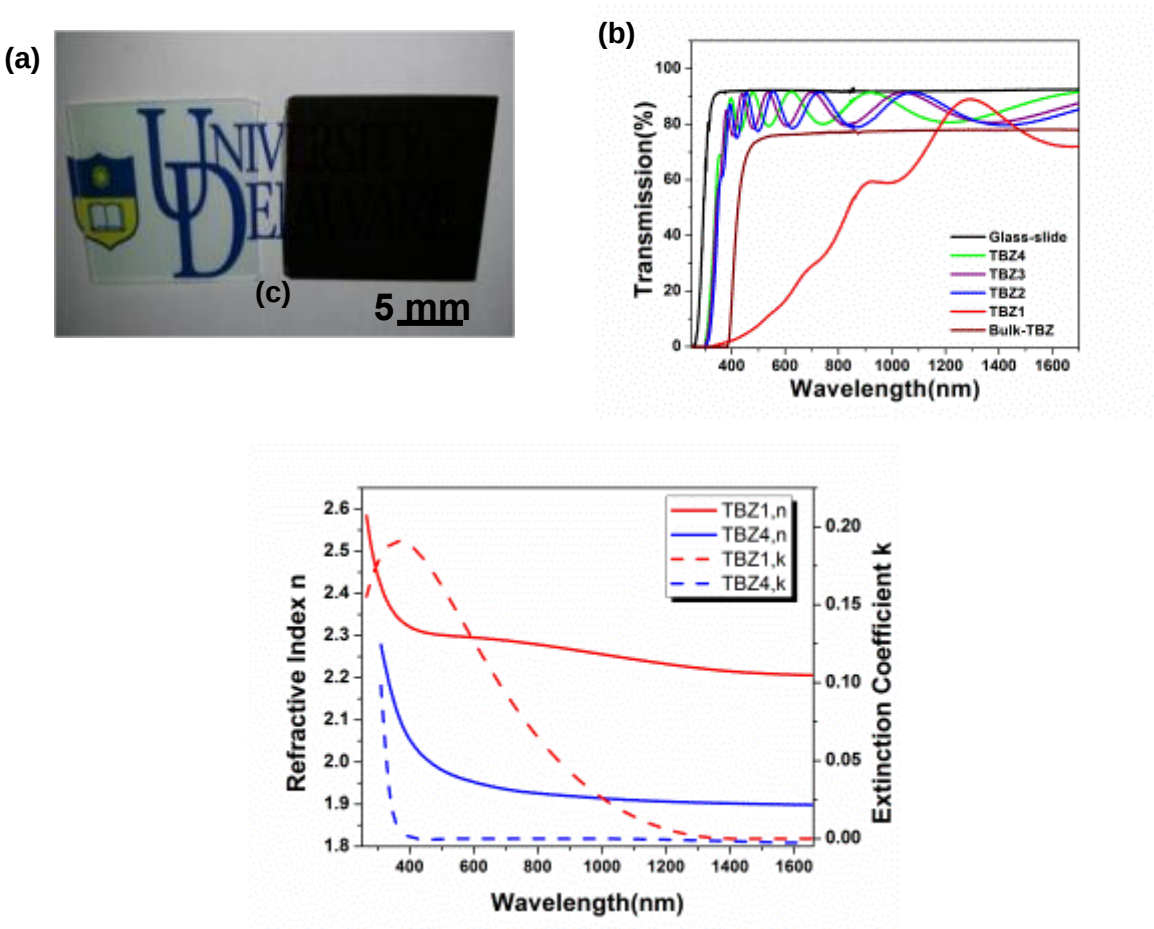


Figure 4.3: (a) Photograph of TBZ4 (left) and TBZ1 (right) on University of Delaware logo for films on sodalime silicate glass substrates deposited under oxygen-rich (L) and deficient (R) conditions; (b)UV-Vis transmission spectrum of sputtered TBZ thin films superimposed on that of glass substrate with varying interference peaks showing thickness change; (c) Refractive index n and extinction coefficient k of sputtered thin films measured by ellipsometry

To validate the fitting model results from ellipsometry, the fitted *n* and *k* data were used as an input to a transfer matrix model to reproduce the optical transmission spectra measured by UV-Vis photo-spectrometry. **Figure 4.4a** shows the flow chart for comparing the transmission spectrum from fitted ellipsometry model with that from experiment; UV-Vis data. Transmission spectra for the samples TBZ1 and TBZ4 simulated using the transfer matrix method were compared with their UV-Vis spectra as shown in **Figure 4.4b.** The excellent agreement confirms the validity of our ellipsometry fitting models.

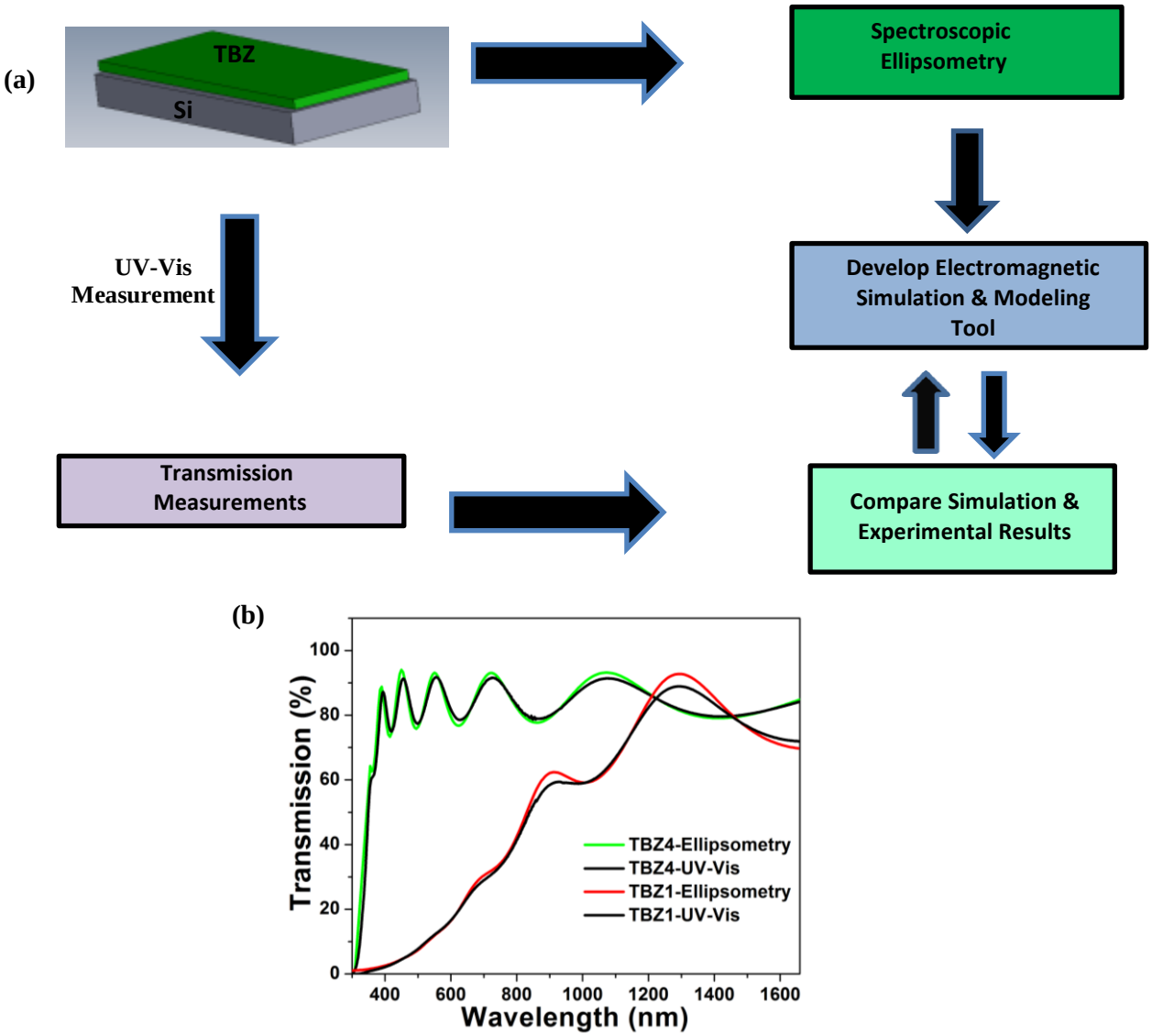

Figure 4.4: (a) Flow chart for comparing the transmission spectrum fitted ellipsometry model and UV-Vis data; (b) Transmission spectrum comparing fitted ellipsometry model and UV-Vis data.

## 4.4 Morphological and Structural Characterization

The surface and cross sectional morphology of the resulting tellurite films were examined using a JSM 7400F scanning electron microscope (SEM) system operating with an accelerating voltage of 3kV and transmission electron microscope (TEM) observations were taken on a JEM-2010F system operating at an accelerating voltage of 200 KeV. The samples were covered with a thin (~ 30 nm) Au/Pd coating prior to SEM imaging to minimize charging from electron accumulation on the sample surface. Samples for TEM (thickness < 100 nm) were prepared using focused ion beam (FIB) on a Zeiss Auriga™ crossbeam nano prototyping station(Schematics of Focused Ion Beam TEM sample prep is shown in **Figure 4.5 e**). Surface roughness of sputtered thin films was measured through atomic force microscopy (AFM) on a Dimension 3100 (Digital Instruments, Inc.) microscope. Silicon AFM probes (Tap 150-G from Budget Sensors, Inc) with a force constant of 5 N/m and resonant frequency of 150 KHz were used. The structural properties of the TBZ thin films deposited under different working gas (oxygen content) conditions were analyzed by glancing incident angle X-ray diffraction (GIXRD) using a Rigaku Ultima IV system equipped with Cu-$K_\alpha$ radiation ($\lambda$=0.15406 nm) at 40 kV and 40 mA.

**Figure 4.5a & b**. show SEM cross-section images of TBZ thin films deposited on silicon substrate at varying oxygen flow rates. The SEM cross-section images of all the thin films are similar in morphology but have different thickness. It can be seen that the thin films have a uniform and dense micro-structure. **Figure 4.5c&d**. show the TEM images of TBZ1 and TBZ4 films on silicon. The corresponding selected area

electron diffraction (SAED) patterns show a diffuse broad diffraction ring approximately at same position indicating that both films are amorphous. The dark and bright spots present in TEM images are atomic columns confirming that a homogeneous amorphous phase is present in the thin films. The amorphous nature of all thin film samples was also confirmed using GIXRD: the spectra shown in **Figure 4.5f** features a broad peak centered at $2\theta = 28.1^{o}$, consistent with previous reports on the bulk amorphous $TeO_2$-$Bi_2O_3$-ZnO system [77]. The results of thin film microstructure analysis, which asserts the amorphous nature of the sputtered TBZ films, are not surprising given the low substrate temperature. An average RMS value of (0.7 ± 0.02) nm was observed on the thin films.

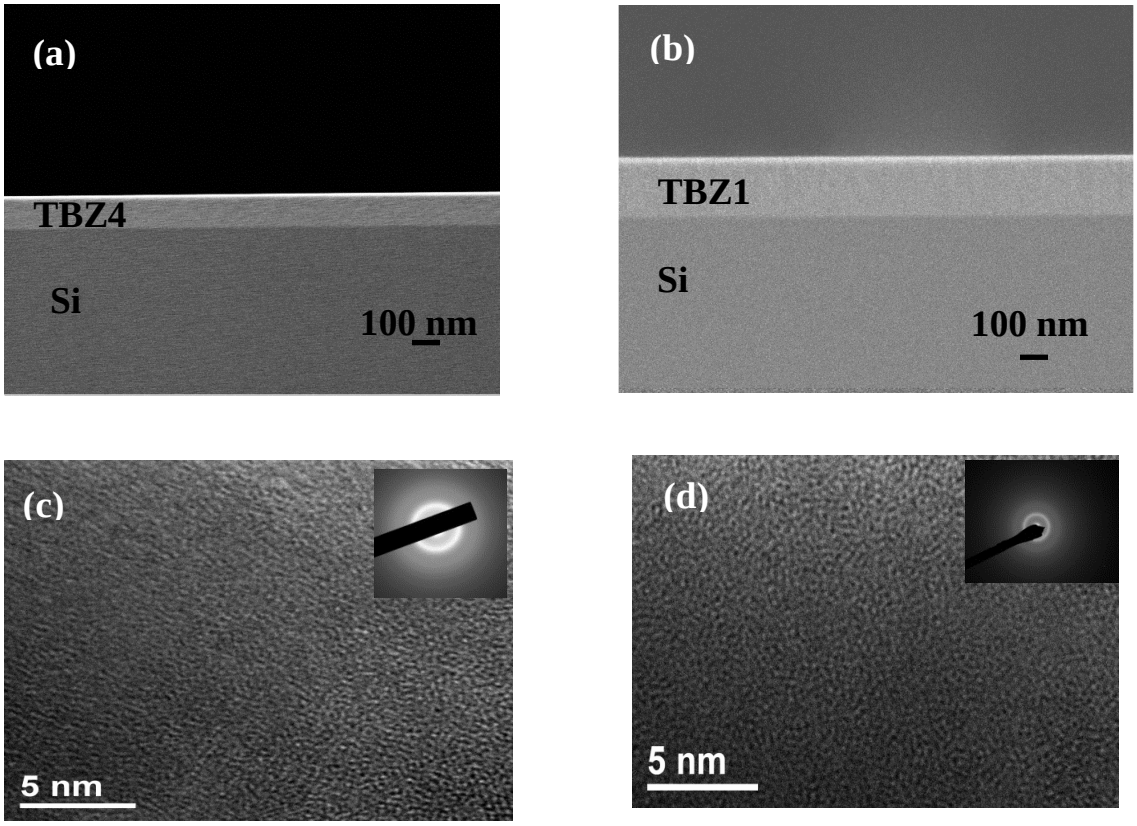

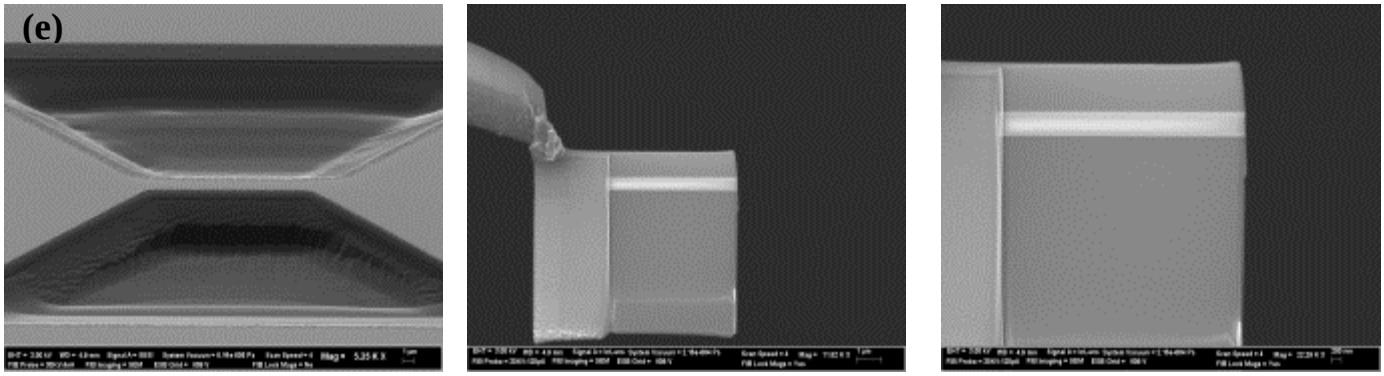


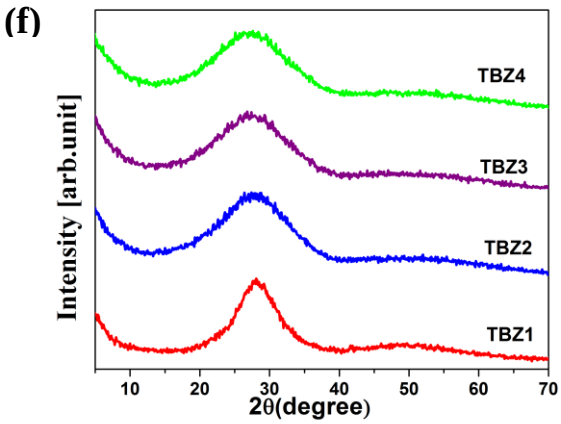


Figure 4.5: SEM Cross-sectional view of sputtered (a) TBZ4 & (b) TBZ1 on Silicon wafer; High resolution TEM images and selected area electron diffraction patterns (inset)of (c) oxygen-rich (TBZ4) (d) oxygen-poor (TBZ1) tellurite films;( e) Schematics of Focused Ion Beam TEM sample prep; (f ) Glancing incident angle X-ray diffraction spectra of TBZ thin film

## 4.5 Compositional and Chemical Analysis

Compositional analysis was carried out using wavelength dispersive spectroscopy (WDS) on a JXA-8200 electron microprobe analysis system. Three points were analyzed per sample in measuring the k-ratios of the samples. The X-ray lines and standards used for data analysis are: Te: TeLα, $Ag_2Te$ (Silver Telluride), Bi: BiMα, BGO (Bismuth Germanium Oxide), Zn: ZnKα, ZnO (Zinc Oxide), O: O Kα,

BGO (Bismuth Germanium Oxide).The raw data were corrected for matrix effects with the PAP method using the General Motor Research film (GMRFILM) software thin-film analysis program. Chemical bonding states in TBZ thin films were examined using X-ray photoelectron spectroscopy (XPS). XPS spectra were recorded on an Omicron EA125 system equipped with dual aluminum-magnesium anodes using non-monochromatic Al-$K_\alpha$ (*hv*=1486.6 eV) radiation at room temperature and chamber vacuum below $2\times 10^{-7}$ Pa. Survey and high resolution spectra were collected at constant analyzer energies 50 eV and 25 eV with step sizes of 1.0 eV and 0.05 eV respectively.

Compositions of the TBZ films as measured using WDS are tabulated in **Table 4.3**.The average error in WDS measurement is ± 0.6 %. It was found that the elemental composition of Ar sputtered (TBZ1) thin films are close to the bulk target composition, whereas films sputtered in $Ar/O_2$ environment become further oxidized. It is interesting to note that (i) all the sputtered films have a Bi/Zn ratio of approximately 0.9 versus 1 in the bulk glass and (ii) the Bi/Te and Zn/Te ratios in the $Ar/O_2$ sputtered films are also lower than the bulk glass but this is not the case for the TBZ1 film. Both observations are suggestive of a degree of preferential elemental sputtering. The latter finding is confirmed by the measured increase of oxygen concentration. The conclusion was further confirmed by Energy-Dispersive X-ray (EDX) spectroscopy and XPS composition analysis.

Table 4.3: Atomic composition of sputtered tellurite films measured using wavelength dispersive spectroscopy. The average measurement error is 0.6 %.

| **Sample ID** | **Te Atomic %** | **Bi Atomic %** | **Zn Atomic %** | **O Atomic %** |
|---|---|---|---|---|

| | | | | |
|---|---|---|---|---|
| **Bulk** | **23.3** | **6.7** | **6.7** | **63.0** |
| **TBZ1** | **22.7** | **6.6** | **7.5** | **63.1** |
| **TBZ2** | **16.8** | **4.2** | **4.5** | **74.5** |
| **TBZ3** | **17.9** | **3.7** | **4.1** | **74.2** |
| **TBZ4** | **17.1** | **3.9** | **4.3** | **74.7** |

XPS measurements were performed to elucidate the chemical state of elements in the bulk and thin films. Relatively low resolution X-ray photoelectron survey scan in the binding energy region 0-1200 eV were recorded for each sample and a typical spectrum for the TBZ bulk and thin film is shown in **Figure 4.6a**. Peaks belonging to Tellurium, Oxygen, Bismuth, Zinc and Carbon were observed in the spectra. The presence of C1s peak at 284.6 eV, associated with post-deposition hydro-carbon contamination [97, 109], is used as internal energy reference to determine the binding energy (B.E) of the XPS spectra. High resolution spectra of Te3d, Bi4f, Zn2p and, O1s orbitals for TBZ bulk and thin films were collected. Peak fitting was performed using mixed Guassian (70 %)-Lorentzian (30%) curves, defined in the CasaXPS software® as GL(30), to obtain the peak positions and full width at half maximum (FWHM). The curve fitting satisfies the following constraints: (a) orbitals relative peak area ratios; (b) each doublet has equal full width at half-maximum (FWHM); and (c) the spin orbit splitting of orbital [110]. The peak positions for core levels Te3d, Bi4f, Zn2p orbitals are listed in **Table 4.4a** while the curve fitting parameters for Te3d core level are **in Table 4.4b**.

Table 4.4a: Core level binding energies of tellurium, bismuth, and zinc for bulk and sputtered tellurite thin films.

| | Binding Energies (eV) | | | | |
|---|---|---|---|---|---|
| | Bulk | TBZ1 | TBZ2 | TBZ3 | TBZ4 |
| **Bi4f$_{7/2}$** | 158.80 | 159.12 | 159.23 | 159.32 | 159.33 |
| **Bi4f$_{5/2}$** | 164.11 | 164.42 | 164.51 | 164.62 | 164.63 |
| **Te3d$_{5/2}$** | 575.79 | 576.16 | 576.48 | 576.41 | 576.40 |
| **Te3d$_{3/2}$** | 586.16 | 586.56 | 586.84 | 586.77 | 586.75 |
| **Tell3d$_{5/2}$** | 573.49 | 573.73 | 574.07 | 574.10 | 574.11 |
| **Tell3d$_{3/2}$** | 583.84 | 584.13 | 584.39 | 584.55 | 584.41 |
| **Zn2p$_{3/2}$** | 1021.26 | 1021.93 | 1021.76 | 1021.64 | 1021.80 |
| **Zn2p$_{1/2}$** | 1044.36 | 1044.93 | 1044.79 | 1044.69 | 1044.90 |

Table 4.4b: Details of the Curve Fitting of Te3d Core Level Spectra

| | | FWHM | Area | background | Line Shape |
|---|---|---|---|---|---|
| **BULK** | **Te3d5/2** | **1.860** | **115082.4** | **Shirley** | **GL (30)** |
| | **Te3d3/2** | **1.814** | **76759.9** | **Shirley** | **GL (30)** |
| | **Tell3d5/2** | **2.141** | **8794.8** | **Shirley** | **GL (30)** |
| | **Tell3d3/2** | **1.957** | **5866.2** | **Shirley** | **GL (30)** |
| **TBZ1** | **Te3d5/2** | **1.791** | **106757.8** | **Shirley** | **GL (30)** |
| | **Te3d3/2** | **1.757** | **71207.5** | **Shirley** | **GL (30)** |
| | **Tell3d5/2** | **1.851** | **17061.4** | **Shirley** | **GL (30)** |
| | **Tell3d3/2** | **2.037** | **11380.0** | **Shirley** | **GL (30)** |
| **TBZ4** | **Te3d5/2** | **1.934** | **116497.8** | **Shirley** | **GL (30)** |
| | **Te3d3/2** | **1.897** | **77704.0** | **Shirley** | **GL (30)** |
| | **Tell3d5/2** | **1.11** | **4469.3** | **Shirley** | **GL (30)** |
| | **Tell3d3/2** | **1.11** | **2981.0** | **Shirley** | **GL (30)** |

**Figures 4.6 b & c** show high resolution spectra belonging to Zn2p, Bi4f orbitals in TBZ thin films at different deposition condition and TBZ bulk. Peaks centers associated to Bi4f$_{7/2}$, Bi4f $_{5/2}$, Zn2p$_{3/2}$, Zn2p $_{1/2}$ for TBZ bulk and thin films were close to the reported values for $Bi_2O_3$ [109, 111] and ZnO [112]. The relative

peak area ratio and spin-orbit coupling for $Bi4f_{7/2}$, $Bi4f_{5/2}$ photolines were 3:4 and 5.3 eV, while those for $Zn2p_{3/2}$, $Zn2p_{1/2}$ photolines were 1:2 and 23.1 eV in all samples investigated. Peaks of other oxides of bismuth and zinc were not observed and significant shift in core lines does not occur in the thin films grown in both oxygen-rich and deficient atmosphere. This indicates that the oxidation state $Bi^{3+}$ and $Zn^{2+}$ were maintained in the oxides in all deposition conditions.

**Figure 4.6d** shows high resolution spectra corresponding O1s orbital for bulk-TBZ, TBZ1 and TBZ4. The slight asymmetry in O1s spectra in all samples is indicative of contributions from two different oxygen sites; bridging oxygen (BO) and non-bridging oxygen (NBO). The peaks associated with BO contributions were found at (531-532 eV) while those from NBO is found at (529-530 eV) similar to reported values for $SiO_2$- and $TeO_2$-based glasses [113,114]. The ratio of BO to NBO was found to increase as the oxygen flow rate in agreement with Raman spectra shown in the next section.

**Figures 4.6 (e-f)** shows the peaks corresponding to the doublets $Te3d_{7/2}$ and $Te3d_{5/2}$ for the bulk target, TBZ1 and TBZ4 thin films. Peak positions observed at (575.79-576.4) ± 0.02 eV and (586.16-586.75) ± 0.02 eV respectively, correspond to those reported for amorphous $TeO_2$ [98, 115]. All patterns show a slight asymmetric line shape, suggesting the presence of mixed oxidation states of Te3d orbital.

Previous reports on tellurite glasses assert that glass modifiers in $TeO_2$-based glass deform the $TeO_4$ structural units into $TeO_3$ with lower coordination number [77, 84]. This deformation which easily occur along the axial-equatorial bonding of $TeO_4$, changes the $Te_{ax}$-$O_{eq}$-Te angle along the c-axis causing creation of defects, oxygen vacancies and increases non-bridging oxygen concentration, which is also confirmed

by our Raman measurements to be discussed in the next section [116]. Oxygen vacancies result in creation of cation-cation bonds such as Te-Te and low coordinated Te [117].

The Te-Te peaks at 573.73 eV [115, 118] found in the oxygen-deficient film indicate the presence of under-coordinated Te which contributes to high absorption in the entire UV-Visible spectrum as observed in **Figure 4.3b**. The area of the shoulder peaks decreases and the binding energy increases as the oxygen in the environment increases. This suggests that the low coordinated Te present in oxygen-deficient thin films oxidizes and becomes $TeO_2$ and sub-oxides in the presence of oxygen, which explains the optical transparency of the oxygen-rich films.

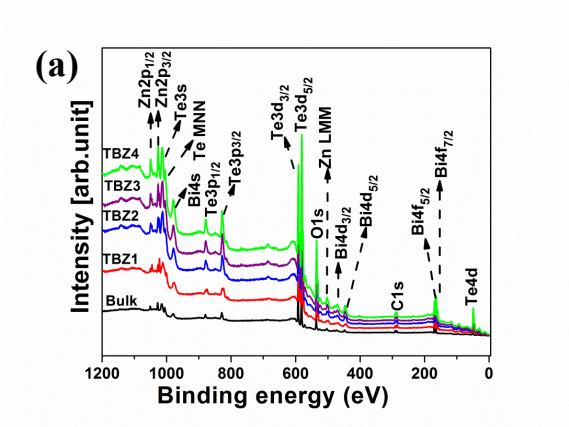


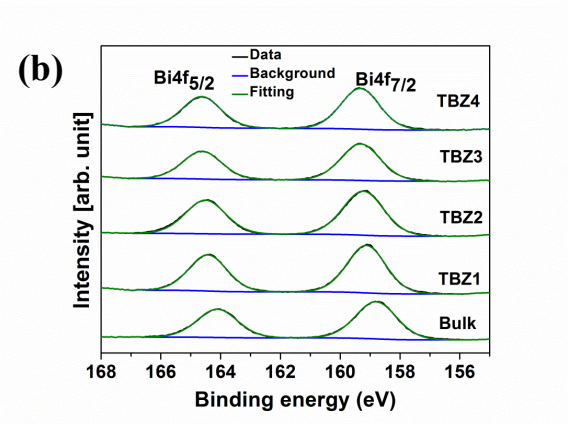


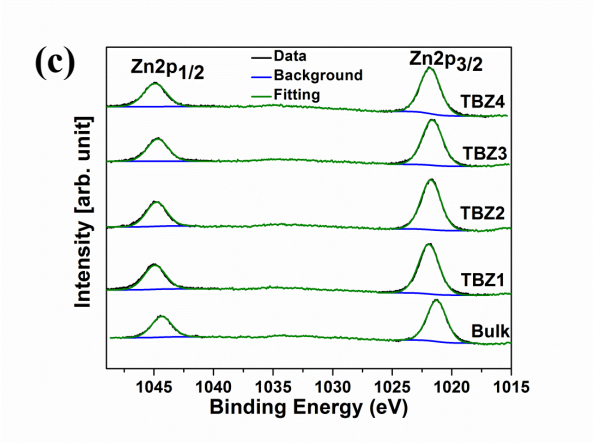


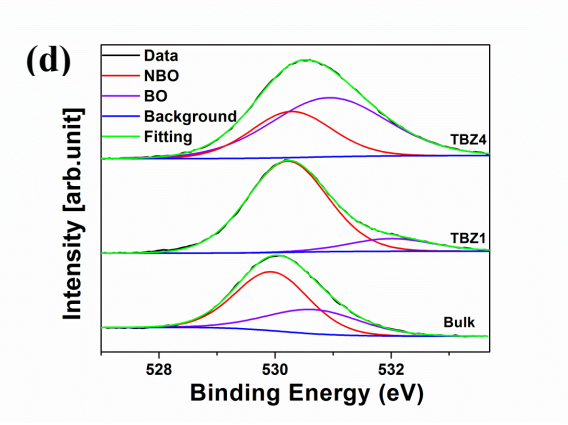

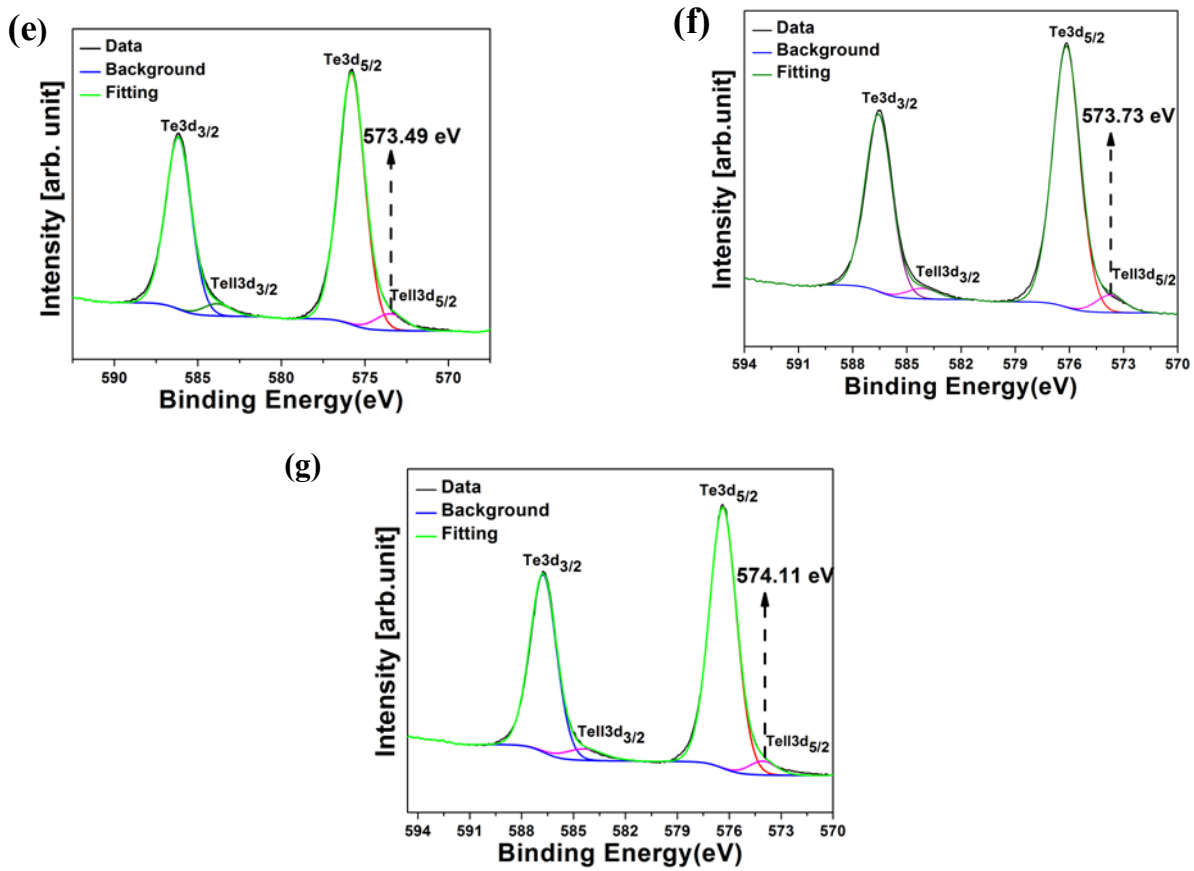


Figure 4.6*:* XPS spectra showing (a) survey scan of all samples showing only the peaks belonging Te, O, Zn, and Bi orbitals; (b) deconvoluted high resolution scan of Bi4f orbital (c) deconvoluted high resolution scan of Zn2p orbital (d) deconvoluted high resolution scan of O1s orbital. (e) deconvoluted high resolution scan of Te3d orbital for bulk (f) deconvoluted high resolution scan of Te3d orbital for TBZ1 (g) deconvoluted high resolution scan of Te3d orbital for TBZ4.

## 4.6 Impact of Stoichiometry on Thin Film Structure

To evaluate the structural evolution due to stoichiometry change, we resort to Raman spectroscopy to unravel the local cluster structures of tellurite glasses. Prior studies have shown that $TeO_2$-based glasses consist of asymmetric structural units such as $TeO_4$ trigonal bipyramid (tbp) and $TeO_3$ trigonal pyramid (tp) [100, 102].

Raman studies on single component $TeO_2$ assert that $TeO_4$ structural units bridging oxygen dominate $TeO_3$ units in overall $TeO_2$ structure [44, 119]. However, it is observed that in multicomponent tellurite glasses $TeO_3$ units with non-bridging oxygen prevail over $TeO_4$ units because addition of glass modifiers such as $Bi_2O_3$ and ZnO leads to progressive transformation of the $TeO_4$ structural units into $TeO_3$ units via the intermediate $TeO_{3+1}$ units [77]. The $TeO_{3+1}$ units are structurally similar to $TeO_4$ structural unit with on longer Te-O bond.

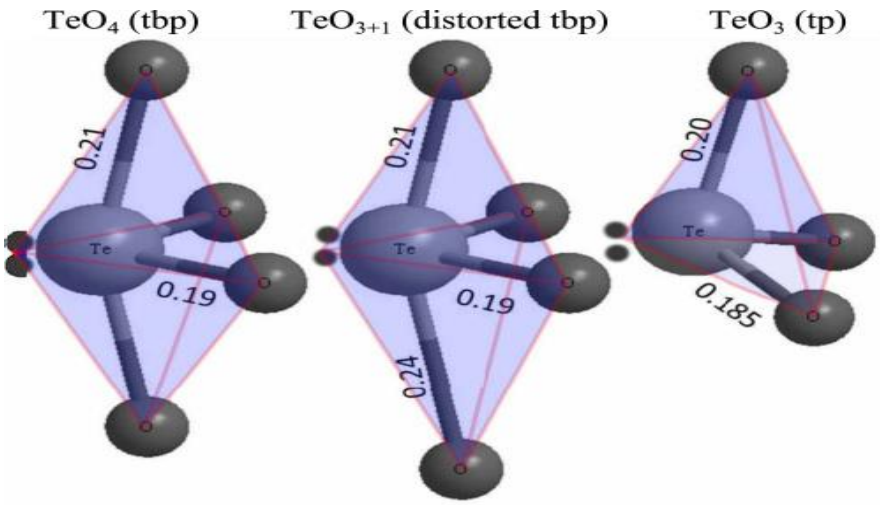


Figure 4.7: Ball and stick representation of the structural units present in tellurite glass. Left: Trigonal bipyramidal $TeO_4$. Center: Distorted trigonal bipyramidal $TeO_{3+1}$. Right: Trigonal pyramidal $TeO_3$. Dots represent nonbonding electrons. Bond lengths (in nm) are taken from [120]

To examine the influence of stoichiometric change in the structure of TBZ bulk and thin films, four Raman measurements recorded on different regions per sample were averaged and plotted in **Figure 4.8a.** The resulting spectra are deconvoluted using

Gaussian fitting as shown in **Figure 4.8b**. The positions of the Raman bands of these glasses and their assigned vibrational modes are listed in **Table 4.5**.

Three major features are observed from the measurements: TBZ-bulk target showed at 404 $cm^{-1}$, 652 $cm^{-1}$, 751 $cm^{-1}$ while argon sputtered thin film (TBZ1) displayed peaks, close to TBZ bulk target, around 392 $cm^{-1}$, 668 $cm^{-1}$, 750 $cm^{-1}$. Similarly, Raman peaks appeared in $Ar/O_2$ sputtered thin films around 463 $cm^{-1}$, 657$cm^{-1}$, 769 $cm^{-1}$. The vibrational modes observed in our study can be associated with the following structural elements: **(a)** bands around 392 $cm^{-1}$- 404 $cm^{-1}$ are assigned to the bending mode of Te-O-Te linkages of predominant $TeO_3$ (tp) networks in TBZ-bulk target and TBZ1 while peaks located around 463 $cm^{-1}$ belong to bending mode of Te-O-Te linkages of predominant $TeO_4$ (tbp) network in $Ar/O_2$ sputtered TBZ2-TBZ4 thin films [44, 121]; **(b)** bands near 655-668 $cm^{-1}$ belong to the vibration of the Te-O bonds in $TeO_4$ (tbp) with bridging oxygen (BO) or Te-O-Te linkages constructed by two unequal Te-O bonds[77,78,98]; **(c)** the band near 750-772 $cm^{-1}$ originate from at least two main contributions assigned to stretching of Te-O or Te=O which contain non-bridging oxygen(NBO) in $TeO_{3+1}$ or $TeO_3$ units[77, 78, 44, 122]. The peak at 576 $cm^{-1}$ originates from the sodalime silicate glass substrate. As shown in **Figure 4.8a**, $TeO_3$ or $TeO_{3+1}$ units with NBO are the predominant structural units in the bulk target and TBZ1 evident from their Raman peak intensity compared to those for $TeO_4$ units. The result is consistent with previous reports on bulk TBZ characterizations [77,78]. Apparently, as oxygen is introduced in the working gas, the stoichiometry of the thin films changes leading a different structural configuration with high concentration of

BO. Consequently, the magnitude of peak intensity of band around 656-668 $cm^{-1}$, assigned to $TeO_4$ with bridging oxygen, increases as the oxygen flow rate leading to a shift in phonon mode of Te-O-Te linkages toward higher vibration frequency as seen in TBZ2-TBZ4. The structural evolution from bulk/TBZ1 to oxygen-rich thin films can be explained as formation of more $TeO_4$ structural units from $TeO_3$ units which indicate a change in coordination number of Te atoms from 3 to 4([$TeO_3$] tp) to ([$TeO_4$] tbp). Oxygen doping of TBZ-bulk target, leads to the formation of Te-O bonds with large bond energy and force constant which is responsible for the Raman red shift [106].

Specifically, vibrational analysis has confirmed existence of transformations of the tellurite entities $TeO_3 \rightarrow TeO_{3+1} \rightarrow TeO_4$ as function of the percentage of $O_2$ ions present during deposition of the tellurite glass matrix.

Table 4.5: Raman Peak Positions and Assignments

| **Raman Band ($cm^{-1}$)** | **Assignment** |
|---|---|
| **392-404** | Bending mode of Te-O-Te linkage in $TeO_3$ network backbone in oxygen-deficient samples. |
| **463 - 465** | Bending mode of Te-O-Te linkages in $TeO_4$ network backbone oxygen-rich samples. |
| **576** | Contribution from the sodalime substrate. |
| **656 – 657** | Vibration of the Te-O bonds in $TeO_4$ trigonal bipyramid with bridging oxygen. |
| **750 - 772** | Stretching mode of Te-O or Te=O which contain non-bridging oxygen (NBO) in $TeO_{3+1}$ or $TeO_3$. |

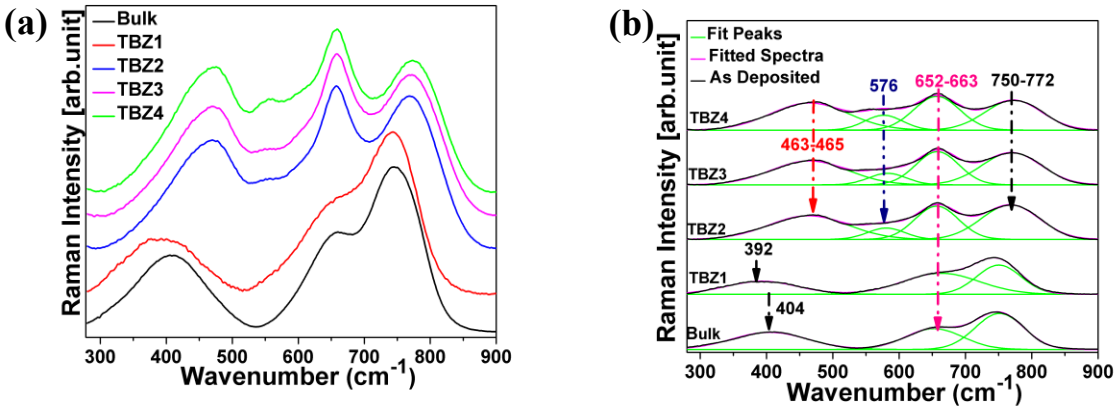


Figure 4.8: (a) Raman spectra of tellurite thin films sputtered in varying argon and oxygen working gas; (b) Raman spectra decomposition into the respective vibrational modes. The corresponding peak assignments are listed in Table 4.

## 4.7 $TeO_2$-based Materials Potential Applications

In this report, we deposited planar $TeO_2$ -based thin films using RF magnetron reactive sputtering. The effects of variation of oxygen flow rate in the working gas ($Ar/O_2$) on the structural, chemical state and optical properties of sputtered thin film were thoroughly investigated using suitable characterization techniques. Thin films sputtered in $Ar/O_2$ atmosphere (oxygen-rich) are amorphous and possess large fractions of $TeO_4$ vibrational bonds and are structurally dissimilar to thin films deposited in pure argon atmosphere (oxygen-deficient) which contains large fractions of non-bridging oxygen. Increasing the oxygen flow rate improves the optical transparency in the multicomponent tellurite thin film in the entire visible and near infra-red region. We suggested that unoxidized Te element in oxygen-deficient thin films is responsible for the broad optical absorption.

The materials characterization results, as carefully explained in the previous sections of this chapter, point that materials properties of $TeO_2$-based thin films such as improved optical transparency, low surface roughness, high refractive index (n ~ 2) and amorphous structure makes $TeO_2$-based glass thin film a suitable candidate to initiate the pathway for potential application in integrated photonics. Furthermore, these attractive properties meet the target material requirements suggesting that tellurites are ideal for frontside LSG structures for thin film solar cell applications.

# Chapter 5

# AGAROSE HYDROGEL MEDIATED WET STAMPING METHOD

## 5.1 Motivation

Due to increasing demand for low cost integrated system with miniaturized components, there has been drive to develop single step techniques to meet this demand. Several micro and nano-scale devices depend on curvilinear and multi-step topographies. Fabrication of such devices from micro and nanoimprint techniques using dry transfer printing materials (polymer, elastomer) and solution based (wet) transfer printing have been deeply explored and established [123,124]. Dry transfer printing of micro and nanoscale patterns using these materials suffers several drawbacks such as mechanical wear, swelling in organic solvent to gas permeability that limits their potentials in broad applications. While solution based transfer printing (convectional wet etching) requires multi-step fabrication of the devices causing poor reproducibility. Moreover, micro-patterning of hard and durable materials involves complicated and expensive procedures such as reactive ion etching [125], laser ablation [126], focused ion beam [42] which are serial and requires that each device has to be fabricated anew.

In this chapter, we developed a simple maskless, single-step and low cost method to pattern micro-scale planar photonic components using agarose hydrogel mediated wet etching. This method overcomes these limitations by using an agarose hydrogel stamp to mediate a conformal etching process at low thermal budget (room

temperature). In our maskless method, agarose hydrogel stamps are patterned following a standard soft lithography and replica molding process from micro-patterned photoresist masters and soaked in a chemical etchant. The micro-scale features on the stamp are subsequently transferred into glass and polymer thin films via conformal wet etching.

## 5.2 Introduction to Agarose Hydrogel

Hydrogels are three-dimensional (3D) polymer materials swollen by a large amount of water while maintaining their dimensional stability. Hydrogel natural forming polymers include proteins such as collagen and polysaccharides such starch and agarose. Hydrogel has unique structure that gives it several advantage characteristics of both the solid and liquid states. Hydrogels are hydrophilic, water insoluble, highly absorbent natural or synthetic polymers. Their high water/buffer holding capacity and good mechanical stability when loaded with low water/buffer content qualify them as good candidate for imprinting stamp for both soft and solid substrates. Hydrogels were utilized as stamps to transfer soft materials such as proteins and antibodies onto solids substrates without noticeable loss of activity [127].

Agarose hydrogel is a hydrophilic material used as stamps material [32, 128, 129]. Agarose is the major component of commercial agar, a polysaccharide extracted from marine red algae. It is a linear polysaccharide with a main chain consisting of 1, 3-linked D-galactose and 1, 4-linked 3, 6-anhydro-R-L-galactose [130] shown in **Figure 5.1**. Agarose is slightly negatively charged with sulfate groups and has a double helical network that is stabilized by water molecules. Agarose hydrogels are prepared by dissolving agar powder in vigorously boiling water until the powder particles dissolves completely leaving a clear hot solution.

Agarose undergoes a thermos-reversible gel in aqueous solution with a setting temperature is usually close to 40 $^{o}$C, while the melting temperature is considerably higher (around 90 $^{o}$C). Note that here both "setting" and "melting" represent simple observational concepts and are not rigorously identifiable with the normal scientific meanings of these terms. Thus it exhibits a significant range of thermal stability.

Agarose hydrogels consist of thick bundles of agarose chains linked by hydrogen bonds with a large amount of nanopores [131]. Agarose molecules are able to form gels with relatively defines pore sizes due to its chemical properties. The pore-size distribution ranges from 1 to 900 nm depending on the agarose concentration [132]. As the agarose concentration increases, the average diameter of the pore decreases. The porous structural network of agarose hydrogel gives it a unique property of holding solutions therefore acts at a solution reservoir.

Agarose gel is a suitable candidate for wet stamping because it's mechanical and chemical ruggedness, and relatively high degree of elasticity. Agarose gel enjoys certain degree of stability in many organic and inorganic solutions. Agarose tolerates weaker acids relatively well and can survive for several hours in harsh chemical such as dilute hydrofluoric acid (HF). As a results of it attractive properties, agarose hydrogel has been employed extensively in, engineering and microfabrication, as a stamp material to fabricate micro scale architecture in solid substrates such glass, silicon, GaAs, etc for semiconductor applications [32, 33].

In our study, we implemented a low cost, bench top and unconventional wet etching process to pattern optical device on sputtered oxide glass thin film using agarose hydrogel stamp. The monolithic fabrication technique eliminates the serial/multi-step patterning of $TeO_2$-based glass films via reactive ion etching, focused

ion beam. In our process, hydrogel stamps are replicated, via soft lithography, from micropatterned masters, soaked in an optimized chemical etchant and then used to etch large area microstructure on the desired substrate with excellent surface smoothness and good retention of stamps quality.

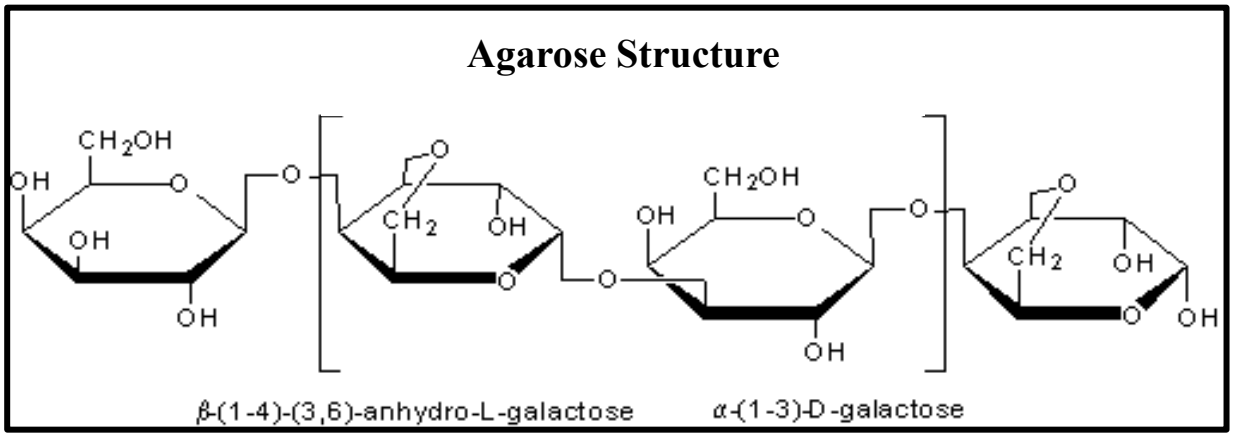


Figure 5.1: Chemical structure of Agarose.

### 5.3 Fabrication Process Flow

Fabrication of micro/nano-structure material surfaces; modification of their microscale topographies, is vital in modern technology including microfluidics, optoelectronics, and water-repellent surfaces. Numerous existing microstructure techniques such as x-ray lithography [133], micromachining [134], laser etching [135], reactive ion etching (RIE) [136], are either serial in nature and/or expensive. In addition, they rely on protective coatings which often delaminate or become under etched. In compliance to the low cost methods to achieve $1/W DOE goal, one would prefer a technique which is both accurate and inexpensive and could be a bench-top for rapid prototyping small scale structure in various materials.

In this study, we utilized a modified process of the reaction-diffusion wet stamping (RD-WETS) method proposed by Grzybowski group [32, 33] to demonstrate patterning of optical devices on $TeO_2$-$Bi_2O_3$-ZnO and other oxide glasses. This proposed method, RD-WETS, initiated by easy-to-use hydrogel stamps, meets the criteria and can imprint binary, multi-layer or curvilinear architecture and devices on glass, metal, semiconductors, crystals and others materials with a resolution of about 300 nm.

RD wet stamping (RD-WETS) method begins by fabricating a hydrogel stamp, which is cast, like in soft lithography [137] against a desired micro-/nano patterned master. Typically, a hot, degassed 8–12% w/w solution of high-strength agarose in deionized water is cast against an SU8 or silicon master presenting an array of micro- or nano features on its surface. After further degassing under vacuum and gelation, the agarose stamp is gently peeled off patterned with the negative of the array of features in the master then soaked in a desired etchant. This master can be reused several times. An agarose stamp soaked with an appropriate chemical reactant can etch/dissolve the desired hard material by simply contacting with the substrate. The Agarose stamp serves a two way "pump"; it continuously supplies the etchant to dissolve the substrate while removing the etchant products into the stamp's bulk.

Following this method, $TeO_2$-$Bi_2O_3$-ZnO glass thin film, that will be in conformal contact with agarose stamp, is deposited using reactive RF sputtering in an oxygen environment which offers the advantage of eliminating oxygen deficiency defects in the multicomponent glass[138]. **Figure.5.2** schematically illustrates the process flow of the device fabrication via wet stamping explored in this study. We

successfully fabricated waveguides on tellurites, AZ resist and rare earth doped tellurites using wet stamping.

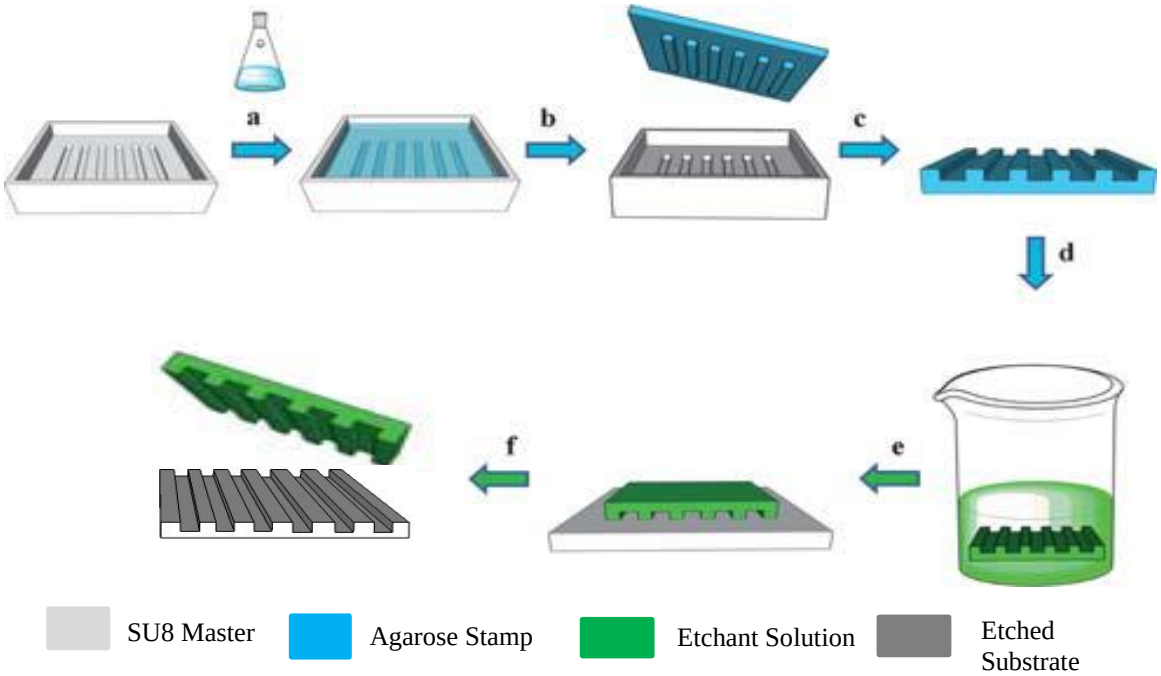


Figure 5.2: Key steps in wet stamping (a) Agarose hydrogel is prepared and poured on a photo-lithographically structured master (PDMS), (b) the hydrogel stamp is cured and peeled off the master, (c) the stamp is cut in smaller pieces, (d) the high porous stamp is soaked into etchant solution, (e) the stamp containing etchant solution is removed and placed in contact with a suitable surface, (f) a patterned substrate is obtained.

### 5.3.1 Master Mold Fabrication

Micropatterned master for wet stamping were prepared using photo-lithography method on SU8 photoresist. SU8 resist is a chemically amplified photoresist and the main components are SU8 monomers, organic solvent and a photo-acid generator (PAG). The available film thicknesses depend on the amount of solvent in the resist before spin coating [139].

The Si-substrate for SU8 photoresist master is properly clean with Piranha solution for 5 mins to remove any organic contaminants then dipped in hydrofluoric acid (HF) solution for 1min to strip oxide layer on the substrate. This process creates improved photoresist adhesion on the Si substrate.

The sample for photo-lithography is prepared by spin coating SU8 photoresist (negative photoresist) on the Si-substrate at 2500 rpm for 35 secs using a spin coater then prebaked (soft bake) for 4 mins at 95 $^{o}$C. Prior to photoresist spin coating, the Si-substrate was preheated to remove any possible moisture on its surface. Microscale patterns were transferred to the photoresist by contact photolithography process. The samples were keep in contact with a chrome mask; with the desired patterns, then exposed to UV rays for 12 secs using MJB3 Mask Aligner. UV rays reacts with carbon chains of the photoresist polymer and intiates a cross-linking process. The area exposed to UV-rays selectively crosslinks while the unexposed region of the SU8 photoresist does not undergo this process thus washes away during process development stage. After exposure the samples were post baked for 4 mins at 95 $^{o}$C. The post exposure bake (PEB) catalytically performs and completes the photo reaction initiated during exposure and also to reduce mechanical stress formed during soft bake and exposure of especially thick resist films.

The sample was developed using SU8 developer for 2 mins 30 secs, rinsed in Isopropyl alcohol (IPA) and dried using nitrogen gun. This repeatable and optimized photolithography process was followed to fabricate devices for target application:
(a) 2 µm thick SU8 masters with 50 µm linewidth bending waveguides to develop a robost and repeatable wet stamping recipe and demonstrate the suitability of wet stamping in patterning complex geometries.

(b) 5 µm thick SU8 masters of dimensions 5-30 µm (width) and 2 cm (long) waveguides for measuring the optical transmisson in sputtered tellurite thin and These SU8 master were characterized using scanning electron micrscope to measure photoresist thickness and pattern quality as shown in **Figure 5.3**.

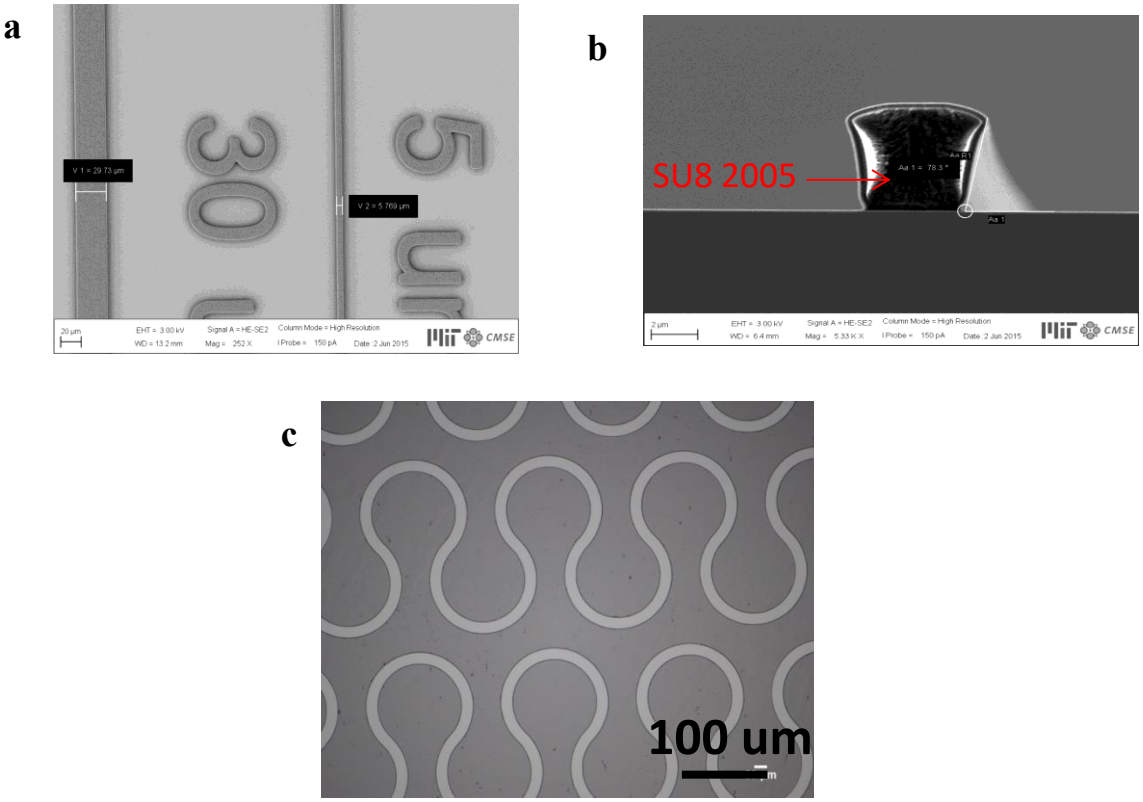


Figure 5.3: SEM images: (a) top and (b) cross-section view of SU8 master mold; (c) Optical microscope image of 50 µm bending waveguides.

### 5.3.2 Agarose Stamp Fabrication

In this study, agarose hydrogel stamps were prepared by dissolving and heating 8-10 w/v % agarose solution of high gel agarose (EMD Millipore Corporation, IL USA) in a microwave oven for 48 secs. The master was heated to 100 $^{o}$C for 10 secs

to allow it warm up and minimize formation of air bubble at it surface. The hot agarose solution is quickly degassed in oven furnace at 110 $^{o}$C (above agarose hydrogel melting) and quickly cast (to a height of 2 cm) onto the micropatterned masters with desired surface topography made from soft materials (SU8 epoxy). The advantages of casting agarose solutions with a thickness of 2 cm are (i) the extended time of gelation for removal of trapped air bubbles from the wells of the master (by repeatedly pulling and releasing a vacuum) and (ii) easy handling during stamping. Finally, we allowed the agarose solution to gel and solidify at room temperature and ambient pressure. The solidified agarose hydrogel stamp is peeled off the master (the master can be cleaned and reused several times) and cut into rectangular stamps which will be soaked in an etchant solution for several hours to allow the etchant solution diffuse into stamps nano-pores. Agarose hydrogel stamp excellently released from the SU8 mold without any residue as shown in **Figure 5.4 a & b**. The stamps are dried on filter paper place for 10 mins and blown dry with nitrogen for 10 s. The stamps can be stored, after wet stamping, for several months in deionized water and reused multiple times.

**a**

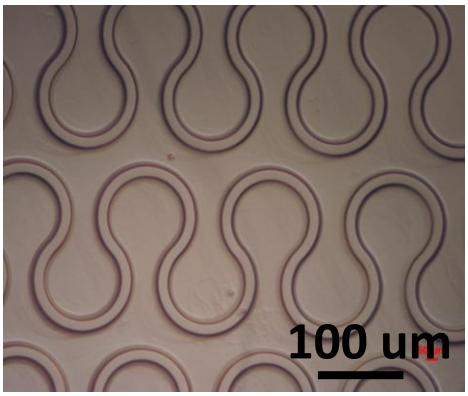


**b**

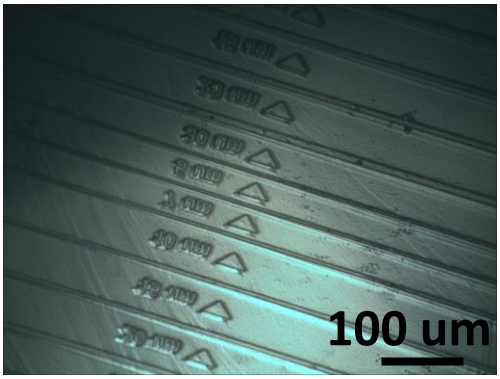

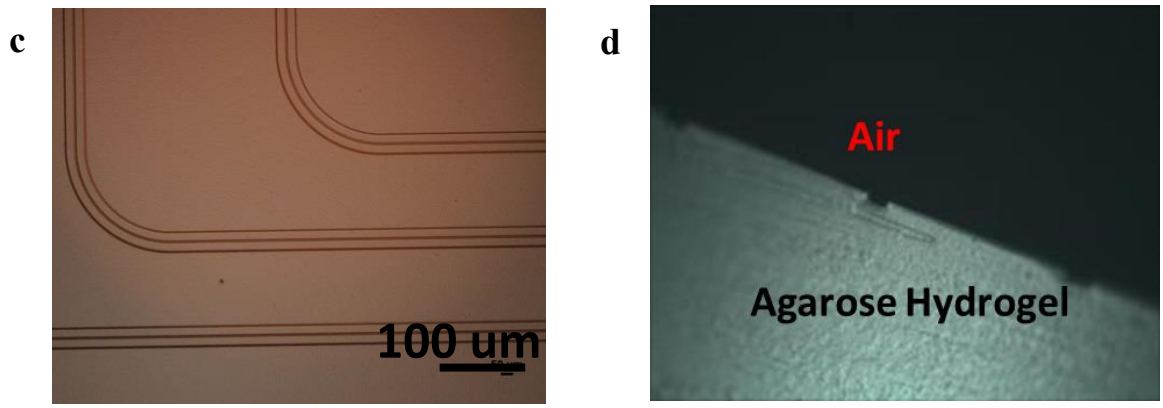


Figure 5.4: Optical image of Agarose hydrogel replica with micropatterned after release from SU8 master.

### 5.4 Wet Stamping of Sputtered Tellurite glass thin films

Multimode waveguides were fabricated on sputtered $TeO_2$-$Bi_2O_3$-ZnO (TBZ) thin films (detailed deposition steps as described in [140]) by bringing the patterned side of agarose hydrogel stamp in contact with the thin film surface and ensure good conformal contact between the stamp-thin film surfaces. Prior to waveguide fabrication on the sputtered thin film, the agarose hydrogel stamps were soaked in an appropriate and optimized etchant solution; an aqueous solution of hydrofluoric acid (ratio of 1 HF: 40 DI $H_2O$), for 4-5 hours to allow the solution penetrate into the stamps nanopores. The stamps were kept feature side up while in etchant solution to prevent pattern deformation. The etchant solution used for wet stamping of tellurite glass was optimized by varying the acid concentration in solution to preserve the integrity and mechanical properties of the stamp. Higher concentration of acid solution speeds the etching but deteriorates the structural quality of the stamp while dilute acid solution simultaneous preserves stamps integrity and provides a more controlled etching process.

The stamps were removed for the acid solution, after soaking, and dried then applied with the micropatterned side in contact with the thin film surface. A 50 g weight was placed on the stamp-thin film system to create conformal contact without deforming the 3D micro structures. Once in conformal contact, the etchant solution slowly diffuses from the hydrogel stamp into the thin film and initiates a chemical reaction on the areas in contact with the stamp. The stamp bulk acts as a two way chemical "pump" simultaneously supplying fresh HF etchant onto the gel-thin film interface while removing reaction products along a concentration gradient as shown in **Figure 5.5a**. This selectively imprints the opposite of the micro features on agarose hydrogel stamp on the thin film at an average etch rate of 20 nm/min. The etchant solution wets the thin film causing lateral spreading of the etchant to other areas of contact between the stamp's micro structures and the thin film. Lateral spreading could be prevented by adding surfactants in the etchant solution and performing the wet stamping in a beaker with paraffin oil. However, this step prevents lateral spreading but affects the device performance. A suitable alternative such as optimizing the etchant solution to reduce the etch time was employed in order to eliminate the use of paraffin oil in the process to preserve the device quality.

We successfully fabricated complex waveguide structure of various linewidths (1 – 50 µm) and tested the device performance to validate the optical performance of unconventional agarose hydrogel mediated wet etched micro structures.

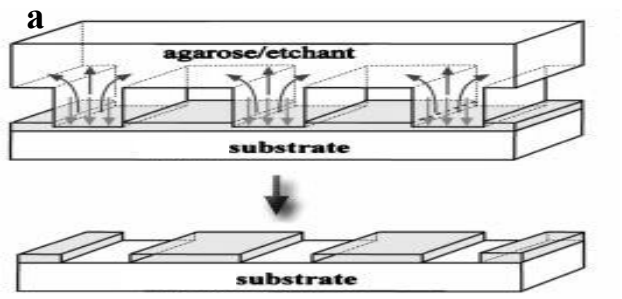

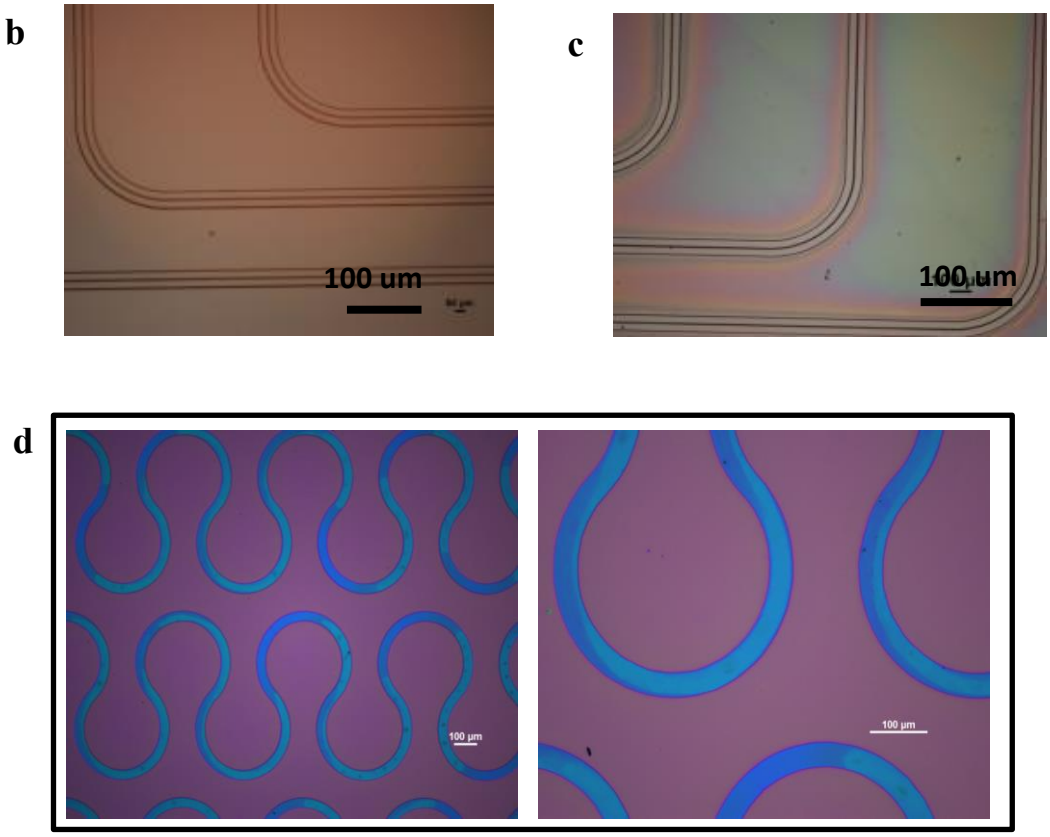


Figure 5.5: (a) Schematics of the experimental flow of wet stamping the arrows indicate two-way pumping mechanism in wet stamping Optical Images of (b) bending waveguides pattern on 12-13 % w/v Agarose gel; (c) Agarose etched bending waveguides (linewidth 1um) on sputtered TBZ glass using dilute HF; (d) Agarose etched bending waveguides (linewidth 50 µm) on sputtered TBZ glass using dilute HF indicating the ability of wet stamping to pattern complex geometries.

### 5.4.1 Optical Loss Measurement of Tellurite Waveguides

Multimode waveguides were fabricated on multicomponent oxide glass thin film (TBZ) deposited on 3 um thick $SiO_2$ cladding layer on silicon substrate (as shown in **Figure 5.6 a**). The thick oxide layer provides enough isolation to prevent leakage of

TBZ optical modes into silicon substrate. Prior to wet stamping device fabrication, we simulated a design of the rib waveguide structure to determine the parameters that produce maximum mode confinement in the core layer (TBZ layer). Our simulation result indicates that these parameters: TBZ4 Rib-WG on 3μm $SiO_2$. TBZ thickness: 700 nm, target width: 5 μm; Rib thickness: 350 nm; Slab thickness: 350 nm were suitable for maximum light confinement. **Figure 5.6 f** shows a simulated TBZ rib waveguide on 3 μm $SiO_2$ cladding.

The optical transmission spectrum was characterized on a Newport Auto Align workstation and an optical vector analyzer (LUNA Technologies OVA-5000) with a built-in tunable laser. Near-infrared wavelength light was coupled in and out through the bus waveguide using a tapered lens-tip fiber. The fabricated tellurite waveguide has dimensions of 1 cm (chip length), 700 nm (height) and 5-10 μm (width). Optical loss in the waveguides is measured using a fiber end-fire coupling method and the cut-back technique, as shown in **Figure 5.6e,** is 2 dB/cm at 1550 nm wavelength**.**

**a**

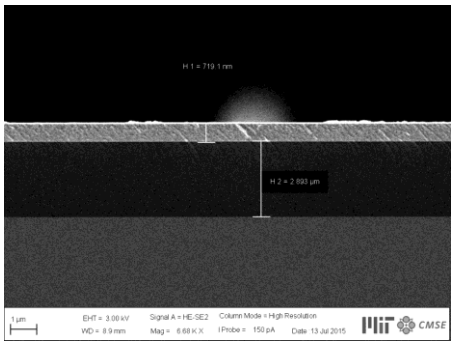


**b**

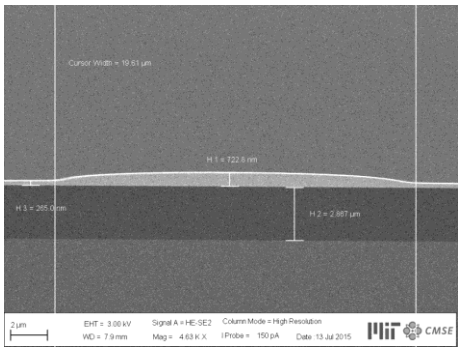

c

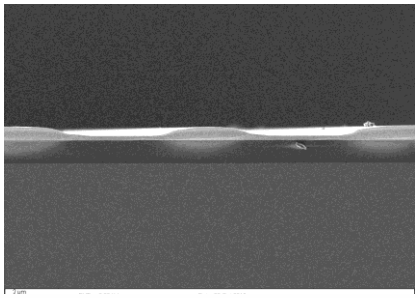

d

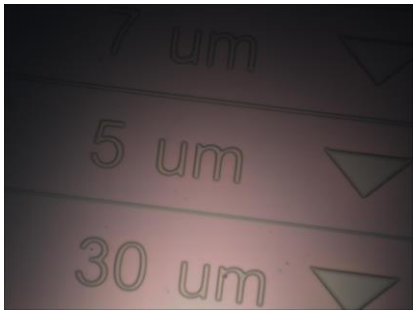
7 um
5 um
30 um

e

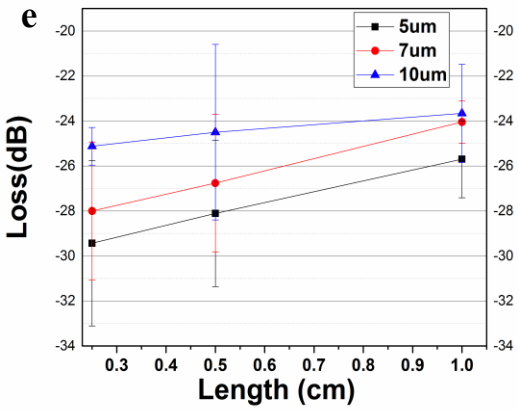
5um
7um
10um
Loss(dB)
Length (cm)
-20
-22
-24
-26
-28
-30
-32
-34
0.3
0.4
0.5
0.6
0.7
0.8
0.9
1.0

f

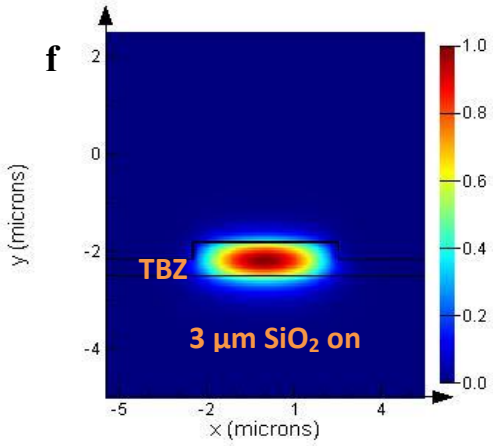
TBZ
3 µm SiO2 on
y (microns)
x (microns)
2
0
-2
-4
-5
-2
1
4
1.0
0.8
0.6
0.4
0.2
0.0

g

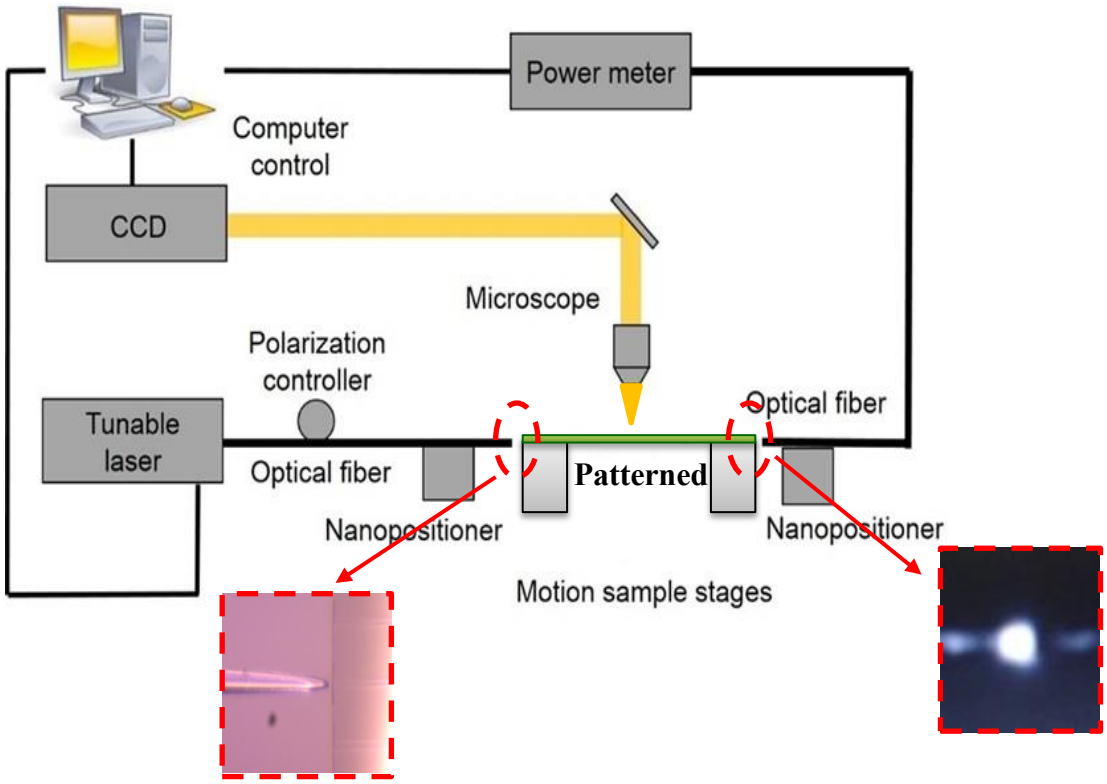
Power meter
Computer control
CCD
Microscope
Polarization controller
Tunable laser
Optical fiber
Optical fiber
Patterned
Nanopositioner
Nanopositioner
Motion sample stages

Figure 5.6 : SEM images of (a) as-deposited TBZ thin film on 3 µm $SiO_2$ cladding; (b & c) micro patterned TBZ rib waveguide via wet stamping process; (d) Optical image of agarose etched micro patterned TBZ rib waveguide (e) Optical transmission measurement to determine material loss at 1550 nm wavelength; (f) Simulation TBZ rib waveguide result; (g) Optical measurement set up.

## 5.5 Wet Stamping of Erbium Doped Tellurites

Oxide glasses such as tellurites are gaining surging popularity as a possible materials for rare-earth doped optical fibers [37].Erbium doped Tellurite (Er-$TeO_2$) thin films are especially promising for integrated photonics because of their transparency form visible to mid-infrared spectral region, high solubility of erbium in $TeO_2$, low phonon energy, and high refractive index [82]

Irrespective of its attractive properties, fabrication of tellurites based glass thin film has been difficult, due to chemical inertness and mechanical hardness, which this limits its application in photonic components. There are several reports of planar waveguides in tellurite based thin films fabricated using reactive ion etching [141], UV direct writing [142], focused ion beam [138], sputter etching [61]. Although all these methods recorded success in fabricating waveguide, they are multi-steps and each device is fabricated afresh. Using a monolithic step, bench top and less expensive agarose mediated wet etching method; we have successfully fabricated micro-scale waveguide in Er-doped $TeO_2$.

In this section we present the process steps for characterization and waveguide fabrication on RF co-sputtered Er-$TeO_2$ thin film to validate the suitability of using a single step wet stamping method "difficult to etch" materials for photonics applications.

### 5.5.1 Erbium-Tellurite Thin Film Deposition and Characterization

Sputtering targets of Erbium(Er) and $TeO_2$ [2 inches, 0.25 inches thickness] purchased from AJA international were used for thin film deposition. Thin films were deposited from the target onto substrates (sodalime silicate glass slides from Fisher Scientific Inc. or 3-inches (100) silicon wafers from SiliconQuest Inc.) by RF reactive co-sputtering. Prior to deposition, the glass substrates were cleaned with $H_2SO_4$-Nochromix® solution while silicon substrates were dipped into buffered oxide etch (BOE) solution for 3 minutes to remove the native oxide layer. The sputter deposition chamber was first evacuated to a base pressure below $10^{-5}$ Torr. The target-substrate spacing is fixed at 13 cm for all deposition. The target Pre-sputtering was conducted for 10 minutes prior to film deposition, with covered substrates, to clean the surface of the target of any possible contamination. Co-Sputtering was performed, using a custom-designed system (AJA sputtering systems), in oxygen ($O_2$) and argon (Ar) atmosphere at growth rate of 14 nm/min and deposition pressure 2.4 mTorr. The flow rate for Ar was 10 sccm and for $O_2$ was 2 sccm. The sputtering power for deposition was 80 W for Er target and 60 W for $TeO_2$ target. During deposition, the substrates were rotated at 5 rpm to ensure uniform thin film deposition. For each deposition, the films are deposited on both soda-lime and Si substrates simultaneously. The substrates were not intentionally heated and were kept near room temperature throughout the deposition process. The Er-doped $TeO_2$ thin film morphology and deposition rate were calibrated using a Dektak profilometer and scanning electron microscope (SEM). The chemical composition of as-deposited Er-$TeO_2$ thin film was characterized using energy dispersive X-ray (EDX) spectroscopy as shown in **Table 5.1.**

### 5.5.2 Morphological and Chemical Characterization of Erbium-Tellurite Thin Film

The surface and cross sectional morphology of the resulting tellurite films were examined using scanning electron microscope (SEM) system(Zeiss Merlin, CMSE MIT) operating with an accelerating voltage of 3kV. The samples were covered with a thin (~ 40 nm) gold (Au) coating prior to SEM imaging to minimize charging from electron accumulation on the sample surface. **Figure 5.7 a**. shows SEM cross-section image of Er-$TeO_2$ thin films deposited on silicon (Si) substrate in constant oxygen and argon flow rates. The as-deposited Er-$TeO_2$ thin films has 650 nm thickness confirming Dektak profilometer measurement. It can be seen that the thin film has a uniform and dense micro-structure.

Chemical Compositions of the TBZ films as measured using EDX are tabulated in **Table 5.1**. Three points were analyzed per sample in measuring the k-ratios of the samples. The results from EDX measurements indicate that the atomic percentage of $Er_2O_3$ in $TeO_2$ thin film is 1.4 %.

**a**

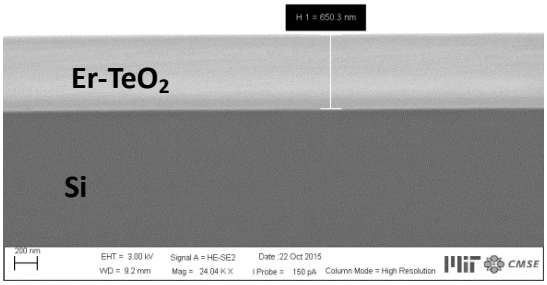


Figure 5.7: SEM image of as-deposited Er-$TeO_2$ on Silicon substrate.

Table 5.1: EDX composition analysis of Co- sputtered Er-$TeO_2$

| Element | Weight % | Atomic % | Error % |
|---|---|---|---|
| **O K** | **19.43** | **66.34** | **4.44** |
| **ErM** | **3.27** | **1.07** | **13.52** |
| **AuM** | **3.28** | **0.97** | **19.09** |
| **TeL** | **74.02** | **31.68** | **5.86** |

### 5.5.3 Wet Stamping of Sputtered Er-$TeO_2$ Thin Films

Multimode waveguides were fabricated on sputtered Er-doped $TeO_2$ thin films by bringing the patterned side of agarose hydrogel stamp in contact with the thin film surface and ensure good conformal contact between the stamp-thin film interfaces. Before making contact with Er-$TeO_2$ surface, agarose hydrogel stamps were soaked in an appropriate and optimized etchant solution; an aqueous acid solution (ratio of 1 HF: 3 HCl: 2 IPA: 500 DI $H_2O$), for 4-5 hours to allow the solution penetrate into the stamps nanopores. Addition of isopropyl alcohol in the etchant solution improves smoothness of the etched surface after etching. The stamps were kept feature side up while in etchant solution to prevent pattern deformation. The etchant solution used for wet stamping of Er-$TeO_2$ glass thin film was optimized by varying the acid concentration in solution to preserve the integrity and mechanical properties of the stamp. The stamps were removed for the etchant solution, after soaking, and dried then applied with the micropatterned side in contact with the thin film surface. Once in

conformal contact, the etchant solution slowly diffuses from the hydrogel stamp into the thin film and initiates a chemical reaction on the areas in contact with the stamp.

Using agarose mediated wet stamping, we have successfully developed a single step, bench top and low cost method of patterning Er-$TeO_2$ glass thin film that provides a simpler alternative to other multi-step processes.

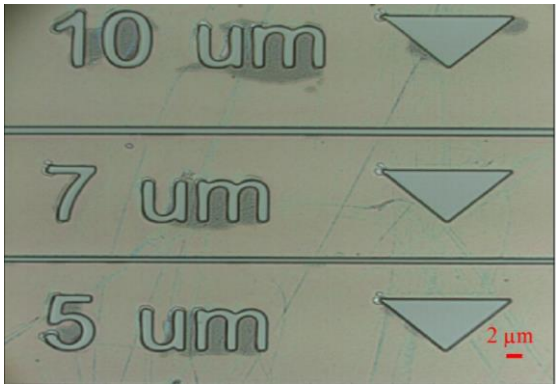


Figure 5.8: Optical Image of Agarose etched waveguides on sputtered Er-$TeO_2$ using HCl + HF+ IPA solution.

Following this technique, we fabricated waveguides on Er-$TeO_2$ thin films on 3 µm $SiO_2$ bottom cladding. The thick oxide layer provides enough isolation to prevent leakage of optical modes into silicon substrate.

The optical transmission spectrum was characterized on a Newport Auto Align workstation and an optical vector analyzer (LUNA Technologies OVA-5000) with a built-in tunable laser (shown in **Figure 5.6**). Near-infrared wavelength light (1525-1610 nm) was coupled in and out through the waveguide using a tapered lens-tip fiber. The fabricated Er-$TeO_2$ waveguide has dimensions of 0.6 cm (device length), 650 nm (height) and 5µm (width). Optical loss in the waveguides is measured using a fiber

end-fire coupling method. To demonstrate a proof concept of fabricating waveguides on Er-doped $TeO_2$ thin films (with 1.4 % $Er^{3+}$ composition according to EDX result in **Table 5.1**) using this technique, we show in **Figure 5.9** an Er-$TeO_2$ loss spectrum with an Erbium absorption trend that indicate high loss around 1540 nm and lower loss around 1600 nm. The observed loss trend is similar to that reported in [143] for reactive ion etching Er-$TeO_2$ fabricated waveguides.

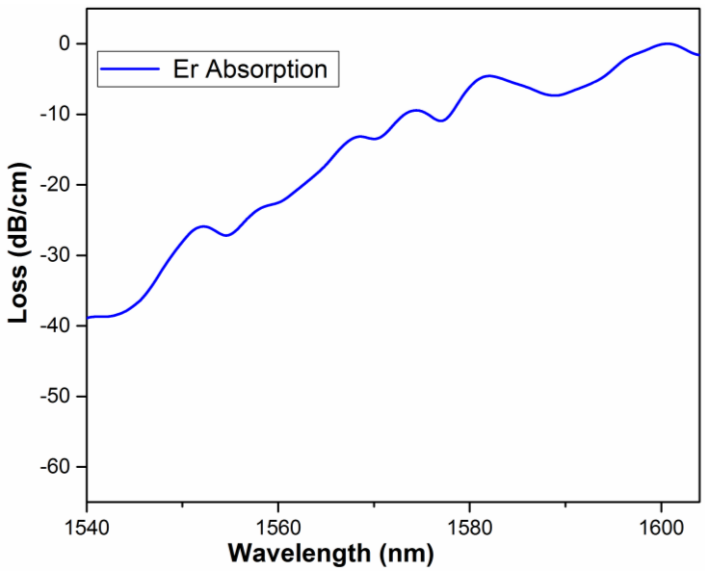


Figure 5.9: Loss Spectrum for 5 µm waveguide showing the high erbium absorption dip at 1540 nm.

## 5.6 Suitability of Wet Stamping Methods

Here we demonstrate the versatility of unconventional agarose mediated wet stamping in patterning polymers (AZ resist) and doped oxide ($GeO_2$-$SiO_2$) glasses. To these materials, 9 % w/v agarose hydrogel stamps were soaked in an appropriate and optimized etchant solution for 4-5 hours to allow the solution penetrate into the stamps nanopores. The optimized etchant for AZ resist, was propylene glycol methyl ether

acetate (PGMEA) solution (ratio of 1 PGMEA: 5 DI $H_2O$), while an aqueous hydrofluoric acid solution (ratio of 1 HF: 40 DI $H_2O$) was used for $GeO_2$-$SiO_2$. We successfully patterned waveguides of various linewidth as shown in the **Figure 5.10**.

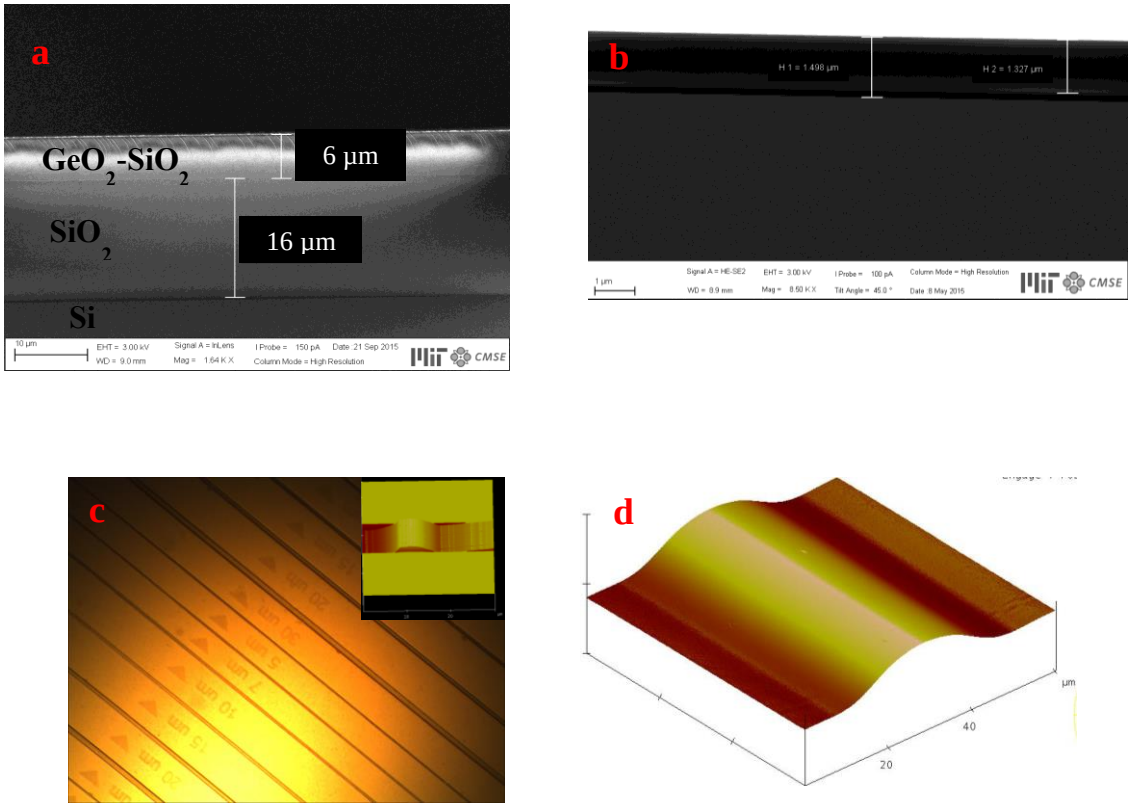


Figure 5.10: SEM images of (a) GeO2-$SiO_2$ (b) AZ-resist (c) Optical image & AFM images of agarose etched $GeO_2$-$SiO_2$ (d) AFM images of agarose etched AZ resist.

## 5.7 Conclusion

In this chapter, we have successful patterned microscale high gel strength agarose hydrogels (12-13 % w/v) and utilized the advantage of its high water holding

capacity for solution-based pattern transfer. We further demonstrated that agarose hydrogel based wet stamping may be a suitable alternative transfer printing method for fabricating microscale optical device for photonics applications. This method can be further optimized to print nanoscale structures by tuning to agarose stiffness, etchant concentration.

However, the method was unsuccessful for integration of TBZ materials as the front side LSG structures on solar cell since the acidic etchant solution will degrade the solar cells performance. Therefore, we focused on integration and performance evaluation of backside LSG structures on solar cell using chalcogenide glass thin film with composition $As_{20}Se_{80}$. This composition meets the target material requirements for backside LSG structures as discussed in [144]

# Chapter 6

# LOW SYMMETRY GRATING (LSG) INTEGRATION ON BACK SIDE OF THIN CRYSTALLINE SILICON (c-Si) SOLAR CELL

## 6.1 Motivation for LSG integration on Thin Film c-Si Solar Cells

Solar technology uses the sun's energy to provide electricity, heat, light water even cooling for homes and business across the globe. Solar cells technology has been at the leading spot of the bulk of green and sustainable solutions to the global energy challenges. The research strength focused on the technology has received tremendous successes but these breakthroughs still lack the capacity to properly position solar technology to favorably compete with fossil fuel energy and meet $1 per watt demand. The drawbacks in meeting this demand are solar cell production cost and efficiency improvement. According the chart below (**Figure 6.1**), material cost constitutes bulk of silicon solar production cost and material reduction creates viable solution.

Reducing c-Si wafer thickness to less than 50 micron significantly reduces material cost and may result in improvement in efficiency by reducing bulk recombination. However, thickness scaling of silicon solar cells suffers poor optical absorption of incident photon near its band edge because the penetration depth of these photons exceeds cell thickness and also that silicon is an indirect band gap semiconductor. To ensure effective photon collection for thin c-Si cells especially around the near infrared region, new concepts are required. Integration of diffractive low symmetry grating structure on the rear side is one of the viable approaches to enhance optical path length of incident photon and ensure optimum incident photon

collection by the solar cell absorber before they leak back to free space. To integrate these diffractive structures onto completely processed solar cells, we developed a well optimized and low cost fabrication process following a well-known thermal nano-imprint process. **Figure 6.2** shows schematics of low symmetry grating integration process flow on the rear side of thin c-Si solar cells. The process step involves: (**1**) Si master fabrication (a) thermal oxidation of silicon dioxide hard mask layer on an offcut silicon (Si (112)) wafer; (b) fabrication of sub-micro period low symmetry grating (LSG) on light sensitive polymer material via lithography (electron beam lithography or photolithography); (c) transfer of the LSG patterns to silicon master via dry (reactive ion etch) and wet etching (anisotropic KOH etch); (**2**) replication of LSG structures on polydimethylsiloxane (PDMS) stamp via soft lithography process; (**3**) imprinting of LSG structures on thermal evaporated $As_{20}Se_{80}$ thin film deposited on the rear side of 50 um thick c-Si solar cells in Argon environment; (**4**) coating of low index polymer (SU8 spacer) to prevent further oxidation of $As_{20}Se_{80}$ glass film and reduce parasitic loss from metals contacts; (**5**) deposition of aluminum back reflectors.

In this chapter, we present the details steps of fabricating and integrating of sub-wavelength diffractive low symmetry grating on the rear side of 30 µm thick c-Si solar cells to improve optical absorption and boost efficiency.

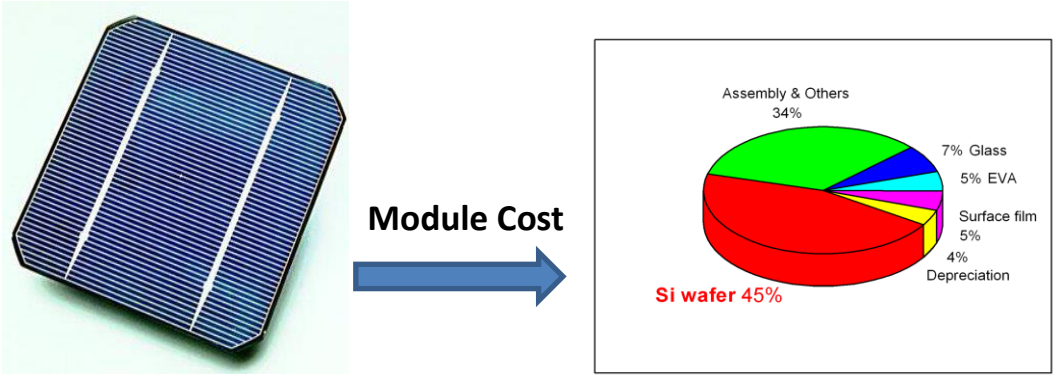

Figure 6.1: Bar chart showing the production cost of making a module of silicon solar cell.

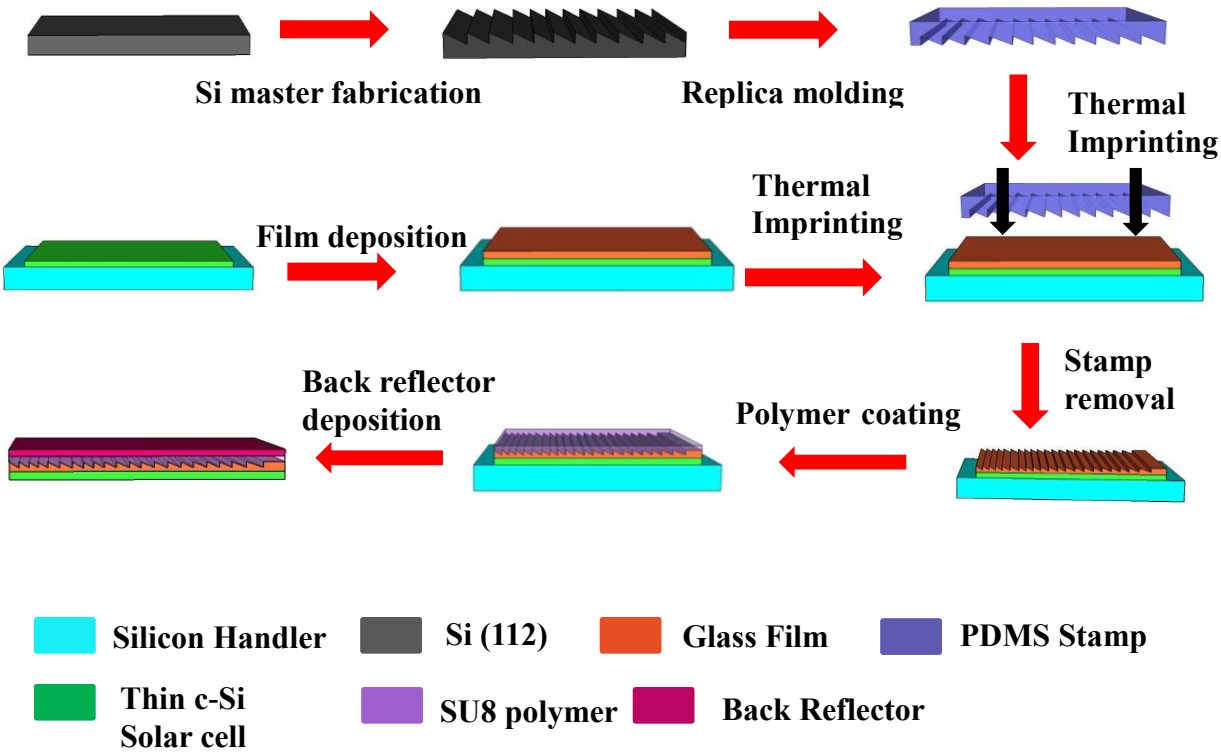


Figure 6.2: Schematic showing the process-flow of LSG integration on thin c-Si solar cells.

## 6.2 Grating Fabrication on Silicon Master

In the section, we present optimized and repeatable steps developed for fabricating sub-micro gratings on silicon (Si (112)) master for replica molding to create PDMS stamps. We successfully fabricated both symmetric and Low symmetry gratings on silicon wafers. We want to highlight that these silicon master can be

reused multiple times (more than 50 times) without any significant deterioration on the patterns integrity.

### 6.2.1 Fabrication of Symmetric Grating Master

The master mold of symmetric gratings that will be used as a comparison to the asymmetric gratings can be fabricated by Inductively Coupled Plasma (ICP) etching of silicon. ICP etching followed by e-beam lithography is a reliable technology to produce micron-size structures with controllable dimensions.

To fabricate the grating mold, we first defined resist pattern on Si wafer using electron-beam lithography, and then ICP was applied to etch the silicon material. The resist were removed in the last step by oxygen plasma. In order to have vertical grating sidewall, we used multiplexed anisotropic Si etching with the detailed recipe shown in **Table 6.1**.

The steps listed in **Table 6.1** constitute a single loop of the etching process. The number of loops needed depends on the depth of the grating. The etching rate was calibrated by running different number of loops and is approximately 75 nm per loop.

Table 6.1: The parameters of multiplexed anisotropic Si etching

| Step | Gases | Pressure/ Position | ICP/Bias (W) | Time |
|---|---|---|---|---|
| 1 | | 100% | 0/0 | 10 sec |
| 2 | 20 sccm $C_4F_8$ | 4 Pa | 0/0 | 15 sec |
| 3 | 20 sccm $C_4F_8$ | 4 Pa | 450/0 | 3 sec |
| 4 | 20 sccm $C_4F_8$ | 4 Pa | 450/15 | 7 sec |
| 5 | | 100% | 0/0 | 10 sec |
| 6 | 25 sccm $SF_6$ | 2 Pa | 0/0 | 15 sec |
| 7 | 25 sccm $SF_6$ | 2 Pa | 500/0 | 3 sec |
| 8 | 25 sccm $SF_6$, 5 sccm Ar | 2 Pa | 500/100 | 2 sec |
| 9 | 25 sccm $SF_6$, 12.5 sccm Ar | 0.75 Pa | 500/25 | 9 sec |

A top-view SEM image of a master mold of symmetric silicon grating after ICP etching is shown in **Figure 6.3**. A successful pattern transfer can be observed from the figure. The gratings have a period of 800 nm with a line-width of 400 nm, which is ideal for solar cell light-trapping. The vertical sidewall of the etched gratings is shown in Figure 7.1, indicating that the successful anisotropic etching of silicon by ICP. The depth of the grating is 300 nm, which is also an ideal dimension for solar cell light-trapping and nano-imprint lithography.

**(a)** **(b)**

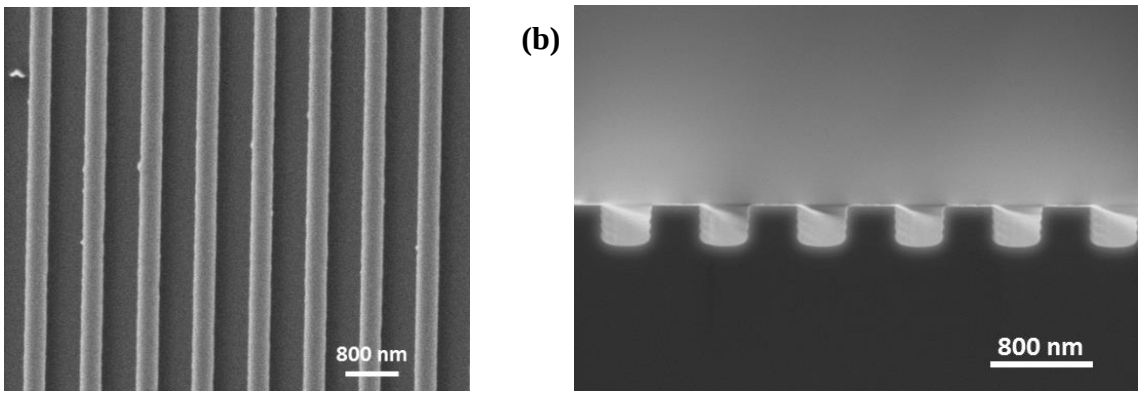


Figure 6.3: (a) Top-view & (b) cross-sectional SEM image of ICP etched Si grating master mold.

### 6.2.2 Fabrication of Micro-scale Low Symmetric Grating (LSG) Master

Here we enumerate the steps involved in making V-groove gratings on silicon wafers which serves as a master for replica molding via photolithography. Before photo-resist deposition, an silica layer (220 nm thick ) was deposited on the silicon wafers using wet thermal oxidation technique. Silica has good selectivity to silicon and serves as the hard mask to protect some areas of silicon during etching. The sample for photo-lithography is prepared by spin coating NR9-1500PYon the wafer at a spin speed of 2500 rpm for 40 secs then baked for 80 secs at 150 $^{o}$C to remove

moisture. The pattern on the chrome mask was carefully aligned parallel to (110) direction of the wafer and exposed to UV rays for 20 secs using MJB3 Mask Aligner. After exposure the samples were post baked for 80 secs at 100 $^{o}$C then sample was developed using RD 6 developer for 15 secs and rinsed in deionized water.We carried out buffered oxide etch (BOE) etching at 1.1 nm /sec to strip the silica layer and open windows to transfer the patterns onto the silicon layer. Anisitropic chemical wet etching technique was used to transfer the micor-scale patterns on silicon. Anisotropic etching etch rate depends on the orientation of crystalline planes. Anisotropic potassium hydrooxide (KOH) etching was done at an etch rate of 1.1 μm/min and temperature of 78 $^{o}$C to selectively etch the sample since KOH etches about hundreds of magnitude faster in (100) direction than (111) direction in silicon wafer. **Figure 6.4** shows SEM cross-sectional images of 1-D V-groove gratings etched on (100) and (211) off-cut Si wafers. As expected, anisotropic wet etching of off-cut wafers leads to asymmetric grating patterns for LSG imprint fabrication.

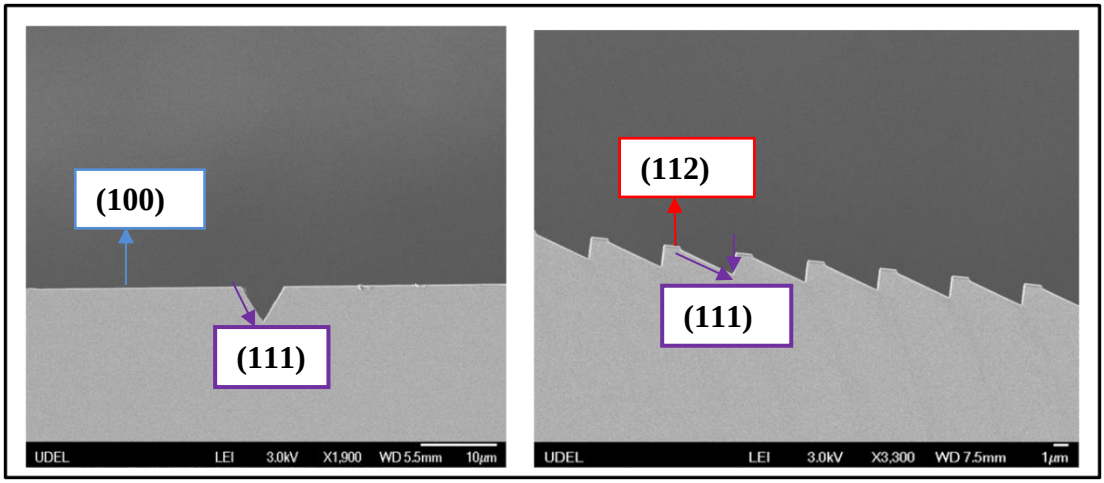


Figure 6.4: SEM cross-sectional images of: (Left) Symmetric V-grooves etched on (100) Si wafers; (Right) shark fin-shape asymmetric grooves etched on (211) off-cut Si wafers.

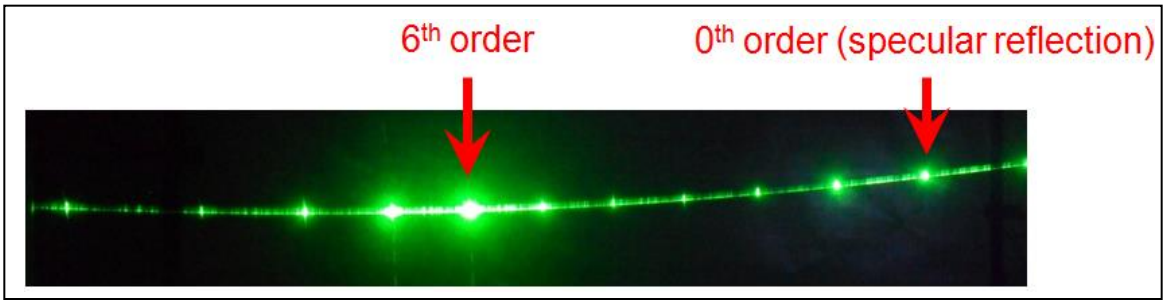


Figure 6.5: Photo of laser diffraction patterns from the etched (211) wafer surface.

We tested the performance of the gratings etch on silicon using a set-up with a green laser source operating at 532 nm wavelength. **Figure 6.5** shows the diffraction grating pattern of 1-D grating obtained using a green laser at 532 nm wavelength. The grating pattern confirms that surface defects on the 1-D grating has zero effect on the grating performance. The blazing angle is 19.5$^{o}$ and angle between two (111) direction is 70.6$^{o}$. In the Littrow configuration, blazing was observed in the 6$^{th}$ dirraction order.

### 6.2.3 Sub-micro Low Symmetry Gratings (LSG) v-grooves Fabrication on Off-cut Silicon Master

Here, we enumerate the steps involved in fabricating sub-micron LSG v-groove on Si (112) wafer which serves as a master for nano-imprint and micro transfer molding. An oxide layer (124 nm thickness) was deposited on the off-cut silicon wafers using dry thermal oxidation technique. The oxide layer serves as the hard mask during etching. The sample for e-beam lithography is prepared by spin coating ZEP photoresist on the wafer at 4000 rpm for 45 secs and baked at 180 $^{o}$C for 60 secs.

ZEP is non conducting polymer therefore electron accumulation during exposure causes drifting of electron beam. Electron drifting during exposure leads to proximity effect where electrons writing a feature at one location increase exposure in a nearby location resulting in pattern distortion and overexposure. E-beam exposure is

performed on *Elinoix* ELS-F125 DRAFT and proximity effect correction (PEC) was done, using Beaver software©, to obtain uniform dimension over the exposed area.

Prior to exposure, we performed ZEP exposure dose and linewidth calibration to optimize exposure parameters suitable dose for e-beam patterning. We carried out these calibrations to determine the effect of PEC on writing grating dimension. **Figure 6.6 a & b** show the scanning electron microscopy (SEM) images of patterns exposed without applying PEC and non-uniform dimension of the gratings over different regions on same sample indicate the broadening effect of electron drift due to electron accumulation. To correct this non-uniformity, we applied PEC during exposure and obtained a uniform grating dimension as shown in **Figure 6.7 a & b.** The optimized e-beam parameters are 400 μC/cm$^2$ dose, 4 nA current & 125 KV accelerating voltage were used in writing the desired grating dimensions (in our case: period= 890 nm, linewidth= 174 nm, gap= 715 nm) for replicating stamps based on our simulation results as shown in **Figure 6.7 c**.

The patterns were aligned parallel to [110] direction of the offcut Si (112) wafer then exposed by electron beam using optimized parameters. The patterns transferred on the wafer are 1-D grating. After exposure the samples were developed using ZED-N50 for 10 secs, rinsed IPA.

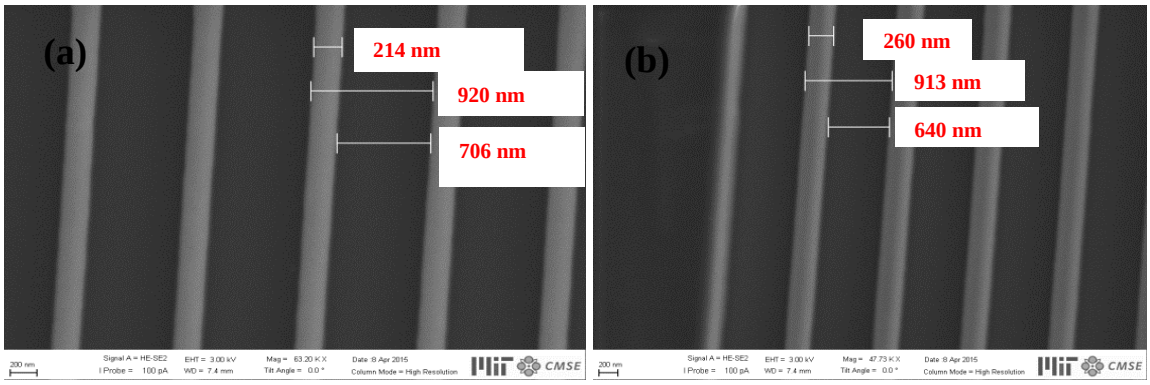

Figure 6.6: SEM images: Top view grating patterns (a) pattern at centre (b) patterns at edge; obtained using optimized e-beam parameters without proximity effect correction on ZEP resist spun on Si (112) wafer & patterned via e-beam lithography.

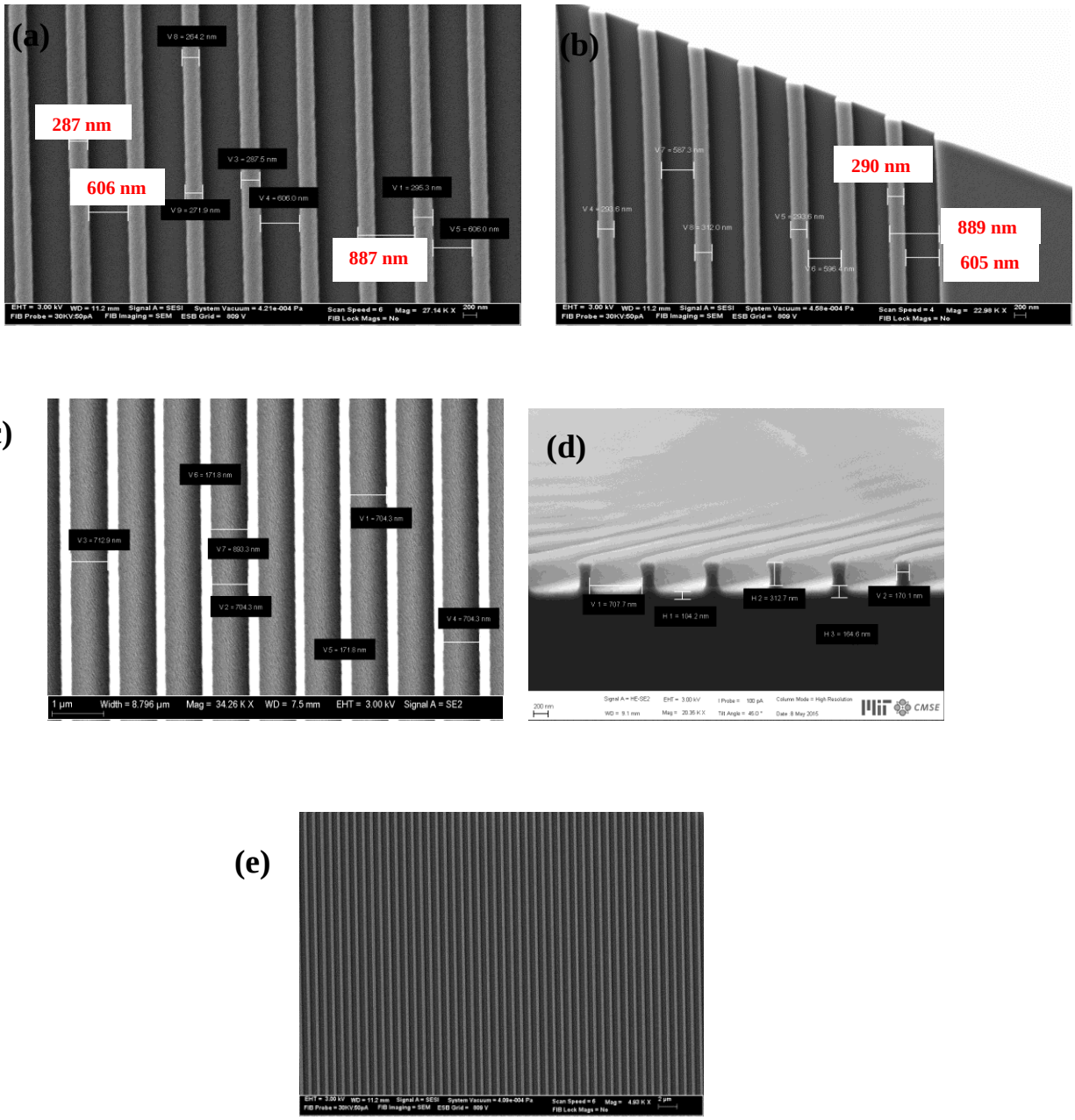

Figure 6.7: SEM images: Top view grating patterns (a) pattern at centre (b) patterns at edge (c) final Si master with desired grating parameters used for replica molding (d) RIE etching showing that ZEP optimized thickness offered good resistance to etch silica layer (e) full view; obtained using optimized e-beam parameters after proximity effect correction on ZEP resist spun on Si (112) wafer & patterned via e-beam lithography.

Reactive ion etching (RIE) was performed to selectively etch the silica layer using $CF_4$ & $CHF_3$ gases at the rate of 30 nm /sec. The best etching condition is with 30 mTorr pressure, 45 sccm $CHF_3$, 15 sccm $CF_4$, 200 W RF power at 150 $^oC$. RIE selectively transfers the patterns onto the oxide layer and opens access to silicon layer for anisotropic wet etching process. ZEP provides good etch resistance for fluorine based gas and 1: 20 etch selectivity with silica as shown in **Figure 6.3 d**. Prior to KOH etching step, the polymer (ZEP electron beam resist) was stripped off using Piranha ( $H_2SO_4$:$H_2O_2$ solution ) to prevent polymer residue from creating unwanted masking during plasma etching.

Anisotropic chemical etching is a well-known technique for fabricating simple microstructures and nanostructures in crystalline silicon. Anisotropic etchant commonly used for Si chemical wet etching is potassium hydroxide (KOH). KOH etches about hundreds of magnitude faster in (100) direction than (111) direction on silicon wafer, anisotropic KOH etching was done in 36% KOH+ 15% IPA solution at 1.1 μm/min and 78 $^oC$ to selectively etch asymmetric v-grooves on silicon layer. Addition of IPA improves the surface roughness due to the increased wettability of the resulting etchant. This process reduces the stability of hydrogen bubbles by varying surface tension. Adding IPA can liberate water particles in the close vicinity of Si surface by hindering hydration of $K^+$ and $OH^-$ ions [145]. This mechanism prevents

the formation of pyramidal hillocks, which known as the most common reasons for having a higher surface roughness of the Si <100>. The presence of IPA interrupts the access of OH- ions across the surface and reduces the oxidation rate. This provides equilibrium in diffusion and oxidation of reaction products and decreases the duration of the attached hydrogen bubbles to the etched surface, which leads to have more smoothness of the surface [146, 147].

Finally, the $SiO_2$ hard mask layer were removed by dipped into dilute hydrofluoric acid (HF), an aqueous solution with a well-known ability to dissolve $SiO_2$. **Figure 6.4 a** shows the SEM result show the images of asymmetric gratings with period 890 nm (712 nm width, 178 nm gap) and 350 nm depth etched on silicon with $SiO_2$ hard mask layer while AFM result (**Figure 6.4 b)** depicts the map of the asymmetric gratings on silicon after $SiO_2$ stripping and the angle between the (112) and (111) plane is about $19^o$.

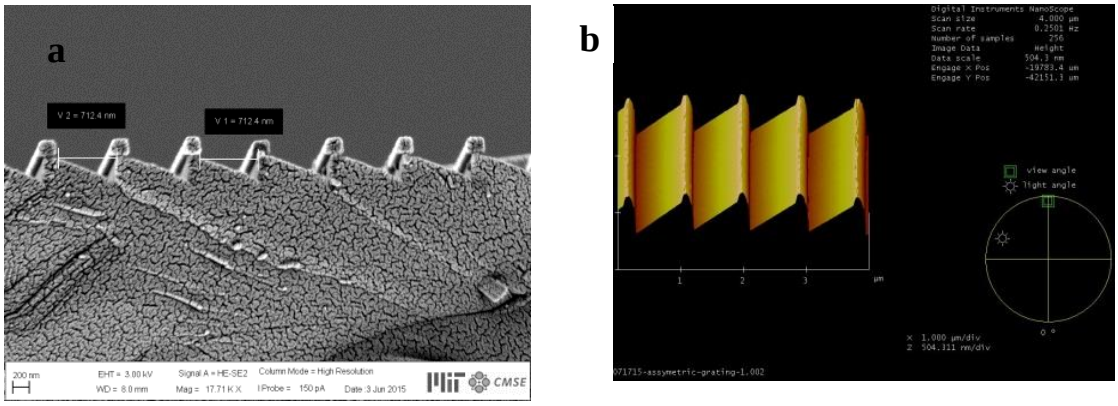


Figure 6.8: SEM images: (a) Tilt view of asymmetric gratings on Si (112) after KOH etching; (b) AFM scan of asymmetric gratings on Si (112) after $SiO_2$ hard mask removal.

## 6.3 Bi-layer Composite Polydimethylsiloxane (PDMS) Stamp Fabrication

Elastomeric molds (stamps) based of PDMS (Sylgard 184 Dow Corning) have been a popular and versatile material for soft lithography because of its flexibility and simple fabrication by replica molding. The PDMS stamps made from this material (referred to as "soft-PDMS") suffer from (i) lateral and roof collapse because of its low modulus; (ii) incomplete filling of deep holes and grooves in a master template as a result its viscosity and poor wettability.

PDMS Stamp collapse limits its ability to fabricate structures in the size scale below 500 nm [137]. Consequently, to meet the current demand the fabrication of structures below 500 nm for soft lithography process and address the relatively low modulus of PDMS, an alternative elastomer material have been explored. A polymer based on vinyl and hydrosilane end-linked polymers (referred as "hard –PDMS") [148] has been successfully developed for fabrication of high density structures beyond the limit of PDMS. The improved performance of hard-PDMS (h-PDMS) is attributed to its better mechanical properties compare to those of Sylgard 184 PDMS. Although the high modulus of h-PDMS worked well for replication, high coefficient of thermal expansion (450 µm $m^{-1}$ $^{o}C$ for h-PDMS vs 260 µm $m^{-1}$ $^{o}C$ for s-PDMS) and handling of these stamps was difficult because of cracking and break off from the master upon cooling. To address this, a bilayer composite stamp that uses a thick slab of s-PDMS to support a thin h-PDMS for improved pattern transfer [149]. To completely fill the master templates with deep hole and grooves (beyond 120 nm), several groups [148, 150] proposed the addition of a suitable solvent to reduce the viscosity of h-PDMS and improve wettability on master templates. Following their reports, we prepared an improved bilayer composite PDMS stamp for sub-wavelength pattern transfer using thermal nanoimprint process.

In nanoimprint lithography (NIL), it is essential to coat master with good anti-sticking surface properties. A low surface energy release layer on the master helps to improve the imprint quality. In our experiment, the Si-master was coated with 1 µL of fluorinated trichlorosilane anti-sticking agent in a desiccator for 20 secs to ensure easy release of PDMS mold from the silicon master after PDMS curing.

Hard-PDMS molds (h-PDMS) were prepared by mixing 1.7 g vinyl PDMS prepolymer (VDT-731, Gelest Corp), 0.05 g modulator (2, 4, 6, 8-tetramethyl-2, 4, 6, 8-tetravinylcyclotetrasiloxane, 87927, sigma Aldrich), 0.5 g of hydrosilane prepolymer (HMS-301, Gelest) and 18 µL of Pt catalyst (Platinum divinyltetramethyldisiloxane). To this mixture, 1 g of toluene (solvent) was introduced and stirred. The solvent lowers the viscosity and improves wettability of the prepolymer. The h-PDMS solution is spun on the Si-master at 2000 rpm for 30 s and left undisturbed for about 2 hrs to provide enough time for the solution to penetrate into the groove depths and ensure complete solvent evaporation. Then the sample was baked for 20 mins at 60 $^{o}$C. The modulator used in preparation of the h-PDMS mold lowers the rate of cross-linking to allow more time the prepolymer to completely fill up the groove depth in the Si-master and for the solvent to completely evaporate but does not take part in the crosslinking reactions.

A soft-PDMS (s-PDMS) handle was prepared, following the standard soft-lithography process to provide adequate support for handling thin h-PDMS. The monomer and curing agent (Sylgard 184) were mixed in the ratio of 1:10 and thoroughly stirred. The PDMS mixture was then poured onto the master, in a petri dish, placed on a leveled and flat surface in a vacuum oven. The mixture is degassed in vacuum to remove air bubbles trapped on stirring then cast on the h-PDMS layer

and cured at 60 $^{o}$C for 3-4 hrs. The PDMS stamp was peeled from the Si master cut into blocks 6 mm$^2$ for thermal imprinting on 30 um thin c-Si solar cells. We made > 10 stamps from a single master without any significant deterioration of the master.

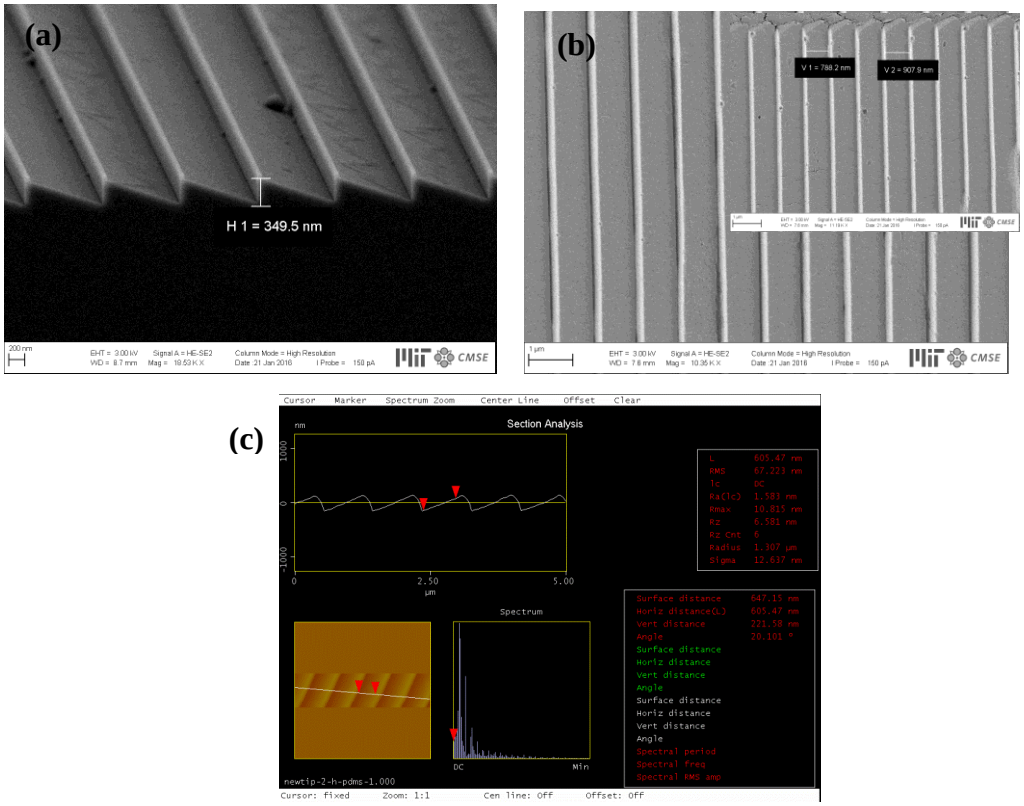


Figure 6.9: SEM images (a) Cross-Section view of asymmetric nano-gratings Si master after PDMS cast; (b) Top view of PDMS stamp after release from Si master; (c) AFM scan of the nano-gratings PDMS stamp.

The stamp's morphology was characterized using SEM & atomic force microscopy (AFM). The bi layer composite PDMS stamps were covered with a thin (~ 30 nm) Au coating prior to SEM and AFM imaging (i) to minimize charging from electron accumulation on the sample surface; (ii) to reduce AFM tip sticking on

PDMS surface during measurement. **Figure 6.9 a & b** show the cross-section view Si master after the PDMS stamp is removed and top view of bilayer composite PDMS stamp. As observed from the images, the near-zero residue on the Si master and inverted pyramid structure of the patterns on the PDMS indicate that there a good pattern transfer form Si-master onto PDMS stamp. AFM scan shown in **Figure 6.9 c** depicts similar structure as observed in **Figure 6.8 c** with blazing angle of about $19.5^{o}$ which is also the angle between (112) and (111) plane. This indicates that lowering the viscosity of the h-PDMS pre-polymer mixture enhances the filling of the asymmetric grating depth and improves pattern transfer from the Si-master to PDMS mold.

## 6.4 Thin Film Deposition on Thin c-Si Solar Cells via Thermal Evaporation

Bulk glasses of composition $As_{20}Se_{80}$ were prepared using a traditional melt-quenching technique using commercial agents [144]. Thin films were deposited, by thermal evaporation, on both 30 µm thin c-Si solar silicon wafers and on the backside of thin c-Si solar cells (samples prepared by Institute of Energy Conversion at University of Delaware). Prior to thermal evaporation, the substrates were mounted on thick silicon wafer to provide mechanical support and ensure easy handling through the processing steps. Thermal evaporation of powdered glass was carried out at a base pressure $<10^{-6}$ Torr in a custom-designed single-source evaporator (PVD Products, Inc.). A 300 nm-thick $As_{20}Se_{80}$ thin films were deposited on the substrates at deposition rate was maintained at ~10 Å/s. The substrates were maintained at room temperature throughout the deposition. Thermal evaporation deposition conditions were optimized with respect to the optical performance of the deposited films (e.g. thickness uniformity and surface quality) and were extremely repeatable.

## 6.5 Thermal Nanoimprint of Low Symmetry Grating (LSG) Evaporated Chalcogenides

Thermal imprinting of nano-scale LSG on chalcogenide glass thin film was done at elevated temperature and pressure. The process depends on the fluidity of the selected glass material at imprint temperature and the stamp loading pressure. Since viscosity is the critical parameter that kinetically guides the imprint process, optimum imprinting conditions required to define conditions of glass flow are guided by prior knowledge of the base glass' viscosity- temperature behavior [151].

Besides, chalcogenides glasses undergo oxidation when annealed in ambient environment, thermal imprinting of LSG on $As_{20}Se_{80}$ thin films deposited on thin c-Si solar cell was performed in an argon purged glove box to prevent oxidation of glass thin films. The glass film sample along with the soft stamp was placed on a hotplate pre-set at imprint temperature. Imprint pressure of approximately 0.13 MPa was applied by loading a metal block on the film-stamp assembly at 153 $^{o}$C for 35 mins. Using the optimized conditions, the applied load and temperature cause the material to flow and conform to the shape of the stamp pattern. The stamp was then manually delaminated from the glass film sample and allowed to cool to room temperature. No evidence of crystallization of $As_{20}Se_{80}$ thin films was observed after thermal imprint process [144]. The imprinted grating morphology was characterized using scanning electron microscopy.

**Figure 6.10** shows cross section SEM images of 890 nm period LSG grating with smooth surface imprinted on $As_{20}Se_{80}$ thin films deposited on silicon substrate. The excellent replication of the asymmetric grating dimensions from the PDMS stamp indicates quality pattern transfer with low roughness to eliminate scattering loss.

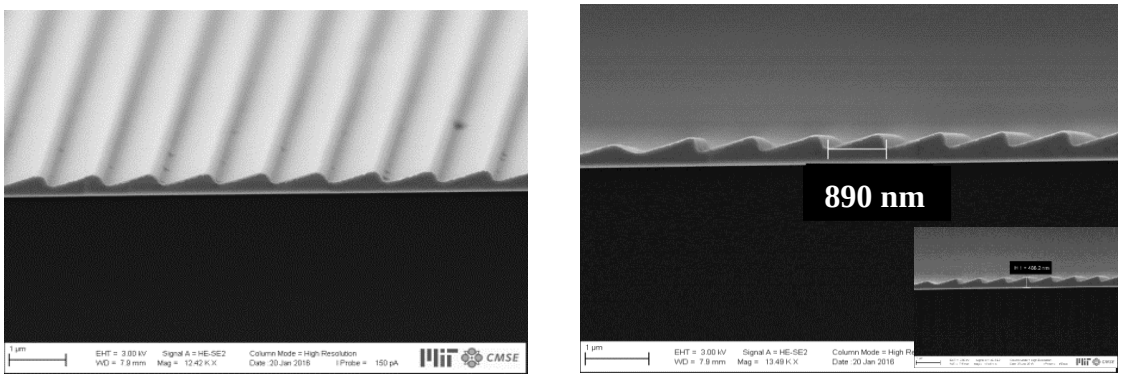


Figure 6.10: SEM image tilted and cross-section view of LSG imprinted on thermal evaporated $As_{20}Se_{80}$ deposited Si wafer

An optically transparent, low index dielectric polymer material was spin coated to prevent oxidation of $As_{20}Se_{80}$ glass thin film and reduce parasitic loss from metal integrated with gratings on solar cells backside as shown in **Figure 6.11**. Throughout the entire grating imprint processing, the cells' metal busbars was protected by aluminum foil to avoid the deposition of glass film and ensure good contact for IV measurement.

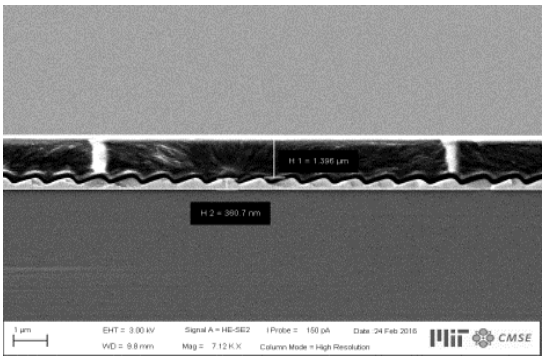

Figure 6.11: SEM cross-section view image of low index polymer material spun on the backside integrated LSG on 30 µm solar cell.

To this end, we have successfully integrated chalcogenide based low symmetric gratings (LSG) on the backside of both thin (30 um) c-Si wafers and thin film c-Si solar cells. These gratings were coated with low index polymer materials using an optimized and repeatable process. Finally, we characterized the device performance to determine the contributions of LSG to light trapping as discussed in chapter 7

# Chapter 7

## PERFORMANCE OF BACKSIDE LOW SYMMETRIC GRATINGS (LSG) ON THIN FILM CRYSTALLINE SILICON (c-Si) CELLS

### 7.1 Motivation

In this chapter, we presented the device performance results obtained after LSG integration process. Absorption enhancement characterization on 30 um thin c-Si wafers (both side polished) was done with UV-Vis spectrophotometer while Current-Voltage (JV) and external quantum efficiency (EQE) measurement were carried out to probe the solar cell performance.

### 7.2 Demonstration of Absorption Enhancement on 30 µm Thin c-Si Wafers

To characterize optical absorption enhancement of low symmetric gratings (LSG) integrated on 30 µm thick c-Si wafer, a Perkin-Elmer 1050 UV-Vis spectrophotometer with integrating sphere was used to record the total transmittance spectra and total reflectance spectra of samples in the range of 400-1400 nm.
An integrating sphere is an optical component consisting of a hollow spherical cavity with its interior covered with a diffuse white reflective coating, small holes for entrance and exit ports. The samples were prepared by depositing $As_{20}Se_{80}$ film onto 30-µm thick silicon wafer using thermal evaporation method. The LSG were then thermally imprinted by using PDMS with optimized parameters. Gratings with period of 890 nm and area of 5mm by 5mm were successfully imprinted on 30-µm thick silicon. A polymer material, transparent in over 400 – 1400 nm, was coated to prevent

oxidation of $As_{20}Se_{80}$ thin film. The total absorption in sample was calculated using the following relation in **Equation 7.1**

Absorption (%) = 100% - Reflectance (%) – Transmittance (%)..... (Eqn 6.1)

The total transmittance was measured by placing the sample in the front of the integrating sphere during the transmittance measurement and the reflectance white standard on the back to prevent the optical leakage as shown in **Figure 7.1 a & b**. The reflecting white standard randomly reflects all transmittance light from the sample into the sphere and is finally absorbed by the detector. The total reflectance was measured by placing the sample on the back as depicted in **Figure 7.2**. Similar to transmittance light, all the reflected light was randomly reflected in the sphere and was finally absorbed by the detector.

The total absorption of grating integrated thin c-Si is capture using **Equation 7.1**. **Figure 7.3** is the absorption spectrum that compares the absorption effect of on bare 30 µm c-Si wafer to those with LSG. The plot shows LSG integrated at the backside of 30 µm c-Si wafer excites more optical modes that contribute to light trapping leading to enhanced absorption from 850 -1100 nm due to prolonged photon-matter interaction. Comparing the contribution of both symmetric and LSG structure at long wavelength, we observed that LSG structures show about 10 % improved absorption in thin ci-Si wafers than symmetric structures.

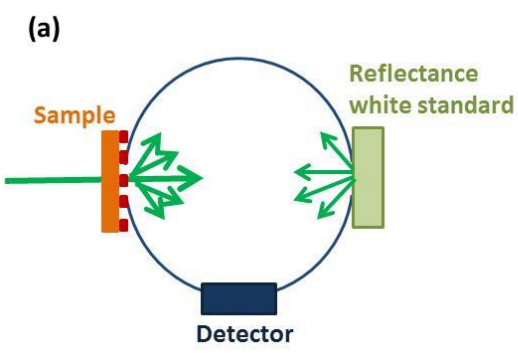


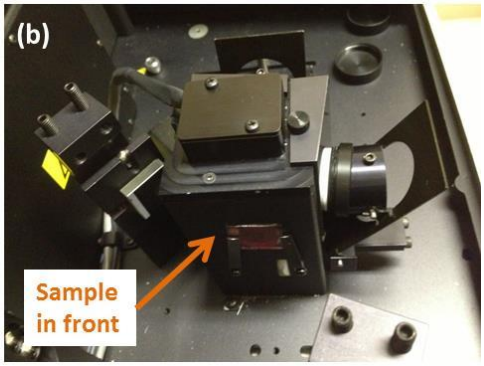

Figure 7.1: (a) A schematic illustration of an integrating sphere measuring the total transmittance spectral by placing a sample in front and a reflectance white standard on the back. (b) A sample was placed in the front of an integrating sphere for the transmittance measurement.

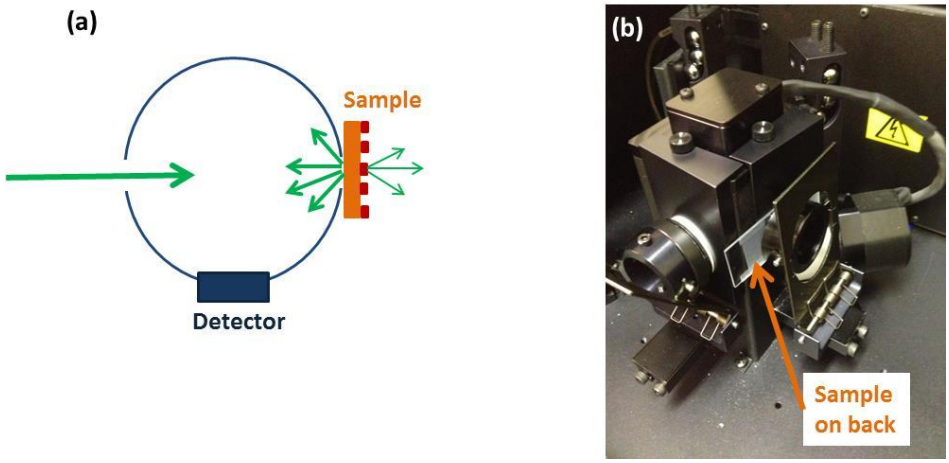


Figure 7.2: (a) A schematic illustration of an integrating sphere measuring the total reflectance spectral by placing a sample on the back. (b) A sample was placed on the back of an integrating sphere for the reflectance measurement.

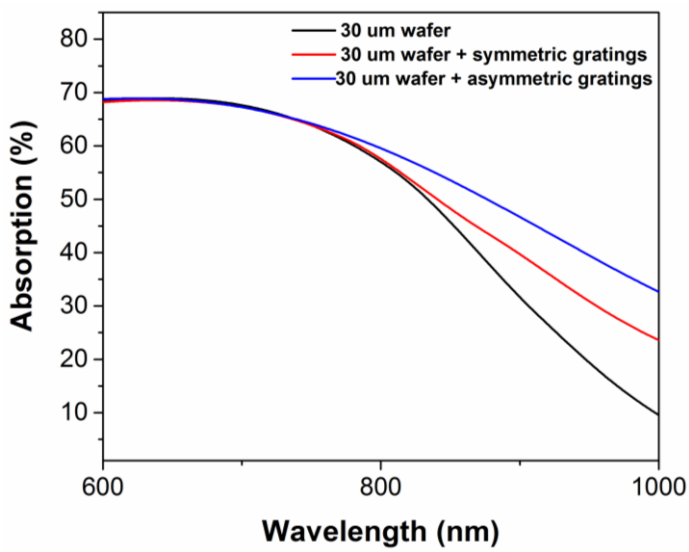

Figure 7.3: Optical absorption measured in a 30-µm c-Si wafer showing optical absorption enhancement in samples with backside gratings.

## 7.3 JV and External Quantum Efficiency (EQE) Measurement Characterization of Thin c-Si Solar Cell

**Figure 7.4 a** is an illustration of the architecture of bifacial (MC1575 batch) thin c-Si solar cell device with low symmetric grating at the back side. This device was processed on a 30 µm thick Si absorber layer. The 30 µm absorber layer was fabricated, using wet etching technique, by etching 300 µm in 25% tetramethylammonium hydroxide (TMAH) at 90°C for ~4 h followed by short HNA etching (30:10:40 hydrofluoric acid-nitric acid-acetic acid mixture) at room temperature. The device structure consists of a-Si passivation layers deposited by plasma enhanced chemical vapor deposition (PECVD) on the wafer and completed with ITO and metal grids as the contacts. The device was processed with a large full cell area of 1 sq. in., covering almost the complete wafer surface. Sub-micron grating with 890 nm period and 5 x 5 $mm^2$ area were imprinted on the backside of the device. On top of the grating, a 500 nm thick layer of aluminum was deposited (via electron beam evaporation technique) serving as a back reflector layer. JV curves of the cell were measured using a shadow mask over the grating layer areas. To compare the performance of the portions of the cell with gratings to that without, a 5 x 5 $mm^2$ area of the cell with no grating coverage was measured by JV with the shadow mask. **Table 7.1**. lists JV data MC1575 cell measurements comparing both cells with gratings and bare cell showing improvement in solar cell efficiency even though there is no corresponding $J_{sc}$ improvement in the solar cell.

Table 7.1: JV data MC1575 cell measurements

| | Area ($cm^2$) | $V_{oc}$ ( mV) | Jsc ($mA/cm^2$) | FF (%) | η (%) |
|---|---|---|---|---|---|
| After Grating | **0.4** | **624** | **23.40** | **55.80** | **8.10** |
| Before Grating | **0.56** | **599** | **25.13** | **47.50** | **7.15** |

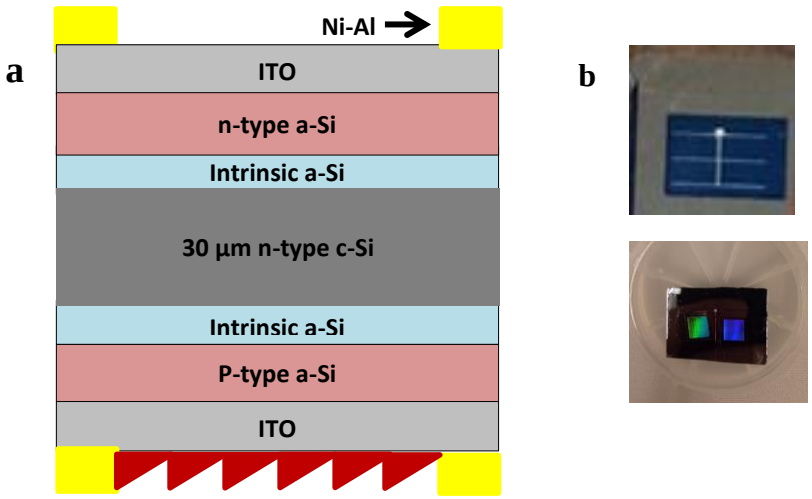


Figure 7.4: (a) Thin bifacial Silicon hetero-junction architecture in substrate configuration (n-i-p) (b) Optical images of bifacial c-Si solar cell before and after Low symmetric grating integration.

Quantum efficiency (QE) measurements of the cells were carried out on a cell without aluminum back reflector and results are shown in Figure 7.5. The plot indicate an improved performance of cells with LSG around 800 – 950 nm over the cells without grating. A back reflector will provide enhanced device performance of the solar cell.

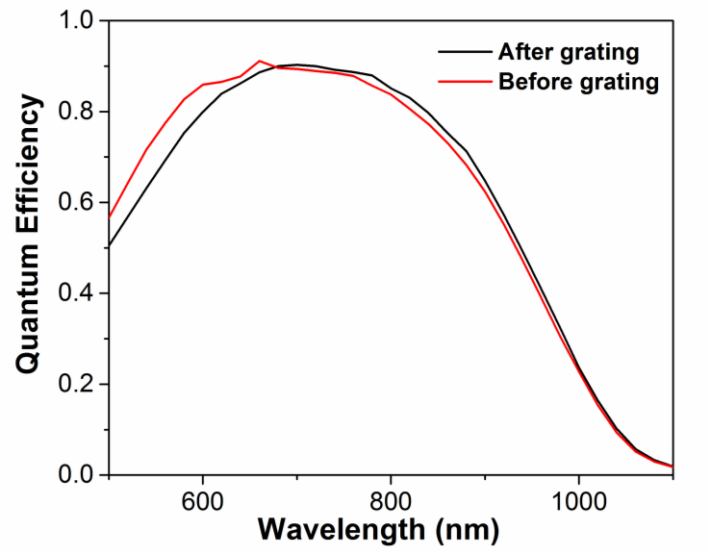


Figure 7.5: Quantum Efficiency measurement comparing thin solar cells with LSG to and thin solar cells without LSG.

# Chapter 8

# SUMMARY & FUTURE WORK

## 8.1 Summary

To favorably compete with fossil-fuel technology, the greatest challenge for thin film solar-cells is to improve efficiency and reduce cost. Thickness scaling to thin film reduces cost but affects the light absorption in the cells, therefore a concept that traps light and increases its optical path length are needed in thin film solar. This concept involves integration of low symmetric grating (LSG) on thin film glass deposited thin c-Si cell (30 µm). These grating structures could be integrated on either the front or the back side of thin c-Si solar cells to enhance incident photons optical path.

Multicomponent $TeO_2$–$Bi_2O_3$–ZnO (TBZ) glass thin films were prepared using RF magnetron sputtering under different oxygen flow rates. Impacts of oxygen flow rate on the structural and optical properties of the resulting thin films were investigated. We observed that thin films sputtered in an oxygen-rich environment are optically transparent while those sputtered in an oxygen-deficient environment exhibit broadband absorption. The structural origin of the optical property variation was studied using X-ray diffraction, X-ray photoelectron spectroscopy, Raman Spectroscopy, and transmission electron microscopy which revealed that the presence of under-coordinated Te leads to the observed optical absorption in oxygen-deficient

films. These observed properties confirm that TBZ is an ideal candidate for the front side LSG material for PV application.

We choose chalcogenide glasses (ChGs) as the back side gratings material due to their attractive optical and structural properties, such as high refractive indices, transparency in the near-IR, and amorphous structure amenable to low cost imprint patterning. We successful deposited chalcogenide glass thin film (300 nm) with composition ($As_{20}Se_{80}$), on c-Si wafers and solar cells using optimized thermal evaporation process. This composition exhibits superior properties such low viscosity and glass imprint temperature making it suitable fabricating sub micro LSG using low cost nano-imprinting method.

On the fabrication level, we demonstrated a simple maskless method to pattern micro structures on sputtered tellurite glass thin films using agarose hydrogel mediated wet etching. Conventional wet etching process, while claiming low cost and high throughput, suffers from reproducibility and pattern fidelity issues due to the isotropic nature of wet chemical etching when applied to glasses and polymers. This method overcomes these challenges by using an agarose hydrogel stamp to mediate a conformal etching process. In our maskless method, agarose hydrogel stamps are patterned following a standard soft lithography and replica molding process from micropatterned photoresist masters and soaked in a chemical etchant. The micro-scale features on the stamp are subsequently transferred into glass and polymer thin films via conformal wet etching. We successfully demonstrated that the process can be applied to thin film photonic/photovoltaic device fabrication in a wide range of glass and polymer materials.

Finally, we developed a well-designed and optimized protocol for integrating sub-wavelength scale low symmetric gratings on the $As_{20}Se_{80}$ thin film at the backside of 30 µm c-Si wafer and solar cells. We demonstrated that c-Si wafers integrated with sub micro scale LSG has enhanced absorption near the band edge of Si compared to those without gratings.

## 8.2 Future Work

We are developing plans to demonstrate the fabrication nano-scale structures on tellurite based thin film via our unconventional wet stamping process and further integration of LSG for front side c-Si PV application.

## REFERENCES


1. M. Green and S. Pillai, "Harnessing Plasmonics for solar-cells", Nature Photonics, **6** 130-132 (2012).
2. www.transparency.eex.com/en/
3. www.popularmechanics.com "Solar Panel drops to $1 per Watt: Is this a Milestone or the bottom for silico-based panels?"
4. J. Rand, R. Hall and A. Barnett, "Light trapping in thin crystalline silicon solar cells," Proc. 21st IEEE Photovoltaic Specialists Conf. pp. 263 (1990).
5. M. Stocks, A. Carr, A. Blakers, "Texturing of polycrystalline silicon," Sol. Energy Mater. Sol. Cells **40**, 33-42 (1996).
6. J. Krč, F. Smole, and M. Topič, "Potential of light trapping in microcrystalline silicon solar cells with textured substrates," Prog. Photovolt. Res. Appl. **11**, 429-436 (2003).
7. H. Sai, H. Fujiwara, M. Kondo, and Y. Kanamori, "Enhancement of light trapping in thin-film hydrogenated microcrystalline Si solar cells using back reflectors with self-ordered dimple pattern," Appl. Phys. Lett. **93**, 143501 (2008).
8. S. B. Mallick, M. Agrawal, and P. Peumans, "Optimal light trapping in ultra-thin photonic crystal crystalline silicon solar cells," Opt. Express **18**, 5691–5706 (2010).
9. R. Dewan, M. Marinkovic, R. Noriega, S. Phadke, A. Salleo, and D. Knipp, "Light trapping in thin-film silicon solar cells with submicron surface texture," Opt. Express **17**, 23058-23065 (2009).
10. P. Bermel, C. Luo, L. Zeng, L. C. Kimerling, and J. D. Joannopoulos, "Improving thin-film crystalline silicon solar cell efficiencies with photonic crystals," Opt. Express **15**, 16986-17000 (2007).
11. E. Yablonovitch, "Statistical ray optics," J. Opt. Soc. Am. A **72**, 899-907 (1982).
12. P. Campbell, and M. A. Green, "The limiting efficiency of silicon solar-cells under concentrated sunlight," IEEE Trans. Electron. Dev. **33**, 234–239 (1986).
13. J. Cotter, "Optical intensity of light in layers of silicon with rear diffuse reflectors," J. App. Phys. **84,** 618-624 (1998).

14. H. Sai, H. Jia, and M. Kondo, “Impact of front and rear texture of thin-film microcrystalline silicon solar cells on their light trapping properties,” J. Appl. Phys. **108**, 044505 (2010).
15. Z. Yu, A. Raman, and S. Fan, “Fundamental limit of nanophotonic light trapping in solar cells,” Proc. Natl. Acad. Sci. **107**, 17491 (2010).
16. S. Han and G. Chen, “Toward the Lambertian Limit of Light Trapping in Thin Nanostructured Silicon Solar Cells,” Nano. Lett. **10**, 4692-4696 (2010).
17. S. Pillai, K. Catchpole, T. Trupke, and M. A. Green, “Surface plasmon enhanced silicon solar cells,” J. Appl. Phys. **101**, 093105 (2007).
18. D. Zhou, and R. Biswas, “Photonic crystal enhanced light-trapping in thin film solar cells,” J. Appl. Phys. **103**, 093102 (2008).
19. J. Yoo, G. Yu, and J. Yi, “Large-area multicrystalline silicon solar cell fabrication using reactive ion etching (RIE),” Sol. Energy Mater. Sol. Cells **95**, 2-6 (2011).
20. K. Lai, F. Tsai, J. Wang, C. Yeh, and M. Houng, “Wet-etch texturing of ZnO:Ga back layer on superstrate-type microcrystalline silicon solar cells,” Sol. Energy Mater. Sol. Cells **95**, 1583-1586 (2011).
21. R. Groenen, J. Loffler, P. Sommeling, J. Linden, E. Hamers, R. Schropp, and M. van de Sanden, “Surface textured ZnO films for thin film solar cell applications by expanding thermal plasma CVD,” Thin Solid Films **392**, 226-230 (2001).
22. M. Python, E. Vallat-Sauvain, J. Bailat, D. Domine, L. Fesquet, A. Shah, and C. Ballif, “ Relation between substrate surface morphology and microcrystalline silicon solar cell performance,” J. Non-Cryst. Solids **354**, 2258-2262 (2008).
23. H. Li, K. van der Werf, J. Rath, and R. Schropp, “Hot wire CVD deposition of nanocrystalline silicon solar cells on rough substrates,” Thin Solid Films **517**, 3476-3480 (2009).
24. N. Barreau, J. Lahnemann, F. Couzinie-Devy, L. Assmann, P. Bertoncini, and J. Kessler, “Impact of Cu-rich growth on the $CuIn_{1-x}Ga_xSe_2$ surface morphology and related solar cells behavior ”, Sol. Energy Mater. Sol. Cells **93**, 2013-2019 (2009).
25. In visible and near-infrared, refractive indices of chalcogenide glasses range from 2.0 to 3.5 depending on the glass composition. Multi-component oxide glasses such as heavy metal oxides typically have refractive indices between 1.8 and 2.5. See: http://mit-pbg.mit.edu/Pages/AsSeTe.html.

26. J. Hu, V. Tarasov, N. Carlie, L. Petit, A. Agarwal, K. Richardson, and L. C. Kimerling, “Fabrication and testing of planar chalcogenide waveguide integrated microfluidic sensor,” Opt. Express **15**, 2307 (2007).
27. S. Madden, K.T Vu, “Very low loss reactively ion etched Tellurium Dioxide planar rib waveguides for linear and non-linear optics” Optics Express 17, 20 17645 (2009).
28. W. Li, S. Seal, E. Megan, J. Ramsdell, K. Scammon, G. Lelong, L. Lachal, and K. A. Richardson, “Physical and optical properties of sol-gel nano-silver doped silica film on glass substrate as a function of heat-treatment temperature,” J. Appl. Phys. **93**, 9553 (2003).
29. J. Massera, J. Choi, L. Petit, M. Richardson, Y. Obeng, and K. Richardson, “Comparison of the Au nanoparticle formation and dissolution mechanisms with those of Cu and Ag nanoparticles in $SiO_2$ sol-gel films,” submitted.
30. T. Benson, A. Vukovic, P. Sewell, A. Loni, Y. Zhang, W. Pan, D. Zhang, M. O’Donnell, J. Lousteau, D. Furniss, A. Seddon, "Novel glass compositions and fabrication technologies for photonic integrated circuits," Proc. ICTON 2005, Tu B2.2, Barcelona, Spain (2005).
31. Z. Lian, W. Pan, D. Furniss, T. Benson, A. B. Seddon, T. Kohoutek, J. Orava, and T. Wagner, “Embossing of chalcogenide glasses: mono mode rib optical waveguides in evaporated thin films”, Opt. Lett. **34**, 1234-1236 (2009).
32. C.J Campbell, S.K Smoukov, K.J.M Bishop, E. Baker, B.A Grzybowski, “Direct printing of 3D and curvilinear micro-meter sized architectures into solid substrates with sub micro-meter resolution”, Adv. Mater. **18** 2004 (2006).
33. B.A Grzybowski, K.J.M Bishop, “Micro- and Nano-printing into solids using reaction-diffusion etching and hydrogel stamps”, Small **5**, 1, 22 (2009).
34. J.Ozdanova, H. Ticha, L. Tichy, “Remark on the optical gap in ZnO-Bi2O3-TeO2 glasses”, J. Non-Cryst. Solids **353** 2799 (2007).
35. R.A. Myers, N. Mukherjee, S.R.J. Brueck, “Large second-order nonlinearity inpoled fused silica”, Optics Letters **16**, 1732 (1991).
36. S.H. Kim, T. Yoko, “Nonlinear optical properties of $TeO_2$-based glasses: $MO_x$-$TeO_2$ (M= Sc, Ti, V, Nb, Mo, Ta, and W) Binary Glasses”, Journal of the American Ceramic Society **78** (4)**,** 1061-1065 (1995).
37. R.A.H. El-Mallawany, Tellurite Glasses Handbook, CRC Press, 2000, p. 113.
38. R. Jose, and Y. Ohishi, “Enhanced Raman gain coefficients and bandwidths in $P_2O_5$ and WO added tellurite glasses for Raman gain media,” Appl. Phys. Lett. **89**(12), 221122-221125 (2006).

39. N. G. Boetti, et al., “Thermal Stability and Spectroscopic Properties of Erbium-Doped Niobic-Tungsten-Tellurite Glasses for Laser and Amplifier Devices,” J. Luminescence, 132 1265–1269 (2012).
40. A. Jha, S. Shaoxiong, H. Li Hui, and P. Joshi, “Spectroscopic properties of rare earth metal ion doped tellurium oxide glasses and fibres,” J. Opt. **33**, 157-176 (2004).
41. E. B. Intyushin, and V. A. Novikov, “Tungsten-tellurite glasses and thin films doped with rare-earth elements produced by radio frequency magnetron deposition,” Thin Solid Films **516** (12), 4194–4200 (2008).
42. P. T. Lin, Michiel Vanhoutte, Neil S. Patel, Vivek Singh, Juejun Hu, Yan Cai, Rodolfo Camacho-Aguilera, Jurgen Michel, Lionel C. Kimerling,Anu Agarwal, “Engineering broadband and anisotropic photoluminescence emission from rare earth doped tellurite thin film photonic crystals,” Optics Express **20** (3) 2124-2135 (2012).
43. P. A. Thomas, “The crystal structure and absolute optical chirality of paratellurite α-$TeO_2$ ”, J. Phys. C: Solid State Phys. **21** (1988) 4611.
44. A.P. Mirgorodsky, T. Merle-Mejean, J.C. Champarnaud, bP.Thomas, B.Frit, “Dynamics and structure of $TeO_2$ polymorphs: model treatment of paratellurite and tellurite; Raman scattering evidence for new γ- and δ – phases,” Journal of Physics and Chemistry of Solids **61** 501-509 (2000).
45. O. Linqvist, “Refinement of the Structure of α-TeO2”, Acta Chemica Scandinavica **22**(3), 977-982 (1968).
46. S. Neov, I. Gerasimova, K. Krezhov, B. Sidzhimov, V.Kozhukharov, “Atomic Arrangement in Tellurite Glasses Studied by Neutron Diffraction”, Phys. Status Solidi (a) **47**, 743 (1978).
47. E.F. Lambson, G.A. Saunders, B. Bridge, R.A. El-Mallawany, “ The Elastic behaviour of $TeO_2$ glass under uniaxial and hydrostatic pressure”, J. Non-Cryst. Solids **69**, 117 (1984).
48. M. Tatsumisago, S.K. Lee, T. Minami, and Y. Kowada, ‘‘Raman Spectra of $TeO_2$-Based Glasses and Glassy Liquids: Local Structure Change with Temperature in Relation to Fragility of Liquid,’’ J. Non-Cryst. Solids, **177**, 154– 63 (1994).
49. T. Yoko, K. Kamiya, K. Tanaka, H. Yamada, S. Sakka, “Glass-Forming region and structure of oxyhalide tellurite glasses containing LiX (X=F and Br) and $LiO_2$” Journal of the Ceramic Society of Japan 97**,** 289 (1989).
50. A. Osaka, Q. Jianrong, T. Nanba, Y. Miura, and T. Yao, “EXAFS of tellurium in the glasses of $B_2O_3$-$TeO_2$ system,” J. Non-Cryst. Solids, **142**, 81-86 (1992).
51. M.A. Salim, G.D. Khattak, N. Tabet, and L.E. Wenger, “X -Ray photoelectron spectroscopy (XPS) studies of copper–sodium tellurite glasses,” Journal of Electron Spectroscopy and Related Phenomena, **128**, 75-83, (2003).

52. M.O'Donell, "Tellurite and Flouorotellurite Glasses for Active and Passive Fibreoptics Waveguides", PhD. Thesis, Universtiy of Nottingham, 2004.
53. E. Chierici, M. C. Didavide, A. Moro, O. Rossotto, L. Tallone, and E. Monchiero, "Direct Writing of Waveguide on a Tellurite Glass Using a Focused Ultraviolet Laser Beam," IEEE/LEOS Workshop on Fibre and Optical Passive Components, IEEE Press, Piscataway, NJ, USA, 29–33, 2002.
54. Y. Tokuda, et al., "Waveguide Formation in Niobium Tellurite Glasses by Pico- and Femtosecond Laser Pulses," J. Non-Cryst. Solids, 326 472–475 (2003).
55. P. Nandi, et al., "Femtosecond Laser Written Channel Waveguides in Tellurite Glass," Opt. Express, 14 12145–12150 (2006).
56. G. Nunzi Conti, et al., "Characterization of Ion-Exchanged Waveguides in Tungsten Tellurite and Zinc Tellurite $Er^{3+}$-Doped Glasses," Opt. Eng., 42 2805–2811 (2003).
57. G. Nunzi Conti, et al., "Ion-exchanged Planar Waveguides in Different $Er^{3+}$-doped Tellurite Glasses," Rare-Earth-Doped Materials and Devices VII, eds., S. Jiang and J. Lucas. SPIE, San Jose, CA, USA, 97–102, 2003.
58. I. Banyasz, et al., "MeV Energy N+-Implanted Planar Optical Waveguides in Er-Doped Tungsten-Tellurite Glass Operating at 1.55 lm," IEEE Phot. J., **4** 721–727 (2012).
59. S. Berneschi, et al., "Ion Beam Irradiated Channel Waveguides in Er3+ -Doped Tellurite Glass," Appl. Phys. Lett., **90** 121136-1–121136-3 (2007).
60. M. D. O'Donnell, D. Furniss, V. K. Tikhomirov, D. Briggs, E. F. Smith, and A. B. Seddon, "Surface Properties of Tellurite and Fluorotellurite Glasses," J. Mat. Res., **22** 1673–1684 (2007).
61. S. M. Pietralunga, et al., "High-Contrast Waveguides in Sputtered Pure TeO2 Glass Thin Films," Opt. Express, **16** 21662–21670 (2008).
62. V. D. D. Cacho, A. L. Siarkowski, N. I. Morimoto, B. H. Borges, and L. R. Kassab, "Fabrication and Characterization of $TeO_2$-ZnO Rib Waveguides," ECS Trans., **31** 225–229 (2010).
63. M. Lanata, M. Fere, D. Piccinin, S. M. Pietralunga, and M. Martinelli, "Sputtered tellurite glass thin films for planar optical devices," International Conference on Transparent Optical Networks, (ICTON 2008), 227–230, 2008.
64. T. Siciliano, M. Di Giulio, M. Tepore, E. Filippo, G. Micocci and A. Tepore , " Effects of thermal annealing time on optical and structural properties of TeO2 thin films", Vacuum. 84, 935 (2010).
65. M F Al-Kuhaili, S M A Durrani, E E Khawaja and Shirokoff, "Effects of preparation conditions on the optical properties of thin films of tellurium oxide" J. Phys. D: Appl. Phys. 35, 910 (2002).
66. B.J Eggleton, B. Luther-Davies, K. Richardson, "Chalcogenides Photonics", Nature Photonics, **5** 141 (2011).
67. J. Hu, V. Tarasov, N. Carlie, L. Petit, A. Agarwal, K. Richardson, and L. C. Kimerling, "Exploration of Waveguide Fabrication From Thermally Evaporated Ge-Sb-S Glass Films," Opt. Mater. **30**, 1560 (2008).

68. Yu, Z.F. and S.H. Fan, Angular constraint on light-trapping absorption enhancement in solar cells. Applied Physics Letters, 98(1) (2011).
69. Yu, Z.F., A. Raman, and S.H. Fan, Fundamental limit of light trapping in grating structures. Optics Express, **2**. 18(19) A366-A380 (010).
70. Preble, S., M. Lipson, and H. Lipson, Two-dimensional photonic crystals designed by evolutionary algorithms. Applied Physics Letters, 86(6) (2005).
71. Jiang, J.H., et al., Parallel microgenetic algorithm design for photonic crystal and waveguide structures. Optics Letters, 28 (23) 2381-2383 (2003).
72. Lin, A. and J. Phillips, Optimization of random diffraction gratings in thin-film solar cells using genetic algorithms. Solar Energy Materials and Solar Cells, 92(12) 1689-1696 (2008).
73. Sheng, X., et al., Design and Non-Lithographic Fabrication of Light Trapping Structures for Thin Film Silicon Solar Cells. Advanced Materials, 23(7) 843 (2011).
74. G. Guery et al. "Impact of tellurite-based glass structure on Raman gain," Chemical Physics Letters 554 123-127(2012).
75. R.A. Myers, N. Mukherjee, and S.R.J. Brueck, "Large Second-Order nonlinearity in poled fused silica," Optics Letters **16**, 1732-1734 (1991).
76. G. Guery et al., "Influence of hydroxyl group on IR transparency of tellurite-based glasses", International Journal of Applied Glass Science 1-7 (2013).
77. X. Hu, G. Guery, J. Boerstler, J.D. Musgraves, D. Vanderveer, P. Wachtel, and K. Richardson "Influence of $Bi_2O_3$ content on the crystallization behavior of $TeO_2$-$Bi_2O_3$-ZnO glass system," J. Non-Crystalline Solids **358** 952-958 (2012).
78. J. Massera et al., "Processing and characterization of a core-clad tellurite glass preforms and fibers fabricated by rotational casting," J. Optical Materials **32** 5 582-588 (2010).
79. R.A.H. El-Mallawany, Tellurite Glasses Handbook, CRC Press, 2000, p. 113.
80. B. Richards et al., "Tellurite glass lasers operating close to 2 um," Laser Phys. Lett. **7**, 3, 177–193 (2010).
81. K. Tanaka et al., "Optical second harmonic generation inpoled MgO–ZnO–$TeO_2$ and$B_2O_3$–$TeO_2$ glasses," J. Non-Cryst. Solids, **203,** 49-54 (1996)
82. J. S. Wang, E. M. Vogel, and E. Snitzer, "Tellurite glass: a new candidate for fiber devices," Opt. Mater. **3**(3), 187–203 (1994).
83. M.R. Oermann, H. Ebendorff-Heidepriem, Y. Li, T. Foo, and T. M. Monro, "Index matching between passive and active tellurite glasses for use in microstructure fiber lasers: Erbium doped lanthanum-tellurite glass", Optics Express, **17** (18), 15578-15584 (2009).

84. C. Rivero et al., “Influence of modifier oxides on the structural and optical properties of binary $TeO_2$ glasses,” J. Applied Physics **101** (2), 023526-7 (2007).
85. E. Yousef, M. Hotzel, and C. Rüssel, “Effect of ZnO and $Bi_2O_3$ addition on linear and non-linear optical properties of tellurite glasses,” J. Non-Cryst.Solids, **353,**333–338(2007).
86. R. Jose, and Y. Ohishi, “Higher non-linear indices, Raman gain coefficients and bandwidths in the $TeO_2$-ZnO-$NbO_5$-$MoO_3$ quaternary glass system,” Appl. Phys. Lett. **90,** 211104-3 (2007).
87. M.R Henderson et al. “Diamond in Tellurite glass: a new medium for quantum information,” Adv. Mater. 23, 2806-2810 (2011).
88. Y. Ruan, K. Boyd, H. Ji, A. Francois, H. Ebendorff-Heidepriem, J. Munch, and T. M. Monro, “Tellurite microspheres for nanoparticle sensing and novel light sources,” Optics Express, **22** (10), 11995-12006 (2014).
89. J. I. Mackenzie, G. S. Murugan, A. W. Yu, J. B. Abshire, “ Er-doped tellurite waveguides for power amplifiers” Proc. SPIE 8988, Integrated Optics: Devices, Materials, and Technologies XVIII, 898809 (2014).
90. L. Li et al., “Integrated flexible chalcogenide glass photonic devices,” Nature Photonics **8,** 643-649 (2014).
91. Juejun Hu, Lan Li, Hongtao Lin, Ping Zhang, Weidong Zhou, and Zhenqiang Ma, "Flexible integrated photonics: where materials, mechanics and optics meet [Invited]," Opt. Mater. Express **3**, 1313-1331 (2013)
92. L.Weng, S.N.B Hodgson, and J. Ma, “Preparation of $TeO_2$-$TiO_2$ thin films by sol-gel process,” Journal of Materials Science Letters **18,** 2037-2039 (1999).
93. M. Bouazaouiet al., “Pulsed Laser Deposition of Er-doped tellurite films on large area”, Journal of Physics: Conference Series 59, 475-478 (2007).
94. A.P Caricato et al., “$Er^{3+}$-doped tellurite waveguides deposited by excimer laser ablation” Mat. Sci. Eng B **105**, 65-69 (2003).
95. F. D’Amore et al., “Sputtered Stoichiometric $TeO_2$ glass films: Dispersion of Linear and nonlinear optical properties”, J. Appl. Phys. **94**, 1654-1661 (2003).
96. M. D. Giulio, M.C. Nicotra, M. Re, R. Rella, and P. Siciliano, “ Optical Absorption and Structural characterization of reactively sputtered tellurium suboxide thin films”, Appl. Surf. Sci.65/66, 313-318 (1993).
97. H.T. Fan, S.S. Pan, X.M. Teng, C. Ye, G.H. Li, and L.D. Zhang, “δ-$Bi_2O_3$ thin films prepared by reactive sputtering: Fabrication and characterization,” Thin Solid Films 513 142–147 (2006).

98. N. Dewan, V. Guputa, K. Sreenivas, and R.S. Katiyar, "Growth of amorphous $TeO_x$(2<x<3) thin film by radio frequency sputtering", J. Appl. Phys., **101**, 084910-7 (2007).
99. J. Massera, A. Halderman, J. Jackson, C. Rivero-Baleine, L. Petit, and K. Richardson, " Processing of tellurite-based glass with low OH content," J.Am.Ceram.Soc., **94 (1),** 130-136 (2011).
100. M. Tatsumisago, S.K. Lee, T. Minami, and Y. Kowada, ''Raman Spectra of $TeO_2$-Based Glasses and Glassy Liquids: Local Structure Change with Temperature in Relation to Fragility of Liquid,'' J. Non-Cryst. Solids, **177**, 154– 63 (1994).
101. J. Heo, G.H. Sigel Jr, E.A. Mendoza, and D.A Hensley, "Spectroscopic analysis of the structure and properties of alkali tellurite glasses," J. Am. Ceram. Soc. **75,** 277-281 (1992).
102. T. Sekiya, N. Mochida, A. Ohtsuka, M. Tonokawa, "Raman spectra of $MO_{1/2}$-$TeO_2$ (M=Li, Na, K, Rb, Cs,and Tl) glasses," J. Non-Cryst. Solids, **144**, 128-144 (1992).
103. J.Jackson, C. Smith, J. Massera, C. Rivero-Baleine, C. Bungay, L. Petit, and K. Richardson, "Estimation of peak Raman gain coefficients for Barium-Bismuth-Tellurite glasses from spontaneous Raman cross-section experiments," Optics Express, **17**, 9071-9079 (2009).
104. J. W. Weber, T. A. R. Hansen, M. C. M. van de Sanden, and R. Engeln, "B-spline Parameterization of the dielectric function applied spectroscopic Ellipsometry on amorphous carbon," Journal of Applied Physics **106**, 123503-9 (2009).
105. G. E. Jellison, and F. A. Modine, "Parameterization of the optical functions of amorphous materials in the interband region," Appl. Phys. Lett.**69** 371-373 (1996).
106. R. Nayak, V. Gupta, A.L. Dawar, and K. Sreenivas, "Optical waveguiding in amorphous tellurium oxide thin films," Thin Solid Films **445**, 118-126 (2003).
107. C. H. Heo, S. Lee, and J. Boo, "Deposition of $TiO_2$ thin films using RF magnetron sputtering method and study of their surface characteristics," Thin Solid Films **475** 183-188 (2005).
108. M. Chandra Sekhar, P. Kondaiah, B. Radha Krishna, and S. Uthanna, "Effect of Oxygen Partial Pressure on the Electrical and Optical Properties of DC Magnetron Sputtered Amorphous $TiO_2$Films," Journal of Spectroscopy **2013**,462734 (2013).

109. G.E. Mullenberg (Ed), Handbook of X-ray Photoelectron Spectroscopy, Perkin-Elmer, Norwalk, CT, 1970.
110. T. S. Sian and G. B. Reddy, "Optical, structural and photoelectron spectroscopic studies on amorphous and crystalline molybdenum oxide thin films," Sol. Energy Mater. Sol. Cells **82**, 375-386 (2004).
111. W.E. Morgan, W. J. Stec, and J. R. Van Wazer "Inner-Orbital Binding-Energy Shifts of Antimony and Bismuth Compounds," Inorganic Chemistry, **12**, 4, 953-955 **(**1973).
112. C.D. Wagner, W.M. Riggs, L.E. Davis, J.F. Moulder, and G.E. Muilenberg, Handbook of X-ray Photoelectron Spectroscopy, Perkin-Elmer Corporation, Physical Electron Division, Eden Prairie, Minn. 55344 (1979).
113. H.W Nesbitt, G.M Bancroft, G.S Henderson, R. Ho, K.N Dalby, Y. Huang, Z. Yan, "Bridging, non-bridging and Free ($O^{-2}$) oxygen in $Na_2O$-$SiO_2$ glasses: An X-ray Photoelectron Spectroscopic(XPS) and Nuclear Magnetic Resonance (NMR) study," J. Non-Cryst. Solids, **357,** 170-180 (2011).
114. G.D Khattak, A. Mekki and L.E Wenger, "Local structure and redox state of copper in tellurite glasses*,"* J. Non-Cryst. Solids, **377,** 174-181 (2004).
115. A.J. Ricco, H.S. White, and M.S. Wrighton, "X-ray photoelectron and Auger electron spectroscopic study of the CdTe surface resulting from various surface pretreatments: Correlation of photo-electrochemical and capacitance-potential behavior with surface chemical composition," J. Vac.Sci.Techol. A, **2**,910 (1984).
116. R. El-Mallawany, A. Abdel-Kader, M. El-Hawary, and N. El-Khoshkhany, "*UV-IR spectra of new tellurite glasses*," Eur. Phys. J. AP **19**, 165 172 (2002)
117. V.K. Tikhomirov, A.B. Seddon, D. Furniss, and M. Ferrari, "Intrinsic defects and glass stability in $Er^{3+}$-doped $TeO_2$ glasses and the implications for $Er^{3+}$-doped tellurite fiber amplifiers," J. Non-Cryst. Solids, **326** 296-300 (2003).
118. M. DiGiulio, G. Micocci, R. Rella, P. Sicilano, and A. Tewre, "Optical Absorption of Tellurium Suboxide Thin Films," Phys. Stat. Sol (a) 136 K101 (1993).
119. B. Jeansannetas et al., "Glass Structure and Optical Nonlinearities in Thallium (I) Tellurium (IV) Oxide Glasses," Journal of Solid State Chemistry, **146**, 329-335 (1999).
120. H. Burger, K. Kneipp, H. Hobert, W. Vogel, V. Kozhukharov, and S. Neov, "Glass formation, properties and structure of glasses in the $TeO_2$-ZnO system," J. Non-Cryst. Solids **151**, 134–142 (1992).

121. S.O. Baki, L.S. Tan, C.S. Kan, H.M. Kamari, A.S.M. Noor, and M.A. Mahdi, "Structural and optical properties of $Er^{3+}$-$Yb^{3+}$codopedmulticomposition $TeO_2$-ZnO-PbO-$TiO_2$-$Na_2O$ glass," J. Non-Cryst. Solids, **362,** 156-161 (2013).
122. J.Ozdanova, H. Ticha, and L. Tichy, "Remark on the optical gap in ZnO-$Bi_2O_3$-$TeO_2$ glasses," J. Non-Cryst. Solids, **353**, 2799-2802 (2007).
123. S.R Quakes, A.Scherer, "From Micro- to Nanofabrication with Soft Materials", Science **290**, 1536-1539 (2000).
124. Y.N Xia, E. Kim, X.M. Zhao, J.A Rogers, M. Prentiss, G.M. Whitesides, "Complex Optical Surface Formed by Replica Molding Against Elastomeric Masters" Science **273**, 347-349 (1996).
125. Handbook of Plasma Processing Technology: Fundamentals, Etching, Deposition and Surface Interactions (Eds: S.M Rossnagel, J.J Cuomo, W.D Westwood), Noyes, Park Ridge, NJ 1990.
126. C.B. Schaffer A. Brodeur, J.F Garcia, E. Mazur, Micromachining Bulk Glass by use of Femtosecond Laser Pulses with Nanojoule Energy" Opt. Lett. **26**, 93-95 (2001).
127. N. Coq, T. van Bommel, R.A. Hikmet, H.R Stapert, W.U. Dittmer, "Self-Supporting Hydrogel Stamps for the Microcontact Printing of Protein", Langmuir **23**, 5154-5160 (2007).
128. M. Mayer, J. Yang, I. Gitlin, D. H. Gracias and G. M. Whitesides, "Micropatterned agarose gels for stamping arrays of proteins and gradients of proteins", Proteomics, **4**, 2366–2376 (2004).
129. M. M Stevens, M. Mayer, D. G Anderson, D. B Weibel, G. M Whitesides, R Langer, "Direct Patterning of Mammalian Cells onto Porous Tissue Engineering Substrates using Agarose Stamps", Biomaterials 26 7636-7641 (2005).
130. N. Fatin-Rouge, A. Milon, J. Buffle, Diffusion and partitioning of solutes in agarose hydrogels: the relative influence of electrostatic and specific interactions, J. Phys. Chem., B **107** 12126–12137 (2003).
131. M. Djabourov, A.H Clark, D.W Rowlands, S.B Ross-Murphy, "Small-Angle X-ray Scattering Characterization of Agarose Sols and Gels", Macromolecules **22** 180-188 (1989).
132. M. Maaloum, N. Pernodet, B. Tinland, "Agarose gel structure using atomic force microscopy: gel concentration and ionic strength effects", Electrophoresis, **1** 1606–1610 (1998).
133. E.W Becker, W. Ehrfeld, P. Hagmann, A. Maner, D. Muenchmyer, "Fabrication of microstructure with high aspect ratios and great structural

heights by synchrotron raditaion lithography, galvanoforming and plastic moulding(LIGA process)", Microelectron. Eng. **4** 35 (1994).

134. J.M. Bustillo, R.T. Howe, R.S. Muller, "Surface Micromachining for microelectromechanical systems", Proc. IEEE **86** 1552 (1998).
135. D.J. Ehrlich, R.M. Osgood, T.F Deutsch, "Laser chemical technique for rapid direct writing of surface relief in silicon" Appl. Phys. Lett. 38 1018 (1981).
136. L.M. Ephrath, "Selective Etching of Silicon Dioxide Using Reactive Ion Etching with $CF_4$-$H_2$", J. Electrochem. Soc **126** 1419 (1979).
137. Y. N. Xia, G. M. Whitesides, "Soft Lithography"Annu. Rev. Mater. Sci., **28** 153 (1998).
138. P. Lin, M. Vanhoutte, R. Camacho, Y. Cai, L. C. Kimerling, K. Richardson, A. Agarwal, and J. Hu, "Temperature-enhanced light emission from Er-$TeO_2$ Photonic Crystals," OSA Integrated Photonics Research, Silicon and Nano Photonics Conference, Toronto, Canada (2011).
139. Stephan Keller , Gabriela Blagoi, Michael Lillemose, Daniel Haefliger, Anja Boisen, " Processing of thin SU8", J. Micromech. Microeng. , **18** 125020 (2008).
140. O. Ogbuu , Q. Du, H. Lin, L. Li, Y. Zou, E. Koontz, C. Smith, S. Danto, K. Richardson, J. J Hu, " Impact of stoichiometry on structural and optical properties of sputter deposited multicomponent tellurite glass films", Journal of American Ceramic Society, **98** 1731-1738 (2015).
141. K.T Vu, S.J Madden, "Reactive ion etching of tellurite and chalcogenide waveguides using hydrogen, methane and argon", Journal of Vaccum Science & Technology A, **29** 011023 (2011).
142. E. Chierici, M.C Didavide, A.Moro, O. Rossotto, L. Tallone, E. Monchiero, Proceedings of IEEE/LEOS Workshop on Fibre ad ptical passive Components (IEEE, Piscataway, NJ, 2002), p.29
143. K. Vu, S. Madden, "Tellurium dioxide Erbium doped planar rib waveguide amplifiers with net gain and 2.dB/cm internal gain", Optics Express **18** 19192 (2010).
144. Y. Zou, D. Zhang, H. Lin, L. Li, L. Moreel, J. Zhou, Q. Du, O. Ogbuu, S. Danto, J.D. Musgraves, K. Richardson, K. Dobson, R. Birkmire, J. Hu, " High-Performance, High-Index-Contrast Chalcogenide Glass Photonics on Silicon and Unconventional Non-planar Substrates", Adv. Opt. Mater. **2** 478-486 (2014).

145. I. Zubel and M. Kramkowska, “The effect of isopropyl alcohol on etching rate and roughness of (1 0 0) Si surface etched in KOH and TMAH solutions”, Sensors and Actuators A: Physical, **93** 138-147 (2001).
146. H. G. G. Philipsen, J. J. Kelly, “Anisotropy in the Anodic Oxidation of Silicon in KOH Solution”, Electrochemical acta, **54** 3526-3531 (2009).
147. C. R. Yang, P. Y. Chen, C. H. Yang, Y. C. Chiou, and R. T. Lee, “Effects of various ion-typed surfactants on silicon anisotropic etching properties in KOH and TMAH solutions”, Sensors and Actuators A: Physical, **119** 271-281 (2005).
148. H. Schmid, B. Michel “Siloxane Polymer for high- resolution, high-accuracy soft lithography”, Macromolecules **33** 3042-3049 (2000).
149. T.W Odom, J. C. Love, D. B Wolfe, K.E Paul, G.M Whitesides, “ Improved pattern transfer in soft lithography using composite stamps”, Langmuir, **18** 5314-5320 (2002).
150. H. Kang, J. Lee, J. Park, H.H Lee, “ An improved method of preparing composite poly(dimethylsiloxane) moulds”, Nanotechnology, **17** 197-200 (2006).
151. J. D. Musgraves , P. Wachtel , S. Novak , J. Wilkinson , K. Richardson , “Composition dependence of the viscosity and other physical properties in the arsenic selenide glass system” J. Appl. Phys., **110** 063503 (2011).